IDŐJÁRÁS

QUARTERLY JOURNAL
OF THE HUNGARIAN METEOROLOGICAL SERVICE

CONTENTS

VOL. 125 * NO. 3 * JULY – SEPTEMBER 2021

IDŐJÁRÁS

Quarterly Journal of the Hungarian Meteorological Service

Editorial Office: Kitaibel P.u. 1, H-1024 Budapest, Hungary
P.O. Box 38, H-1525 Budapest, Hungary
E-mail: journal.idojaras@met.hu
Fax: (36-1) 346-4669

Indexed and abstracted in Science Citation Index Expanded™ and Journal Citation Reports/Science Edition
Covered in the abstract and citation database SCOPUS®
Included in EBSCO's databases

Subscription by mail:
IDŐJÁRÁS, P.O. Box 38, H-1525 Budapest, Hungary
E-mail: journal.idojaras@met.hu

DOI:10.28974/idojaras.2021.3.1

IDŐJÁRÁS

Quarterly Journal of the Hungarian Meteorological Service
Vol. 125, No. 3, July – September, 2021, pp. 367–396

Basics of the atmospheric energetics: A brief summary of global and regional atmospheric energetics reflected upon the university curricula

Réka Ágnes Dávid* and **Péter Tasnádi**

Department of Meteorology,
Eötvös Loránd University,
H-1117 Budapest, Pázmány P. st. 1/A, Hungary

Corresponding author E-mail: davidreka@caesar.elte.hu

(Manuscript received in final form April 22, 2021)

Abstract— The purpose of this study is to provide an overview of the science and development of atmospheric energetics, its so far matured parts to date, and the direction of the researches. However, we restrict ourselves to the discussion of the very basic results of the researches to reveal the parts the introduction of which can be suggested into the compulsory education of the future meteorologist. This became feasible especially due to the rapid development of the personal computer that makes possible the calculation of the atmospheric energies for students by using their own laptops, so this field of meteorology now can be a tactile reality for them. The founder of atmospheric energetics was Lorenz, who formulated for a global, dry atmosphere the concept of available potential energy, which is the difference between the current energy state of the atmosphere and a reference state with minimum energy. His basic results concerning the global description of atmospheric energetics have already become part of the university curriculum. It is important to be able to describe the energy balance of the atmosphere both locally as well as globally, for which the introduction of enthalpy and exergy seemed appropriate. The advantage of examining the dry atmosphere is that significant simplifications can be applied, but the atmosphere is finally moist, so research has also started in this direction, first with a global and then with a local approach. The key is to find the reference state, which is a complex, computationally demanding task. In this paper, we focus on the most important steps of this process and concentrate on the thermodynamic basis of the new concepts.

Key-words: atmospheric energetics, available potential energy, moist available potential energy, enthalpy, exergy, thermodynamics, education

1. Introduction

At the end of the 19th century, Hertz (who is famous for his long-wavelength electromagnetic waves discovery) delivered a lecture, which has been almost forgotten, about the energy budget of the earth and gave quite precise estimations of the energy balance of the Earth (*Mulligan* and *Hertz*, 1997). In atmospheric energetics, the concept of available kinetic energy was introduced by *Margules* (1906). The maximum possible kinetic energy was identified in an isolated part of the air, which can be achieved through adiabatic changes starting from rest. The real development of atmospheric energetics launched with Edward Lorenz's pioneering paper (*Lorenz*, 1955) introducing the concept of available energy.

After Lorenz, many excellent researchers have worked on the field, and the literature on it became very rich. It can be quoted some excellent reviews and books on it *(Dutton*, 1973; *Van Mieghem*, 1973; *Marquet*, 1991[1]; *Wiin-Nielsen* and *Chen*, 1993; *Tailleux*, 2013). However, basic textbooks on dynamic meteorology generally have satisfied with the discussion of Lorenz's work and, except for Dutton, do not step toward more recent results (*Dutton*, 1976; *Panchev*, 1985; *Zdunkowski* and *Bott*, 2003; *Holton*, 2004; *Mak*, 2011; *Hoskins* and *James*, 2014). In this paper, the basics of atmospheric energetics, particularly its thermodynamic, will be reviewed background. Now, atmospheric energetics developed into a field of meteorology which supports highly the complex thinking on the explanation of the global circulation and on the local atmospheric motion. In light of this, dynamic meteorology textbooks devote an undeservedly short chapter to the topic. Maybe, it could be justified on the grounds that the field is still undeveloped and its knowledge is constantly changing, but since Lorenz's work, there have been a number of achievements that have been clarified and can rightly become materials of the textbooks. Therefore, we intentionally focus only on the basic issues and are not dealing with those details that are still in doubt. We emphasize those parts that are worth discussing in the standard educational materials.

The basics of the energetics are also processed in the book of *Dési* and *Rákóczi* (1970) as well as in *Götz* and *Rákóczi* (1981). The first book is based on the work of Margules, while the second uses Lorenz's energy conversion ideas. In the work of *Práger* (1982), the available potential energy (*APE*) concept of Lorenz is detailed. *Makainé* (1971, 1972, 1974) analyzed in some publications the relevancy of the *APE* in synoptic problems in Hungarian. *Czelnai et al.* (1991) discusses shortly the energy conversions of the atmosphere among the other basic transport processes. *Major et al.* (2002) studied the climatic energetics of Hungary.

[1] A new (2014) version of the original paper is available on the webpage of the author with valuable new comments. http://www.umr-cnrm.fr/spip.php?article833&lang=en

We overview the question of the availability and its thermodynamic base for atmospheric energetics. The possibility of the use of the concept of available potential energy for global and local processes of the atmosphere will be discussed, and relevant definitions for dry and moist atmospheres will be also investigated. Special attention will be paid to the problem of the reference state. From the literature, some are emphasized in *Table 1* which provides the structure of the topic and which papers, in our opinion, can be regarded as the milestones of the development of atmospheric energetics.

Table 1. Different cases and approaches which are in focus. (The study of *Tailleux* (2013) contains global view as well.)

	Dry case	**Moist case**
Global view	*Lorenz*, 1955 *Dutton*, 1973	*Lorenz*, 1978
Local view	*Marquet*, 1991 *Tailleux*, 2013	*Harris* and *Tailleux*, 2018

2. Conversions of the energies in the atmosphere

There are various forms of energy in the atmosphere, the almost only source of which is the Sun. The study of atmospheric energetics belongs to the field of dynamic meteorology; its general target is to describe the energy generation, transportation, and dissipation (*Wiin-Nielsen* and *Chen*, 1993; *Götz* and *Rákóczi*, 1981).

The energy of the atmosphere consists of the internal, potential, and kinetic energy. The specific energies are the before mentioned forms of the energy per unit mass (in the same order):

$$i = c_v T\,, \tag{1}$$

where c_v is the specific heat of air at constant volume and T is the temperature,

$$\phi = gz, \tag{2}$$

where g denotes the gravitational acceleration, z is the altitude,

$$k = \frac{\mathbf{v}^2}{2}, \tag{3}$$

where **v** is the three-dimensional velocity vector relative to the Earth. The previous quantities Eqs. (1) – (3) have to be integrated over the total mass of the atmosphere to get the total amounts of energy of the atmosphere ($E = \int_{V_A} e\rho \mathrm{d}V$, where e can be i, ϕ or k, and V_A is the volume of the atmosphere).

Table 2 below shows the annual mean values of the energy forms for the Northern Hemisphere. It has to be pointed out, that the kinetic energy is a few orders of magnitude smaller, than the internal or the potential energy. Kinetic energy provides the energy for the midlatitude's cyclones. It decreases in summer partly due to the changes in the meridional temperature gradient (*Gertler* and *O'Gorman*, 2019).

Table 2. The annual mean values of the various energy forms for the Norther Hemisphere (1000–75 hPa) expressed in energy per unit area or per unit mass (*Oort*, 1971).

Energy	**[kJ/m^2]**
Internal	1674.8×10^6
Potential	567.5×10^6
Kinetic	1153.4×10^3

The atmosphere is not an equilibrium thermodynamic system, but it is approximately in radiation balance, which means that the incident radiation energy equals the emitted radiation. The processes of the atmosphere, among them the general circulation, are governed by kinetic energy, so to understand these processes, we need to study the generation and dissipation of the kinetic energy and also its conversion from other types of energies.

The posed questions of the atmospheric energetics in the early years of the twentieth century were related to the energetics of the cyclones, whether where the energy of the middle-latitude depressions comes from (*Margules*, 1910). According to the observations, there is not enough energy from the work against the pressure gradient. It turned out, that although the atmosphere contains a large amount of potential and internal energy, only a small part of them can be transformed into kinetic energy. It can be understood using a simple example created by *Wiin-Nielsen* and *Chen* (1993) following *Margules* (1910). Imagine a vessel filled with two fluids of different densities. The two fluids are separated by a vertical wall, so the fluids situate beside each other. When the wall is removed, the denser fluid goes to the bottom of the vessel and the less dense stratifies above it (the fluids do not mix). The potential energy of the fluids is decreasing and reaches its minimum value. Although the potential energy of the

fluids might be very high, its available part is only the difference between that of the initial and final state. This available part may be very low due to this process.

The details of the following equations can be found in the work of *Wiin-Nielsen* and *Chen* (1993) and in Hungarian in *Götz* and *Rákóczi* (1981). One of the most general laws of nature, the law of energy conservation also applies to the atmosphere. Applying the law of energy conservation to thermodynamic processes, we get the first law of thermodynamics. If we look for the derivatives of the global energy forms, the derivatives of the internal energy can be obtained from the integral of the internal energy density which can be expressed from the differential form of the first law $c_v dT = \delta q - p d\alpha$, where the continuity equation was used for getting the second term at right-hand side of the above mentioned equation:

$$\frac{\mathrm{d}I}{\mathrm{d}t} = \int_{V_A} \dot{q}\rho \mathrm{d}V \quad - \int_{V_A} p\nabla \cdot \mathbf{v} \mathrm{d}V \quad , \tag{4}$$

Where δq and $\dot{q}$ are the heat absorbed by the unit mass and the heat current to unit mass, respectively, $\rho = \frac{1}{\alpha}$ is the density of the air, α is the specific volume of the air, p is the pressure, and $\mathbf{v}$ is the velocity vector of the wind. In Eq. (4), the first term is the internal energy generation ($G(I)$) and the second one is the conversion from internal energy to kinetic energy ($C(I,K)$). There are two processes, which influence the internal energy: (1) internal energy increases if the atmosphere is heated, where the density is high or it is cooled, where the density is low, (2) internal energy decreases in divergent areas, where the average pressure is high or in convergent areas, where the pressure is low.

The global form of the change of potential energy is the following:

$$\frac{\mathrm{d}P}{\mathrm{d}t} = \int_{V_A} g\rho w \mathrm{d}V \quad , \tag{5}$$

where w is the vertical wind component. Eq. (5) is the conversion from potential energy to kinetic energy with a minus sign ($-C(P,K)$). And finally, the form of the change of global kinetic energy is:

$$\frac{\mathrm{d}K}{\mathrm{d}t} = \int_{V_A} p\nabla \cdot \mathbf{v} \mathrm{d}V \quad - \int_{V_A} g\rho w \mathrm{d}V \quad + \int_{V_A} \mathbf{v} \cdot \mathbf{F} \mathrm{d}V \quad , \tag{6}$$

where **F** is the frictional force and the other notations have been already defined. The first term of Eq. (6) is known from Eq. (4), which is $C(I,K)$, the second term is the conversion from potential energy to kinetic energy ($C(P,K)$), and the

last term is the dissipation of kinetic energy ($D(K)$). So, Eqs. (4)–(6) can be written as:

$$\frac{\mathrm{d}I}{\mathrm{d}t} = G(I) - C(I,K), \tag{7}$$

$$\frac{\mathrm{d}P}{\mathrm{d}t} = -C(P,K), \tag{8}$$

$$\frac{\mathrm{d}K}{\mathrm{d}t} = C(P,K) + C(I,K) - D(K). \tag{9}$$

In the case of long-time average, a steady-state can be considered, which means that there are no changes in the form of energies, which results that the time derivatives of the energy forms are zero, so we get (*Götz* and *Rákóczi*, 1981; *Wiin-Nielsen* and *Chen*, 1993):

$$G(I) = C(I,K) = D(K), \tag{10}$$

$$C(P,K) = 0. \tag{11}$$

Finally, it is worth mentioning, that the gravitational potential and internal energy in an ideal gas of hydrostatic state are proportional to each other, and since the atmosphere can be regarded as an ideal gas, the sum of its specific potential and specific internal energy can be expressed with its specific enthalpy. Lorenz called the sum of the internal and gravitational potential energy simply as potential energy, but enthalpy is a more exact name that helps to avoid misunderstandings originating from the mixing of the terminology. Using this, Lorenz got simpler equations for the cycle of the energy transformations:

$$\frac{\mathrm{d}H}{\mathrm{d}t} = G(H) - C(P,K), \tag{12}$$

$$\frac{\mathrm{d}K}{\mathrm{d}t} = C(H,K) - D(K), \tag{13}$$

where $H = I + P$. However, the numerical value of these conversion factors can only be realistic if the moisture of the air is also taken into account. *Fig. 1* shows the scheme of the energy cycle.

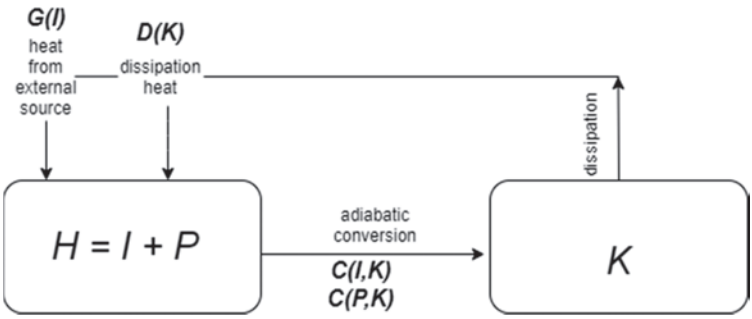

Fig. 1. The scheme of the energy cycle.

3. The equilibrium state of the atmosphere

As we have expounded, the atmosphere is not in a thermodynamic equilibrium state, but it is in approximate dynamic equilibrium, because of the balance of the incoming and outgoing radiation. In contrast to outgoing radiation, incident radiation is not evenly distributed on the surface of the Earth, and due to this, general circulation which continuously transfers the energy from the equator toward the poles is developing.

According to thermodynamics, the equilibrium state of a system can be found in two equivalent ways. If the system is adiabatically (entropically) closed, then its equilibrium state is where its energy is minimum. On the other hand, if the system is energetically closed, then its equilibrium state belongs to its minimum energy one (*Callen*, 1960).

The specific entropy can be obtained by the integration of the differential form of the thermodynamic law $ds = c_v \frac{dT}{T} + \frac{p}{T} d\alpha$ and with the use of the gas law:

$$s = c_v \ln \frac{T}{T_0} + R \ln \frac{\alpha}{\alpha_0} \quad , \tag{14}$$

where s is the specific entropy, T_0 and α_0 are an arbitrary reference temperature and specific volume, respectively.

Obviously, the state of a real atmosphere is neither entropically nor energetically closed. However, an equilibrium state can be assigned to either the current state of the atmosphere or some average state if one closes fictitiously the atmosphere and determines the extremum of the energy or the entropy.

Lorenz and Dutton carried out this procedure, Lorenz applied the energy minimum principle, while Dutton used entropy maximum for searching equilibrium state of the dry atmosphere (see *Fig. 2*).

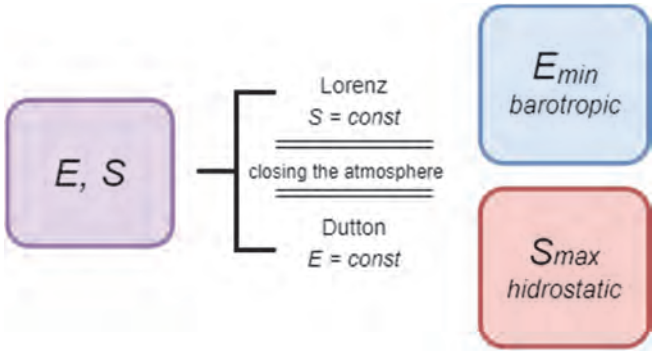

Fig. 2. The state of thermodynamic equilibrium based on the two principles: the approach of Lorenz (up) and Dutton (down). *E* and *S* denotes the global energy and entropy of the atmosphere, respectively.

Despite that the numerical results concerning dry atmosphere do not reflect in every respect the real properties of the atmosphere, they can point to many interesting facts. They can be used in cases when the correlations between processes and not the exact numerical values are in focus. Several atmospheric energy issues are related to the storage and movement of energy that takes place between the components of the climate system (atmosphere, ocean, land, and cryosphere). As an example, we show the correlation between sea ice cover and energies (*Table 2* and *Fig 3*). The details of the calculations can be seen in *Appendix A*.

Table 2. Pearson correlation between the sea ice cover, the total entropy, and the total energy of the atmosphere (1979–2019). ERA5 database was used for the calculations (see *Appendix A*).

	Sea ice cover	**Entropy**
Energy	-0.81	0.99
Entropy	-0.82	

Unsurprisingly, there is a very strong correlation between the energy and the entropy, and negative correlation between the energy and the sea ice cover, and slightly different between the entropy and the sea ice cover, this is illustrated by *Fig. 3*.

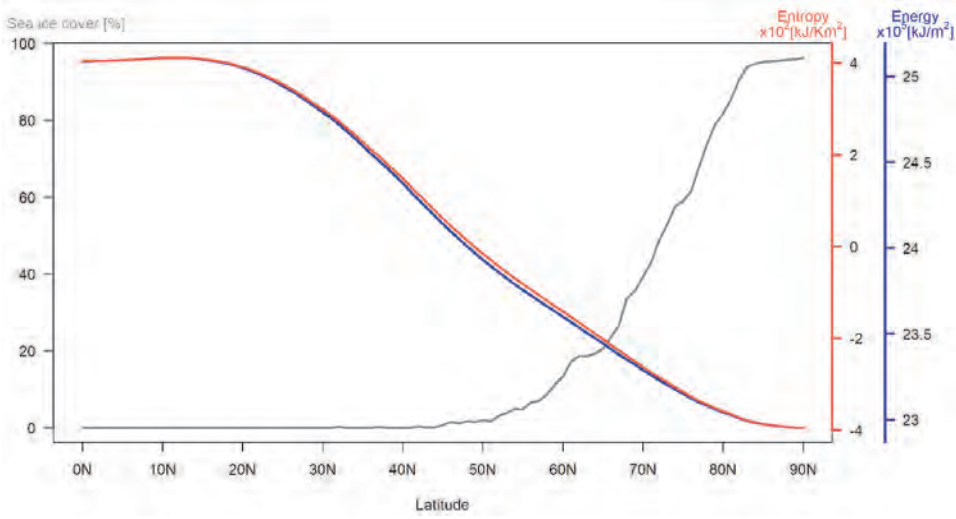

Fig. 3. The average energy and entropy per m^2 cell of a given latitude and the sea ice for the Northern Hemisphere. ERA5 database was used for the calculations (*Appendix A*).

In most cases, the relationship between sea ice and oceanic energy is examined (*Su* and *Ingersoll*, 2016), but researches have also shown that there is also a relationship between the global energy on the top of the atmosphere and the ocean heat content (*Trenberth et al*., 2014) or between atmospheric *APE* and sea ice cover (*Novak* and *Tailleux*, 2018). Particular attention was paid to sea ice around Greenland and the Ross Sea (*Shepherd* and *Wingham*, 2007; *Jacobs et al.*, 2011).

Fig. 4 shows the annual averages of the entropy, energy, and sea ice for the Northern Hemisphere. There is an increasing trend in the ocean heat content from 1993 (*Trenberth et al*., 2014), this can be seen as the decreasing trend in the sea ice cover in *Fig. 4*.

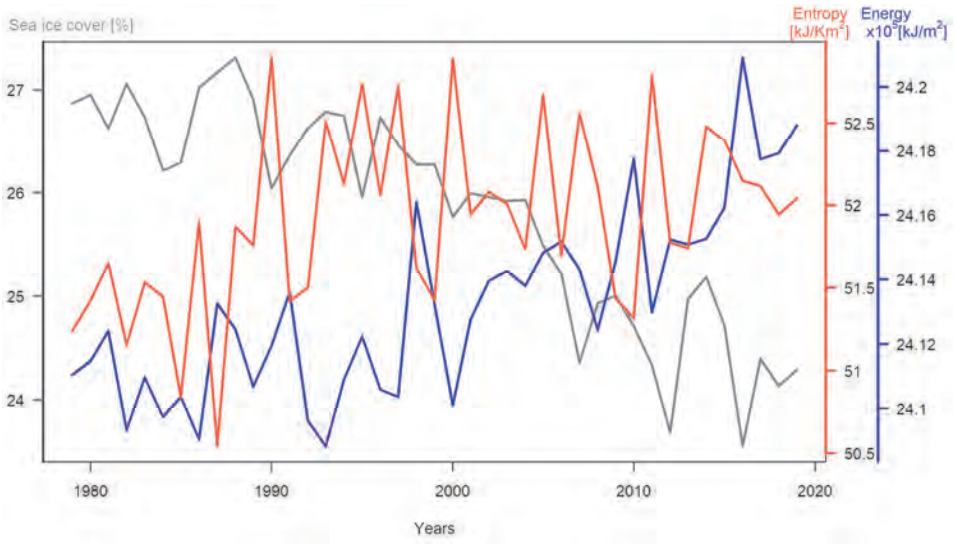

4. Fig. The annual averages of the sea ice, entropy, and energy per m^2 for the Northern Hemisphere. ERA5 database was used for the calculations (see *Appendix A*).

4. The available enthalpy

The question of availability was addressed by Edward Lorenz in 1955 when he introduced the concept of available potential energy (*Lorenz*, 1955). His aim, analyzing the global circulation in the twentieth century, was to find the energy sources and sinks of atmospheric motions, as well as the forms of energy transformations that allow atmospheric motions to persist despite frictional dissipation.

The available potential energy of Lorenz (APE) was defined to be the maximum part of the sum of the internal and potential energy (in hydrostatic case, it is the enthalpy) of the atmosphere that can be converted to kinetic energy under ideal conditions during isentropic processes. In the following, the term enthalpy will be used instead of the potential energy used by Lorenz. (The approximations, which Lorenz used, clearly show that Lorenz regarded the actual state of the atmosphere to be hydrostatic.) It follows, that there is some part of enthalpy that cannot be converted into kinetic energy, thus a state of minimum enthalpy in the atmosphere should be defined as a reference state. APE was defined by Lorenz as the difference between the enthalpy of the atmosphere's real (actual) and reference states. To find the state of minimal enthalpy, he rearranged adiabatically the actual state of the atmosphere to a

statically completely stable and vertically stratified one, and using this state he calculated the APE. Lorenz also determined an approximate formula for the practical calculation of APE. The total enthalpy in a hydrostatic atmosphere is the following:

$$P = \int_{V_A} c_p \rho T \mathrm{d}V \quad = \int_{A_G} \int_0^{\infty} c_p \rho T \mathrm{d}z \, \mathrm{d}A \,, \tag{15}$$

where A_G is the surface of the Earth. To execute the integration in a pressure coordinate system (p-system), we use the hydrostatic approximation:

$$\mathrm{d}z = -\frac{1}{\rho \mathrm{g}} \, \mathrm{d}p. \tag{16}$$

Entering Eq. (16) in Eq. (15) we get:

$$P = \frac{c_p}{g} \int_{A_G} \mathrm{d}A \int_0^{p_0} T \mathrm{d}p \,. \tag{17}$$

Applying potential temperature as vertical coordinate:

$$APE = TH_A - TH_R = \frac{c_p}{2gp_0^{\kappa}(\kappa+1)} \int \mathrm{d}S \int_0^{p_0} \left(p^{(\kappa+1)} - \bar{p}^{(\kappa+1)}\right) \mathrm{d}\theta \approx$$
$$\approx \frac{R}{2gp_0^{\kappa}} \int \mathrm{d}S \int_0^{p_0} \bar{p}^{(\kappa+1)} \left(\frac{p'}{\bar{p}}\right)^2 \mathrm{d}\theta, \tag{18}$$

where the total enthalpy (TH) is expressed as:

$$TH = I + P = \int \mathrm{d}S \int_0^{\infty} \rho g z \mathrm{d}z + \int \mathrm{d}S \int_0^{\infty} \rho c_v T \mathrm{d}z = \int \mathrm{d}S \int_0^{\infty} \rho c_p T \mathrm{d}z =$$
$$\frac{c_p}{g} \int \mathrm{d}S \int_0^{p_0} T \mathrm{d}p = \frac{c_p}{g p_0^{\kappa}} \frac{1}{\kappa+1} \int \mathrm{d}S \int_0^{\infty} p^{\kappa+1} \mathrm{d}\theta \,. \tag{19}$$

In the equations, c_p and c_v are the specific heat under constant pressure and constant volume, respectively, R is the specific gas constant for dry air, κ is the ratio of R to c_p, g is the gravitational constant, p is the pressure, p_0 is the pressure at the surface, which can be regarded to 1 atm, θ is the potential temperature, T is the temperature, ρ is the density, z is the height, $\mathrm{d}S$ is the surface element of the isentropic surfaces, and $p' = p - \bar{p}$.

It shows that the *APE* is proportional to the pressure variance on isentrops to the leading order. Returning to *p* as vertical coordinate:

$$APE \approx \frac{R}{2gp_0^{\kappa}} \int \mathrm{d}S \int_0^{\infty} \bar{p}^{(\kappa+1)} \left(\frac{p'}{\bar{p}}\right)^2 \mathrm{d}\theta = \frac{1}{2g} \int \mathrm{d}S \int_0^{p_0} \bar{\alpha}\bar{\theta} \left(\frac{\partial\bar{\theta}}{\partial p}\right)^{-1} \left(\frac{\theta'}{\bar{\theta}}\right)^2 \mathrm{d}p. \quad (20)$$

Wiin-Nielsen used the $\frac{\theta'}{\bar{\theta}} \approx \frac{\alpha'}{\bar{\alpha}}$ approximation, while Lorenz applied $\frac{\theta'}{\bar{\theta}} \approx \frac{T'}{\bar{T}}$. The Lorenz approximation leads to a result depending on the temperature variance on isobaric surfaces:

$$APE = \int \mathrm{d}S \int_0^{p_0} \frac{1}{\bar{T}} \frac{T'^2}{\gamma - \Gamma} \mathrm{d}p, \quad (21)$$

where γ and Γ are the actual and the adiabatic lapse rate, respectively. *Wiin-Nielsen* and *Chen* (1993) derived a formula depending on the variance of the specific volume α' and the static stability parameter $\bar{\sigma}$:

$$\bar{\sigma} = \frac{\bar{\alpha}}{\bar{\theta}} \frac{\mathrm{d}\bar{\theta}}{\mathrm{d}p} . \quad (22)$$

Eq. (22) is a definition equation, where σ is considered constant, and this constant is taken as the average value of it ($\bar{\sigma}$).

$$APE = \int \mathrm{d}S \int_0^{p_0} \frac{1}{2g} \frac{\alpha'^2}{\bar{\sigma}} \mathrm{d}p. \quad (23)$$

It can be shown that $C(H, K)$ and $G(H)$ equal to $C(APE, K)$ and $G(APE)$.

5. Dutton's entropic energy

Dutton (*Dutton* and *Johnson*, 1967; *Dutton*, 1976) approached the problem of the equilibrium state of the atmosphere through the determination of the maximum entropy. He determined the maximum entropy state of the energetically closed atmosphere with the use of the calculus of variations. According to Dutton's point of view, atmospheric movements are induced by thermal driving forces, so at a given moment he fictitiously insulated the atmosphere from the external energy sources keeping the total energy constant and sought what end state the equalization of internal inhomogeneities leads to.

In a closed atmosphere, due to differences in temperature and pressure, various processes take place that increases entropy. When the processes stop, the entropy will be maximum. This is the state where the atmosphere would converge, if it was cut off from all the energy sources. Dutton called this maximum entropy state an associated state to the actual one. Dutton's calculation based on the calculus of variations led to a final state of the atmosphere, which is isotherm and hydrostatic. This result can be easily predicted also an intuitive way. The maximum entropy state of the atmosphere is a so-called dead state, in which only random thermal motion can occur, and macroscopic processes are perfectly impossible due to the balanced intensive state variables. In this state the temperature is constant, all wind velocity is zero, there is no convection, and consequently, the pressure is hydrostatic.

Let the total energy and the mass at the initial state of the atmosphere be *E* and *M*, respectively, and let the atmosphere be an ideal gas. Then the properties of the associated maximum entropy state are the following. Its temperature is

$$T_0 = \frac{E}{c_p M}, \tag{24}$$

it is motionless and the pressure obeys the barometric height law:

$$p(z) = p_0 \exp(-\frac{gz}{RT_0}), \quad p_0 = \frac{Mg}{4{R_E}^2\pi}, \tag{25}$$

where R_E is the radius of the Earth. It should be mentioned that the energy ($E = E_0$) in the actual state and in the associated state equal with each other, and while in the actual state the energy consists of internal, potential (gravitational) and kinetic energies ($E_0 = E = I + P + K$), in the associated state there are only internal and potential energies ($E_0 = I_0 + P_0 = H_0$). Since the atmosphere is an ideal gas, and in the associated state it is hydrostatic, the energy equals to the enthalpy.

Dutton determined the difference of the entropy of the associated and actual state of the atmosphere and introduced the concept of entropic energy *N* as $N = T_0(S_0 - S)$, where S_0 and S are the entropy of the associated and actual state, respectively. Dutton proved, that

$$N = T_0(S_0 - S) = K + T_0\Sigma, \tag{26}$$

where $T_0\Sigma$ is the static entropic energy. To obtain this equation Dutton expresses $S_0 - S$ as a sum of the leading terms of its Taylor series and a remainder term. The remainder term Σ can be expressed as an integral of the positive definite

homogeneous second order form of the temperature and specific volume, which proves that it is positive.

$$\Sigma = \int_V \frac{\rho}{2}\left\{ c_v \left[\frac{\frac{T-T_0}{T_0}}{1+\frac{\lambda_1(T-T_0)}{T_0}} \right]^2 + \left[\frac{\frac{\alpha-\alpha_0}{\alpha_0}}{1+\frac{\lambda_2(\alpha-\alpha_0)}{\alpha_0}} \right]^2 \right\} \mathrm{dV}', \qquad (27)$$

where λ_1 and λ_2 are constants, which satisfies $0 \leq \lambda_1, \lambda_2 \leq 1$. λ_1, λ_2 show the position where the remaining term should be calculated in the $(T,\ T_0)$ and $(\alpha,\ \alpha_0)$ interval.

The entropic energy determines a kind of „distance" from the equilibrium state, and in a really closed system, it would decrease monotonously when the system tends to its equilibrium state. It would mean that in the atmosphere the general circulation ought to cease. Clearly, the atmosphere is not an isolated system, and therefore, the net heating provides the entropy destruction that permits N to avoid the monotonic evolution.

6. Comparison of the two theories

Both theories are unrealistic, because besides the arbitrary closing of the atmosphere, they concern a dry atmosphere. The neglecting of the moisture leads by all means unrealistic results. Nevertheless, both theories have significantly contributed to the theoretical clarification and better understanding of the role of changes in the atmospheric energies in the processes of the atmosphere. A further problem is that both theories treat globally the atmospheric energies, so they are not suitable for the description of the local processes which can be important for example in cyclones.

However, contrary to Lorenz's theory, where processes would no longer take place in the atmosphere under the constancy of entropy, this associate end state (under appropriate conditions) could really be reached by the atmosphere. Using thermodynamic argumentation only, the concept of entropy promises a prediction about the direction a thermodynamic process must take. Although this maximum entropy state is also fictitious, it is more realistic than the minimum energy state applied by Lorenz. Despite of this, recently Lorenz' point of view dominates the energy description of the atmosphere. In our opinion, Dutton's approach should be also involved in the standard curriculum, since the entropic approach of the atmospheric processes is at least as important as the energetic one.

7. The local definition by Marquet and Tailleux

Marquet in his excellent paper (*Marquet*, 1991) re-examined the concept of APE and defined a locally practicable version of it. He placed in a historical perspective the development and various definitions of the concept of available energy and, albeit with doubts, identified it with the exergy. However, the main novelty of his paper is the local definition of the specific available potential energy as the generalization of the Lorenz' global available potential energy and the entropic energy of Dutton. As the topic is very diverse and burdened by terminological inconsistencies, we recommend turning for details to the excellent papers of *Keenan* (1951), *Haywood* (1974a,b), and *Marquet* (1991), and to navigate between different technical terms. Especially the application of the various versions of the APE theory was developed by many researchers.

The algebraic expression of the APE density would allow the study of energy conversions in open domains (e.g., cyclones, baroclinic waves), where boundary fluxes are also considered. Furthermore, by focusing on the energies at various distinct pressure levels, the tropospheric-stratospheric energy exchange processes could be interpreted.

The approach of Marquet shows that the hydrodynamic application of available enthalpy allows the generalization of available energy concepts previously introduced by Lorenz and Dutton to global meteorological processes. Marquet defines the specific available enthalpy as:

$$a_h \equiv (h - h_r) - T_r(s - s_r) = (h - T_r s) - (h_r - T_r s_r), \tag{28}$$

which can be expressed as

$$a_h(T,p) = c_p(T - T_r) - c_p T_r \ln\left(\frac{T}{T_r}\right) + R T_r \ln\left(\frac{p}{p_r}\right), \tag{29}$$

where h denotes the enthalpy and T_r and p_r are the reference temperature and reference pressure, respectively. (The exact definitions of T_r and p_r will be given by (43–44), and the physical interpretation of them will be discussed later.) An interesting property of available enthalpy in an ideal gas is that it can be separated into temperature- and pressure-dependent terms:

$$a_h(T,p) \equiv a_T(T) + a_p(p), \tag{30}$$

where the temperature (a_T) and pressure (a_p) dependent terms of the specific enthalpy are:

$$a_T = c_p(T - T_r) - c_p T_r \ln\left(\frac{T}{T_r}\right), \tag{31}$$

$$a_p = RT_r \ln\left(\frac{p}{p_r}\right). \tag{32}$$

Marquet has derived a local energy cycle with the set of energy components: the specific gravitational potential (e_G) and the kinetic energy (e_K), furthermore, with the a_T and a_P ,which are the temperature (T) and the pressure (p) dependent term of the specific enthalpy, respectively. The capital letters with s subscript denote the conversions, generation, and dissipation of the specific quantities. The subscripts distinguish them from those which are in Lorenz's formulas without indices and which concern global quantities (the lower indices denote of the type of the quantities).

$$\begin{aligned}
\frac{\mathrm{d}e_G}{\mathrm{d}t} &= -C_s(G,K) \\
\frac{\mathrm{d}e_K}{\mathrm{d}t} &= +C_s(G,K) + C_s(h,K) - D_s(K) \\
\frac{\mathrm{d}a_T}{\mathrm{d}t} &= +C_s(p,T) - C_s(h,K) + G_s(h) \\
\frac{\mathrm{d}a_p}{\mathrm{d}t} &= -C_s(p,T)\,.
\end{aligned} \tag{33}$$

The $C_s(m,n)$ conversion factors give the increase of type nth energy at the expense of the type mth.

Knowing Marquet's results, Dutton proved them on a much simpler intuitive "ad hoc" way, which is briefly recalled below (*Dutton*, 1992). Multiplying the equation of motion ($\frac{\mathrm{d}\mathbf{v}}{\mathrm{d}t} = -\alpha\nabla p - g\mathbf{k} + \alpha\mathbf{F} + f(\mathbf{k}\times\mathbf{v})$) by $\mathbf{v}$ we got the equation:

$$\frac{\mathrm{d}e_K}{\mathrm{d}t} = -\alpha\mathbf{v}\cdot\nabla p + C_s(G,K) + D_s(K), \tag{34}$$

where the e_G energy component is the following:

$$\frac{\mathrm{d}e_G}{\mathrm{d}t} = -g\frac{\mathrm{d}z}{\mathrm{d}t} = -C_s(G,K), \tag{35}$$

and D_s is the specific rate of work of all the forces except the gravitation and gradient ones. From the first law of thermodynamics it can be obtained that

$$\frac{\mathrm{d}e_h}{\mathrm{d}t} = \alpha\frac{\mathrm{d}p}{\mathrm{d}t} + \dot{q} = \alpha\frac{\partial p}{\partial t} + \alpha\mathbf{v}\cdot\nabla p + \dot{q}\,, \tag{36}$$

where $\dot{q}$ is the heating rate. Comparing the thermodynamic and kinetic energy equations it can be concluded that

$$\alpha \mathbf{v} \cdot \nabla p = -C_s(h, K). \tag{37}$$

The specific heating rate can be written in the following form:

$$\dot{q} = \frac{T_r}{T}\dot{q} + \left(1 - \frac{T_r}{T}\right)\dot{q}. \tag{38}$$

The first term in the right side of Eq. (38) can be expressed with the specific entropy, Eq. (37):

$$s = s_T + s_p = c_p \ln\frac{T}{T_r} - R \ln\frac{p}{p_r}\,, \tag{39}$$

$$\frac{T_r}{T} q = T_r \frac{\mathrm{d}s}{\mathrm{d}t} = T_r \left(c_p \frac{\mathrm{d}\ln T}{\mathrm{d}t} - R \frac{\mathrm{d}\ln p}{\mathrm{d}t}\right). \tag{40}$$

Introducing

$$C_s(p, T) = -RT_r \frac{\mathrm{d}\ln p}{\mathrm{d}t} = -\frac{R}{p} T_r \omega\,, \tag{41}$$

where $\omega = \frac{\mathrm{d}p}{\mathrm{d}t}$ is the conversion from a_p to a_T, as well as the generation (G_s) of a_T, is $G_s = \alpha \frac{\partial p}{\partial t} + \left(1 - \frac{T_r}{T}\right)\dot{q}$ furthermore using available enthalpy components defined above, we can get with simple algebra the equations of the local cycle Marquet has found. The first term in G_s can be interpreted as the work due to adiabatic expansion, while the second is the heat reduced by the Carnot factor $\left(1 - \frac{T_r}{T}\right)$. The local cycle gives the energy balance of a motion of an atmospheric parcel. Having added the four equations of the cycle, we got the equation:

$$\frac{\mathrm{d}}{\mathrm{d}t}(e_K + e_G + a_h) = G_s - D_s. \tag{42}$$

The right hand side of Eq. (42) vanishes in a frictionless and isentropic steady flow, and then the hydrodynamic derivative equals zero, therefore, $e_K + e_G + a_h = c,\ c = \text{constant}$ along any particular streamline, but it may be different on different streamlines. This equation is a form of the Bernoulli equation.

The definition of the reference temperature and reference pressure is an intricate one. Marquet proposed and applied the following formulas:

$$\frac{1}{T_r} = \frac{1}{gM}\int_0^{p_0} \frac{1}{T}\,\mathrm{d}V_p \ , \tag{43}$$

$$\ln(p_r) = \frac{1}{gM}\int_0^{p_0} \ln(p)\,\mathrm{d}V_p, \tag{44}$$

where $\mathrm{d}V_p$ notes the small domains of the air we sum up as $\mathrm{d}V_p = \mathrm{d}A\mathrm{d}p = {R_F}^2\mathrm{d}\lambda\mathrm{d}\varphi cos\varphi\mathrm{d}p$, where $A = 4R^2\pi$ is the surface of the Earth, the other notations are the same as before. We reproduced the calculations made by Marquet with the ERA5 database (see *Appendix A*). The available enthalpy temperature- and pressure-dependent terms (*Fig. 5*) and their summation (a_h) are presented in this paper. As the latitude increases, the value of a_T decreases, and along the N30° it decreases below 2 kJ/kg. a_T loses its zonal picture around 300 hPa, where it begins to increase again. In fact, the value of a_p decreases with the pressure. *Fig. 6* shows a_h, the sum of a_T and a_p. As expected, a_h is similar to a_p due to it weights heavier on it ($a_p > a_T$). We see a minimal ratio of a curve close to the Equator, which is affected by a_T, where it has the highest values.

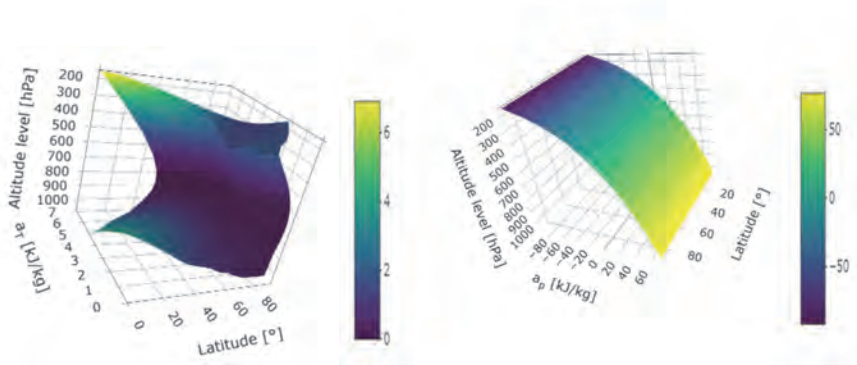

Fig. 5. The available enthalpy temperature- (left) and pressure-dependent (right) terms for the Northern Hemisphere, made by 41 years average.

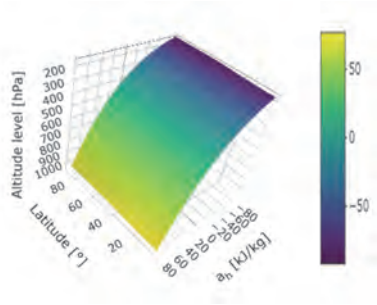

Fig. 6. The available enthalpy for the Northern Hemisphere, made by 41 years average. The calculated enthalpy values are visible on the axis and on the legend.

8. The exergy concept in atmospheric energetics

Marquet's available enthalpy concept can be connected to the concept of the exergy of steady-state open systems. The general description and the embedding of exergy concepts into thermodynamics can be found, e.g., in *Harmatha*, (1982), *Bejan* (2006), and *Dincer* and *Rosen* (2007). However, these studies have summarized the thermodynamic basis focusing on engineering concern of the exergy theory. The atmospheric application of the concept was discussed earlier by *Karlsson* (1990) and *Kucharski* (1997), and the latter author cited a lot of further references concerning the topic. However, we think that it is worth rigorously looking through the basics and origin of this concept and investigating thoroughly its possible connections with atmospheric energetics, particularly with the role of the reference state.

If a system is not in equilibrium with its environment, then spontaneous processes start to equalize the intensive state variables of the system and the environment. Due to these processes, after some time the system will be balanced with the environment. Up till the equilibrium befalls, energy and mass flow through the boundary of the system. The energy transport can be taken place by heat and work. We would like to control the transport processes to make maximum use of its internal energy be maximally exploit as work. The adiabatic process seems to be proper to achieve this goal. However, the processes with finite velocity are always irreversible which means that some part of the work is transformed (for example by friction) into heat and transferred back to internal energy. Because of this, we can conclude that the most efficient processes should be quasistatic, so reversible. It means that the maximum available work belongs to an ideal limiting case. The second law of thermodynamics prevents all internal energy from being transferred from the system as work. Naturally, the available part of the internal energy is the function both the state of the system and the environment.

To determine the maximally extracted work, imagine a system that is insulated from its environment and search the boundary conditions under which the maximum work can be extracted. Let us allow the quasistatic adiabatic processes between the system and the environment. Then the energy can be changed between them by performing work. Achieving the equilibrium state, the internal energy (U_{sys}) of the system becomes a minimum $W_{max} = \Delta U_{sys}$.

Connecting the system to a heat reservoir with constant temperature, the work performed during the setting of the balance between the system and the environment can be done isothermally, so the maximally extracted work equals the change of the free energy $W_{max} = \Delta F_{sys}$. (F_{sys} is the free energy of the system.) Similarly, if the system is connected to a work reservoir, the maximum work is $W_{max} = \Delta H_{sys}$, and in the case of both heat and work reservoirs, it is $W_{max} = \Delta G_{sys}$. (H_{sys} and G_{sys} denote the enthalpy and free enthalpy or Gibbs potential of the system, respectively.)

In the case of a system, which is not in equilibrium with its environment, the balanced state can be achieved by the combination of an isothermal and an adiabatic path. So, first the system is brought adiabatically to the temperature of the environment and after isothermally to the state of the environment. Adding the work performed through the two ways we get the maximum work available. Obviously, the maximum extractable work depends on the structure of the system. According to this, we can obtain two results depending on that the system is closed or it is a stationary open system, where proper reservoirs ensure the constancy of the temperature or the pressure.

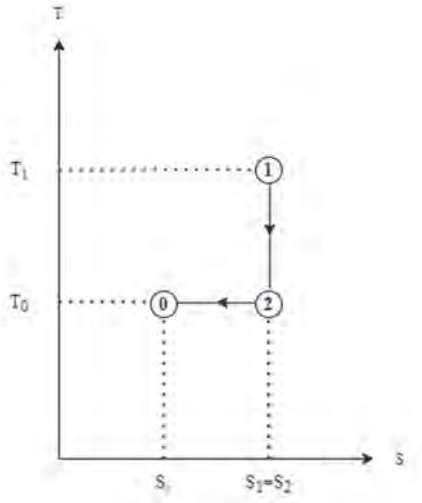

Fig. 7. A sequence of adiabatic and isothermal paths (0 is the state of the environment).

Fig. 7 shows in a T–S diagram the sequence of adiabatic and isothermal paths from state 1 to state 0 (which is the state of the environment). First, the system goes adiabatically from state 1 to state 2, where the temperature equals to that of state 0, after it goes isothermally to state 0. Following the thermodynamic path given in *Fig. 7*, the possible maximum of the extracted work can be determined. In the first adiabatic part of the path, the work performed by the system is $W_{1,2} = U_1 - U_2$, and on the second (isothermal) part it is $W_{2,0} = F_2 - F_0$. Consequently,

$$W_{max} = U_1 - U_2 + F_2 - F_1 = U_1 - U_2 + (U_2 - T_2 S_2) - (U_0 - T_0 S_0)\,. \quad (45)$$

Taking into account that, as *Fig. 6* shows, $T_0 = T_2$ and $S_0 = S_1$:

$$W_{max} = (U_1 - T_0 S_1) - (U_0 - T_0 S_0) = \Delta U - T_0(S_1 - S_0). \qquad (46)$$

In a steady state open system, where the constancy of pressure is ensured by a pressure reservoir, the extractable work, during the adiabatic change of state, is $W_{1,2} = H_1 - H_2$, while during the isothermal path, where the system is even connected to a heat reservoir, the work is $W_{2,0} = G_2 - G_0$. Adding these two contributions

$$W_{max} = H_1 - H_2 + G_2 - G_1 = H_1 - H_2 + (H_2 - T_2 S_2) - (H_0 - T_0 S_0)\,. \quad (47)$$

Taking into account again that $T_0 = T_2$ and $S_0 = S_1$:

$$W_{max} = (H_1 - T_0 S_1) - (H_0 - T_0 S_0) = \Delta H - T_0(S_1 - S_0). \qquad (48)$$

Strictly speaking, the maximum work extractable from a system is called exergy, and the calculations above show, that it depends on the state variables both the system and the environment. In a broader sense, the maximum work available from a steady state system is called exergy, too. These expressions are very similar to those giving the change of the free energy of the system and the change of the free enthalpy of the system. The only difference is that the free energy and the free enthalpy are state variables of the system and depend on the temperature of it, while the exergy depends on the temperature of the environment too.

The mathematical expressions of the exergy are formally very similar to those that defined for available potential energies (enthalpies) in atmospheric physics and introduced with various names. For example, Dutton's entropic energy:

$$N = T_0(S_0 - S), \qquad (49)$$

and Marquet's available enthalpy:

$$a_h \equiv (h - h_r) - T_r(s - s_r) = (h - T_r s) - (h_r - T_r s_r) \qquad (50)$$

are exergies. In expressions concerning atmospheric availability, reference states appear everywhere which can be corresponded in exergetics to properties of reservoirs or the surroundings. However, while in technical thermodynamics regarding engines, turbines, solar cells, and so on, there are well defined environment or physical systems which can be identified with reservoirs, in atmospheric physics, there are no such possibilities, the reference states have to be chosen arbitrarily. In the case of atmospheric flows, temperature and pressure reservoirs cannot be found, so the customary definitions cannot be used. It means that the concept of exergy is worth using in atmospheric energetics only

as an aid which helps through analogies. Naturally, physical state variables defined using arbitrarily chosen reference state can be expressed well the local atmospheric properties, which are suitable in the description of the local energetics of the atmosphere. This is expressed by Marquet in the following way: „The available enthalpy in this sense is a general thermodynamic local state function which has proved to be significant in order to be described as the part of (thermodynamic) energy that can be transformed into any other form of energy. But this exergy approach was not so easy to introduce in atmospheric energetics, since the temperature of the thermostat (which is the central concern of the exergy theories) must be replaced by the definition of a mere numerical value." (*Marquet*, 1991[2])

9. The available energy of Tailleux

Novak and *Tailleux* (2018) studied the available energy density for dry air, hydrostatic atmosphere, while *Tailleux* (2018) examined the local available energy of compressible stratified multicomponent fluids. Relying on the work of *Andrews* (1981) and *Holliday* and *McIntyre* (1981), they have defined the available potential energy by using simple physical principles, essentially the Archimedes' law. The available potential energy can be identified with the work which is necessary to bring an air parcel with fixed density from the reference state where it is in equilibrium to a state corresponding to the actual state of the atmosphere, against the buoyancy forces. This motion can be described with the equation:

$$\rho_r \frac{\mathrm{d}w}{\mathrm{d}t} = (\rho - \rho_r)g\,, \tag{51}$$

where ρ_r and ρ are the density of the parcel and the density of the environmental atmosphere, respectively. The specific buoyancy force is

$$\frac{\mathrm{d}w}{\mathrm{d}t} = \frac{\rho-\rho_r}{\rho_r}g\,, \tag{52}$$

and the work performed against it is

$$E_a = -\int_{z_r}^{z} \frac{\rho - \rho_r}{\rho\rho_r}\rho g \mathrm{d}z = \int_{p_r}^{p}\left(\frac{1}{\rho_r} - \frac{1}{\rho}\right)\mathrm{d}p = \int_{p_r}^{p}(\alpha_r - \alpha)\mathrm{d}p\,. \tag{53}$$

The crucial point of this definition is the choice of the reference state as well.

[2] A new (2014) version of the original paper is available on the webpage of the **author** with valuable new comments. http://www.umr-cnrm.fr/spip.php?article833&lang=en

Tailleux (2018) studied the local version of APE which includes diabatic sinks and sources. For simple compressible fluids, the total potential energy of the air portion is the sum of the available elastic energy and the APE. These energies represent the adiabatic shrinkage or expansion work required to move from the reference pressure to the actual pressure. Tailleux writes the APE formula using primitive equations of motion, which is simpler and more clearly visible than the previously published formulas for the relationship between the APE (density given by the Boussinesq approximation) and the basic equation of hydrostatics. The key step was to introduce a hybrid function of β depending on thermodynamic coordinates and altitude, which reminds the non-kinetic energy in the Bernoulli equation, which is actually the sum of the classical potential energy and a $\frac{p_0}{\rho}$ term[3]. According to the definition of Tailleux, β concerns the actual state, while β_r is for the reference state, and it can be expressed in the following forms:

$$\beta(z, S_i, s, p) = \Phi(z) + e_{th}(S_i, s, p) + \frac{p_0(z)}{\rho(S_i, s, p)}, \tag{54}$$

$$\beta_r(z_r, S_i, s, p_r) = \Phi(z_r) + e_{th}(S_i, s, p_r) + \frac{p_0(z_r)}{\rho(S_i, s, p_r)}, \tag{55}$$

where e_{th} is the specific internal (thermal) energy, S_i denotes the components of the fluid, the meaning of the other quantities are usual, and the variables with indices *r* stand for variables of the reference state. Tailleux proved that $\Pi = \beta - \beta_r$ quantity is positive definite and gives the potential energy density.

In this context, it clarifies the relationship between the Boussinesq approximation and the energetics of stratified fluids and shows the physical background underlying the choice of reference state in the local APE theory.

10. The approach of the moist atmosphere

Cyclones of the midlatitudes strongly influence the climate. In today's climate change, it is important to understand the relationship between the climate and the energies which drive the atmospheric processes. Besides the (vertical and meridional) temperature gradients, the moisture influences the APE. *Gertler* and *O'Gorman* (2019) found that increasing surface temperature causes increasing APE and decreasing meridional surface temperature gradient causes decreasing APE. The extratropical summer cyclones on the Northern Hemisphere are

[3] Batchelor calls the $\frac{p_0}{\rho}$ term as fictitious potential energy associated with the pressure field in his famous book: An Introduction to Fluid dynamics (2009 p 158).

weakening with the increasing temperature and moisture, however, despite the weakening, the convection intensifies.

The atmosphere at a given moment is determined by its mass and the field of velocity. This means that it depends on the distribution of ρ, T, p, and the phases of water, along with the wind components (*Lorenz*, 1979). Consequently, to use atmospheric energetics in the explanation of the real processes, the role of the moisture must be taken into account. The decisive step toward this was also taken by Lorenz (*Lorenz*, 1978; 1982). First, he elaborated a graphic procedure for determining the available energy of the moist atmosphere, and after it, he gave an algorithm for using this method in numerical calculations. The core problem is the determination of the reference state of the moist atmosphere, that cannot be determined as easily as in the dry case, by an analytical method according to entropy or humidity distribution, considered as state-of-the-art. However, finding the reference state is an analytical assignment problem, but it is computationally intensive. It is based on discretizing the atmosphere with equal mass domains and redistribute them by pressure. An additional difficulty is that with the addition of moisture, several minimal states could be created, consequently, it affects APE.

If the atmosphere is divided into parcels of equal mass, the changes in the atmosphere can be identified if the redistribution of these parcels is detected. The goal is to find the permutation of the parcels of the atmosphere with the least enthalpy (*Harris* and *Tailleux*, 2018). To be able to form parcels with equal mass, an x coordinate (following Lorenz) was created that covers different areas starting from the pole, but the mass belonging to them is equal. Parcels are characterized by the temperature T and by an indicator for the moisture, which can be, e.g., the specific humidity q or relative humidity f_r, these were zonally averaged over pressure levels. The Lorenz coordinate can be obtained:

$$x = -\frac{1}{2{R_E}^2\pi}\int_{\frac{\pi}{2}}^{\varphi}\int_0^{\pi} 2R_E cos\varphi \mathrm{d}\lambda R_E \mathrm{d}\varphi = -\frac{1}{2{R_E}^2\pi} 2{R_E}^2\pi[sin\varphi]_{\frac{\pi}{2}}^{\varphi} = \\ = -\left(sin\varphi - sin\frac{\pi}{2}\right), \tag{56}$$

$$x = 1 - sin\varphi\,, \tag{57}$$

where R_E is the radius of the Earth. The sum of the potential and internal energy equals the enthalpy, and it is the function of the thermodynamic variables, while the reference state is the minimum enthalpy one. While in the case of a dry atmosphere the enthalpy of the atmosphere is proportional to the sensitive heat, in the wet atmosphere the latent heat is added to the sensitive heat due to the phase transitions (*Lorenz*, 1979).

The calculation of moist available potential energy ($MAPE$) is based on Lorenz's numerical procedure, which relies on a graphical method elaborated also by Lorenz. The graphical method replaces the equation of a reversible

adiabatic process with the plotted state curve. The essence of this procedure is, as it was already mentioned, to divide the atmosphere into parcels by equal mass and to rearrange these parcels. In the wet atmosphere, the dynamics of the parcels are determined by three variables: the pressure, the temperature, and a measure of the humidity, which is, in this case, the relative humidity f_r, but it could be the specific humidity as well (*Lorenz*, 1978).

In the procedure, the atmosphere is divided into N equal masses, each p_n parcel has its p, T, and f_r. All the parcels together completely cover the whole atmosphere between p_A and p_B, it is assumed that the part of the atmosphere above p_B has such a small $MAPE$ that it is negligible. The space between p_A and p_B is divided vertically into M parts, while horizontally into L parts, so: $N = M * L$.

$$n = l * M + m\,, \tag{58}$$

where: $n \in N$, $0 \leq l < L$, and $0 < m \leq M$. The pressure of p_n parcel is chosen to be:

$$p_n = p_0 + n\Delta p\,, \tag{59}$$

where $p_0 = p_A - \frac{\Delta p}{2}$ and $\Delta p = \frac{p_B - p_A}{N}$. The pressure of the reference state is p_1, …, p_n, but the order is different, so the permutation of the actual state is needed (Lorenz, 1978).

The permutation can be obtained by finding the best algorithm, which sorts the parcels fast and accurately enough. This is the question of our time concerning MAPE.

Stansifer et al. (2017) calculated the exact minimum enthalpy of the atmosphere for three cases. Five parcel-sorting algorithms were applied: Munkres algorithm or so-called Hungarian method (*Kuhn*, 1955), divide-and-conquer algorithm, greedy algorithm, Lorenz's algorithm, and the *Randall* and *Wang*'s (1992) algorithm. They lighted upon that the Munkres algorithm is the most accurate, but if the computational speed is preferred, then the divide-and-conquer algorithm should be used.

Harris and *Tailleux* (2018) re-examined the result of *Stansifer et al.* (2017) and extended the list of the analyzed algorithms, these are the top-down-, bottom-up-, and Emanuel algorithm. They tested these algorithms for more than 3700 soundings, and they found that best solution of the calculation of the exact $MAPE$ is the Munkres algorithm, however, it has long runtime. When the approximation of the $MAPE$ is enough *Harris* and *Tailleux* (2018) suggest the use of the divide-and-conquer method.

There are cases, when some algorithms give negative $MAPE$ values, which means that the reference state has higher energy than the actual state. The divide-and-conquer algorithm sometimes gives back negative values, but rarer than the top-down or Lorenz' algorithms (*Harris* and *Tailleux*, 2018).

Peng et al. (2015) have chosen a reference state based on a model atmosphere, so it is independent from both the actual and the average state of the atmosphere. It shows that relying on the exergy theory, an arbitrary state can be defined as reference one.

It can be seen that in this area of atmospheric energetics, numerous open questions can be found, so it is not enough mature to be involved in the university curricula.

11. Summary

The atmospheric energetics was reviewed with particular attention to educational aspects. The decisive step of the development of atmospheric energetics was the introduction of the availability concepts. Having made this by Lorenz, in the development of the field, the global and local description of the energy cycle of the dry atmosphere was made, and recently the global and local description of the moist atmosphere is intensively investigated. The crucial question of these investigations is the definition and finding of the reference state. The deviation of the actual energy from it gives the available energy. Reference state should be chosen on physical considerations, so that it should be an equilibrium state of the atmosphere. However, applying the exergy concept makes it possible to choose a referential state arbitrarily. In our opinion, exergetics is a useful tool for the treatment of nonequilibrium thermodynamics, but for the atmosphere as a whole, it should be used only through analogies. We think that in the current state the basic results of atmospheric energetics are ripe to be involved in the university curricula. This is also supported by the development of computer technology, which enables the reproduction of numerical calculations on desktop computers based on the new databases. Equally important would be to incorporate the foundations of exergetic methods into atmospheric thermodynamics curricula.

Acknowledgement: Supported by the ÚNKP-20-3 New National Excellence Program of the Ministry for Innovation and Technology from the source of the National Research, Development and Innovation Fund. We thank the anonymous reviewer for his/her valuable remarks and suggestions.

References

Andrews, D., 1981: A note on potential energy density in stratified compressible fluid. *J. Fluid Mech.*, *107*, 227–236. https://doi.org/10.1017/S0022112081001742

Bejan, A. 2006: Advanced Engineering thermodynamics. Wiley, New Yersey. ISBN-13:978-0-471-67763-5

Callen, H.B., 1960: Thermodynamics, Wilkey and sons, London ISBN: 0471862568

Copernicus Climate Change Service (C3S), 2017: ERA5, Fifth generation of ECMWF atmospheric reanalyses of the global climate. Copernicus Climate Change Service Climate Data Store (CDS). https://cds.climate.copernicus.eu/cdsapp#!/home.

Czelnai, R., Götz, G., and *Iványi, Zs.* 1991: Bevezetés a meteorológiába II. A mozgó légkör és óceán. Tankönyvkiadó, Budapest, (Introduction to Meteorology II. The moving atmosphere and ocean.) Book number: J3-1344. (in Hungarian)

Dési, F. and *Rákóczi, F.*, 1970: A légkör dinamikája. Tankönyvkiadó, Budapest. in Hungarian (Dynamics of the atmosphere.) Book number: 42135. (in Hungarian)

Dincer, I. and *Rosen, M.A.*, 2007: Exergy. Elsevier, Amsterdam. ISBN: 978-0-08-044529-8

Dutton, J.A. and *Johnson, D.R.*, 1967: The Theory of Available Potential Energy and a Variational Approach to Atmospheric Energetics. *Adv. Geophys., 12,* 333–436. https://doi.org/10.1016/S0065-2687(08)60379-9

Dutton, J.A., 1973: The global thermodynamics of atmospheric motion. *Tellus, 25,* 89–110. https://doi.org/10.1111/j.2153-3490.1973.tb01599.x

Dutton, J.A., 1976*:* The Ceaseless Wind. McGraw Hill, USA. ISBN 0-07-018407-0

Dutton, J. A. 1992: Energetics with an entropy flavour. *Quart. J. Roy. Meteorol. Soc. 118,* 165–166. https://doi.org/10.1002/qj.49711850309

Gertler, C.G. and *O'Gorman, P.A.*, 2019: Changing available energy for extratropical cyclones and associated convection in Northern Hemisphere summer. *PNAS, 116,* 4105–4110. https://doi.org/10.1073/pnas.1812312116

Götz, G. and *Rákóczi, F.*, 1981: A dinamikus meteorológia alapjai. Tankönyvkiadó, Budapest. ISBN: 963 17 5580 0 (Foundations of the dynamic meteorology.)(in Hungarian)

Harmatha, A., 1982: Termodinamika műszakiaknak. Budapest, Műszaki Könyvkiadó. ISBN: 963-10-4467-X (Engineering Thermodynamics.) (in Hungarian)

Harris, B.L. and *Tailleux, R.*, 2018: Assessment of algorithms for computing moist available potential energy. *Quart. J. Roy. Meteorol. Soc., 144,* 1501–1510. https://doi.org/10.1002/qj.3297

Haywood, R.W., 1974a: A critical review of the theorems of thermodynamic availability, with concise formulations. Part 1. *J. Mech. Eng. Sci., 16,* 161–174. https://doi.org/10.1243/JMES_JOUR_1974_016_046_02

Haywood, R.W., 1974b: A critical review of the theorems of thermodynamic availability, with concise formulations. Part 2., *J. Mech. Eng. Sci., 16,* 258–267 https://doi.org/10.1243/JMES_JOUR_1974_016_046_02

Holliday, D. and *McIntyre, M. E.*, 1981: On potential energy density in an incompressible stratified fluid. *J. Fluid. Mech., 107,* 221–225. https://doi.org/10.1017/S0022112081001742

Holton, J.R., 2004: An introduction to Dynamic Meteorology. Elsevier, Amsterdam. ISBN: 0-12-354015-1

Hoskins, J.B. and *James, N.*, 2014*:* Fluid dynamics of the midlatitude atmosphere, Wiley Blacwell. ISBN 978-0-470-79519-4 https://doi.org/10.1002/9781118526002

Jacobs, S.S., Jenkins, A., Giulivi, C.F., and *Dutrieux, P.*, 2011: Stronger ocean circulation and increased melting under Pine Island Glacier ice shelf. *Nat. Geosci., 4,* 519–523. https://doi.org/10.1038/ngeo1188

Karlsson, S., 1990: Energy, entropy and exergy in the atmosphere (thesis). Chalmers Tekniska Högskola, Bibliotekets Reproservice, Göteborg. ISBN: 91-7032-526-X

Keenan, J., 1951: Availability and irreversibility in thermodynamics. *Br. J. Appl. Phys 2,* 183–192. https://doi.org/10.1088/0508-3443/2/7/302

Kucharski, F., 1997*:* On the concept of exergy and available potential energy. *Quart. J.Roy. Meteorol. Soc. 123,* 2141–2156. https://doi.org/10.1002/qj.49712354317

Kuhn, H.W., 1955: The Hungarian method for the assignment problem. *Nav. Res. Logist. Q., 2,* 83–97. https://doi.org/10.1002/nav.3800020109

Lorenz, E.N., 1955: Available Potential Energy and the Maintenance of the General Circulation. *Tellus, 7,* 157–167. https://doi.org/10.3402/tellusa.v7i2.8796

Lorenz, E.N., 1978: Available energy and the maintenance of a moist circulation. *Tellus,* 30, 15–31. https://doi.org/10.3402/tellusa.v30i1.10308

Lorenz, E.N., 1979: Numerical evaluation of moist available energy. *Tellus, 31,* 230–235. https://doi.org/10.3402/tellusa.v30i1.10308

Lorenz, E.N., 1982: Low-order models of atmospheric circulations. *J. Meteorol. Soc. Japan 30,* 15–31. https://doi.org/10.2151/jmsj1965.60.1_255

Major, Gy., Nagy, Z., and *Tóth, Z.* 2002: Magyarországi éghajlat-energetikai tanulmányok. A Budapesti Közgazdaságtudományi és Államigazgatási Egyetem Környezettudományi Intézetének tanulmányai. Budapest. ISBN: 963-503-273-0 (Hungarian climate energy studies.) (in Hungarian)

Mak, M., 2011: Atmospheric Dynamics. Cambridge Univ. Press. ISBN: 978-0-521-19573-7

Makainé, Cs., M., 1971: A közepes energetikai szint néhány statisztikai és szinoptikai sajátossága. *Időjárás, 75,* 349–360. (Some statistical and energetical properties of the average energetical level.) (in Hungarian)

Makainé, Cs., M., 1972: Orográfiai hatások elemzése a hasznositható potenciális energia és kinetikus energia változásában. *Időjárás, 76.,* 334–340. (Analisys of orografical influences of the variation of the available potential and kinetic energy.) *(*in Hungarian)

Makainé, Cs., M., 1974: A barotrop légkör energetikai aktivitásáról. *Időjárás, 78.,* 109–115. (On the energetical activity of barotropic atmsosphere.) (in Hungarian)

Margules, M., 1906: The last paper "On the theory of storm" (Zur Sturmtheorie). *Meteorol. Z. 23,* 481–497. translated by *Marquet, P.* in 2017.

Margules, M., 1910: The mechanical equivalent of any given distribution of atmospheric pressure, and the maintenance of a given difference in pressure. *Smithsonian Miscellaneous collection 54,* 501–532.

Marquet, P., 1991: On the concept of exergy and available enthalpy: Application to atmospheric energetics. *Quart. J. Roy. Meteor. Soc. 117,* 449–475. https://doi.org/10.1002/qj.49711749903

Mulligan, J.F. and *Hertz, H.G.,* 1997: An unpublished lecture by Heinrich Hertz: "On the energy balance of the Earth''. *Am. J. Phys, 65,* 36–45. https://doi.org/10.1119/1.18565

Novak, L. and *Tailleux, R.,* 2018: On the local view of atmospheric available potential energy. *J. Atmos. Sci., 75,* 1891–1907. https://doi.org/10.1175/JAS-D-17-0330.1

Oort, A., 1971: The observed annual cycle in the meridional transport of atmospheric energy. *J. Atmos. Sci. 28,* 325–339.https://doi.org/10.1175/1520-0469(1971)028<0325:TOACIT>2.0.CO;2

Panchev, S., 1985: Dynamic Meteorology. D. Reidel Publishing Co. Kluwer, ISBN 90-277-1744-1 https://doi.org/10.1007/978-94-009-5221-8_1

Peng, J., Zhang, L., and *Zhang, Y.,* 2015: On the local available energetics in a moist compressible atmosphere. *J. Atmos. Sci., 72,* 1551–1561. https://doi.org/10.1175/JAS-D-14-0181.1

Práger, T., 1982: Numerikus Prognosztika I. Tankönyvkiadó, Budapest (Numerical prognostics I.) Book number: J3-1244.(in Hungarian)

R Core Team, 2017: R: A language and environment for statistical computing. R Foundation for Statistical Computing, Vienna, Austria. https://www.R-project.org/.

Randall, D.A., and Wang, J., 1992: The moist available energy of a conditionally unstable atmosphere. *J. Atmos. Sci. 49,* 240–255. https://doi.org/10.1175/1520-0469(1992)049<0240:TMAEOA>2.0.CO;2

Schulzweida, U., 2019: CDO User Guide. 1–206. https://code.mpimet.mpg.de/projects/cdo/embedded/cdo.pdf

Shepherd, A. and *Wingham, D.,* 2007: Recent sea-level contributions of the of the Antarctic and Greenland ice sheets. *Science 315,* 1529–1533. https://doi.org/10.1126/science.1136776

Stansifer, E.M., O'Gorman, P.A., and *Holt, J.I.,* 2017: Accurate computation of moist available potential energy with the Munkres algorithm. *Quart. J. Roy. Meteor. Soc., 143,* 288–292. https://doi.org/10.1002/qj.2921

Su, Z., and Ingersoll, A.P., 2016: On the minimum potential energy state and the eddy size-constrained ape density. *J. Phys. Oceanogr., 46,* 2663–2674. https://doi.org/10.1175/JPO-D-16-0074.1

Tailleux, R., 2013: Available potential energy and exergy in stratified fluids. *Annu. Rev. Fluid Mech., 45,* 35–58. https://doi.org/10.1146/annurev-fluid-011212-140620

Tailleux, R., 2018: Local available energetics of multicomponent compressible stratified fluids. *J. Fluid Mech., 842,* R1. https://doi.org/10.1017/jfm.2018.196

Trenberth, K.E., Fasullo, J.T., and *Balmaseda, M.A.,* 2014: Earth's energy imbalance. *J. Climate, 27,* 3129–3144. https://doi.org/10.1175/JCLI-D-13-00294.1

Van Mieghem, J., 1973: Atmospheric Energetics. Clarendon Press, Oxford, UK, ISBN 10: 0198516053

Wiin-Nielsen, A. and *Chen, T.C.,* 1993: Fundamentals of Atmospheric Energetics. Oxford and New York and Oxford, ISBN 0-19-507127-1

Zdunkowski, W. and *Bott, A.* 2003: Dynamics of the atmosphere. Cambridge Univ. Press. ISBN-13: 978-0-52100666-8 https://doi.org/10.1017/CBO9780511805462

Appendix A. Entropy and energy calculation

The appendix summarizes the numerical procedures, databases, and software, which were applied in the calculations, the results of which are presented in *Figs. 3–6* and in *Table 2*.

The target area was the Northern Hemisphere on 1°×1° spatial resolution, vertically 19 pressure levels were used (1000–100 hPa by 50 hPa). The examined time period was 1979–2019. The meteorological dataset used in this study was the product of the European Centre for Medium-Range Weather Forecasts (ECMWF), the ERA5. The ERA5 database is the fifth generation of the ECMWF reanalysis, available from 1979 with relatively small delay. ERA5 provides in atmospheric, terrestrial, and oceanic data hourly approximation. It combines large amount of historical observations (satellite and in-situ) with global modeling with advanced modeling and data assimilation systems. ECMWF data is available in NetCDF (network common data form) form, which is advantageous, because such format is suitable for storing array information (*Copernicus Climate Change Service*, 2017).

Monthly averages were calculated by using a free software called CDO (Climate Data Operators) developed by the Max Planck Institute (*Schulzweida*, 2019).

The obtained data were processed with the R program (*R Core Team*, 2017). With the help of this software, calculations and representations were also made.

T_r was calculated numerically from Eq. (43):

$$\frac{1}{T_r} = \frac{1}{\Delta t}\int_{t_1}^{t_2}\left[\iiint \frac{1}{T}\frac{dm}{M}\right]dt = \frac{1}{\Delta t}\int_{t_1}^{t_2}\frac{1}{T_{m(t)}}dt\,, \qquad (A1)$$

where T_r is a characteristic value of the terrestrial atmosphere, which remains close to 250 K under current climatic conditions.

Entropy was calculated by using Eq. (39), where the second (pressure dependent) term diminishes after the integration, because:

$$\int_{V_A} R\ln\left(\frac{p}{p_r}\right)dV = \frac{R}{g}\int_A d\lambda d\varphi \int_0^{p_0}\ln\left(\frac{p}{p_r}\right){R_F}^2 cos\varphi dp =$$
$$= \frac{R}{g}\int_0^{p_0}\ln\left(\frac{p}{p_r}\right)4{R_F}^2\pi dp = \frac{R}{g}4{R_F}^2\pi\left(-\int_{p_0}^{0}\ln(p)dp + \int_{p_0}^{0}\ln(p_r)dp\right) =$$
$$= \frac{R}{g}4{R_F}^2\pi\left(-p_0\ln(p_r) + p_0\ln(p_r)\right) = 0\,. \qquad (A2)$$

Total energy of the atmosphere was calculated as follows:

$$e_{total} = c_p T + \frac{1}{2}\mathbf{v}^2. \quad (A3)$$

If we integrate over the atmosphere, we get the energy and the entropy for the atmosphere:

$$E_{total} = \frac{1}{g}\sum e_{total}\, {R_E}^2 cos\varphi \mathrm{d}\lambda \mathrm{d}\varphi \mathrm{d}p, \quad (A4)$$

$$S = \frac{1}{g}\sum s_T\, {R_E}^2 cos\varphi \mathrm{d}\lambda \mathrm{d}\varphi \mathrm{d}p, \quad (A5)$$

where g = 9.81$\frac{m^2}{s}$, the gravitational constant, R_E (= 6370 km) is the radius of the Earth, λ is the longitude, and φ is the latitude, so dλdφ = 1°×1° due to the resolution.

a_h is available from Eq. (29), a_p is calculated by Eq. (32), and a_T is reached after simplifying Eq. (31):

$$a_T \approx c_p \frac{(T - T_r)^2}{2T_r}. \quad (A6)$$

DOI:10.28974/idojaras.2021.3.2

IDŐJÁRÁS

Quarterly Journal of the Hungarian Meteorological Service
Vol. 125, No. 3, July – September, 2021, pp. 397–418

Validation of subgrid scale ensemble precipitation forecasts based on the ECMWF's ecPoint Rainfall project

Boglárka Tóth and **István Ihász***

Hungarian Meteorological Service,
P.O. Box 38, H-1525 Budapest, Hungary

Corresponding author E-mail: ihasz.i@met.hu

(Manuscript received in final form January 11, 2021)

Abstract— Nowadays, state-of-the-art numerical weather prediction models successfully predict the general weather characteristics several days ahead, but forecasting extreme precipitation is quite challenging even in the short time range. In the framework of the ecPoint Project, the European Centre for Medium-Range Weather Forecasts (ECMWF) developed a new innovative probabilistic post-processing tool which produces 4-day precipitation forecast as accurate as the raw ensemble forecast at day 1. In the framework of the scientific co-operation between ECMWF and the Hungarian Meteorological Service (OMSZ), we were invited to participate in the validation of the experimental products. Quasi operational post-processed products have been available since July 1, 2018. During our work, besides using different verification technics, a new ensemble meteogram was also developed which can support operational forecasters during extreme precipitation events. As a result of our work, products of the ecPoint Project have been included in the operational forecasting activity.

Key-words: extreme events, ensemble forecasts, post-processing, calibration, precipitation, probability, numerical weather prediction models, early warning, case studies, ECMWF

1. Introduction

On July 1, 1994, the cooperation agreement between Hungary and ECMWF entered into force. Since then, it has proved very beneficial for a wide range of activities, including the contributions the Hungarian Meteorological Service (OMSZ) has made to several developments at ECMWF (*Ihász* and *Modigliani*, 2019). In the summer of 2018, OMSZ was invited to take part in the validation of the ecPoint Rainfall project lead by the European Centre for Medium-Range Weather Forecasts (ECMWF).

In the framework of the ecPoint Rainfall project, ECMWF has developed a probabilistic point-rainfall product which could support the prediction of flash floods across the globe (*Pillosu* and *Hewson*, 2017). The product, which is based on an innovative post-processing method, aims to bridge the gap between the relatively coarse resolution of today's global forecasting models and the higher-resolution limited-area models needed to describe localized heavy rainfall. The methodology is based on physically relevant statistical relationships between the larger-scale weather features well represented by ECMWF forecasts and local realizations represented by point observations. These relationships make it possible to compute statistically based (rather than raw-ensemble-based (*Mátrai* and *Ihász*, 2017; *Ihász et al.*, 2018)) probabilities for point rainfall. This includes extremes, which can be used to infer the likelihood of flash floods for use on platforms such as the European and Global Flood Awareness Systems (*Hewson et al.*, 2019).

This new post-processing method blends together information from different locations whenever they experience similar rainfall generation mechanisms, assuming that these physical mechanisms are universal and dependent on key atmospheric and geographic properties (*Hewson* and *Pillosu*, 2020). This means that:

- one year of global rainfall observations is adequate, because it can equate to hundreds of years used in locally-calibrated techniques, and
- extremes can be successfully predicted, even when they do not exist in a local record.

Moreover, the reliance on physics means that forecasts can be confidently produced for anywhere in the world, even places without observations. The post-processing system has been fully automated and requires minimal computing resources to run compared to high-resolution numerical models (*Hewson* and *Pillosu*, 2021).

One of the most important benefits of this innovation is that it does not need long timeseries as most of the post-processing technics required in the last several decades. During post-processing which required long timeseries, reforecast dataset was needed due to regular model developments, but in the other hand the lack of the continuous high quality observation is a typical and

unsolved problem. Post processing technics based on ECMWF model using reforecasts could not be a problem as 20 years of reforecasts are operationally available, but comprehensive observation precipitation datasets can be a serious problem in Europe, including Hungary too, because extreme precipitation is typically concentrated on a very small region.

2. Former developments aiming to improve precipitation forecasts

2.1. Using numerical model products at the eighties

Necessity of the study of meteorological and hydrological circumstances of floods on two main rivers (Danube and Tisza) got a special emphasize after a severe flood event on Tisza, which caused extreme damages in spring 1970 (*Bonta* and *Újváry*, 2011). In the middle of the 1970s, several projects were realized to study the weather scenarios causing heavy floods. As model forecasts from large European meteorological services were available only in the beginning of the 1980s, a statistical method was constructed to estimate the precipitation amount (*Bodolainé*, 1983).

Since the ‘70s, at the largest meteorological services global models have been operationally running, and relatively few countries were able to run regional models providing downscaled weather forecasts. In the ’80s, due to the rapid development of limited area regional models, significant benefits could be provided especially in surface weather parameters, like precipitation, 10m wind, and 2m temperature compared to global forecasts. Consequently, the Hungarian Meteorological Service (OMSZ) considered to implement a state-of-the-art model in the second part of the 1980s,

2.2. Using limited area models since early nighties

At the end of the 1980s, the use of limited-area models (LAMs) became a key element in operational weather forecasting in some European countries. At the time, the Swedish grid point LAM was one of the best, specially precipitation forecasts were quite good comparing to other models. OMSZ acquired it in 1988. Dezső Dévényi headed a small new team focusing on this activity. Having solved several problems, in July 1991, a version of the model with a horizontal resolution of 0.9°x0.9°covering Europe and 12 levels in the vertical became operational at OMSZ (*Ihász*, 1992). At that time, it was not possible to obtain adequate lateral boundary conditions from the Global Telecommunication System (GTS). There was an obvious solution to this problem: to use ECMWF data as lateral boundary conditions.

Among one of his first activities, Iván Mersich, the new president of OMSZ, sent an application by the Hungarian Meteorological Service to join ECMWF as a member (*Woods*, 2005). In the event, a cooperation agreement between ECMWF and Hungary was signed in the spring of 1994 (*Kaba*, 1994). Lateral boundary conditions then became available and were used operationally in the LAM model. This development led to significantly improved forecast quality for the rest of the life of this LAM, until 1998 (*Ihász*, 2014).

Hungary was one of the first countries to participate in the ALADIN project led by Météo-France since 1991 (*Horányi et al.*, 1996*; Horányi et al.*, 2006). In 1998, the ALADIN/HU model became operational at OMSZ, on a new high-performance computing facility. In the first ten years of operations, the model was coupled to the global ARPEGE model. It was then coupled to ECMWF's deterministic global model, resulting in significant improvements in the quality of the forecasts provided by OMSZ (*Bölöni et al.*, 2009).

Since 2009, OMSZ has been running the ALADIN model with 11 ensemble members (*Horányi et al.*, 2011). In 2016, ECMWF started to provide ensemble lateral boundary conditions in the framework of the Boundary Condition (BC) Optional Programme. OMSZ has been using them ever since, thus improving the quality of its probabilistic forecasts (*Szűcs et al.*, 2016).

In the first decade of this century, the AROME non-hydrostatic model was developed in the framework of international cooperation. In 2010, the AROME model was made operational at OMSZ (*Mile et al.*, 2015*; Szintai et al.*, 2015). This non-hydrostatic model provides very useful information, especially on extreme precipitation events in summer.

2.3. Ensemble product development

Over the last 25 years, OMSZ has worked in various areas of product development. They include many pioneering activities in the use of ensemble forecasts, a special attention was paid to improve quality of the precipitation forecasts. Since 2003, ensemble clustering focusing on Central European meteorological patterns has been run operationally using resources provided by ECMWF's ecgate computing cluster (*Ihász*, 2004). This system makes available the representative ensemble member and the ensemble mean for each cluster to the General Directorate of Water Management. OMSZ has also been able to significantly improve the quality of the ensemble forecasts by means of calibration for variables such as 2-meter temperature, 10-meter wind speed, and precipitation (*Ihász et al.*, 2010*; Mátrai and Ihász*, 2017*; Ihász et al.*, 2018).

Since 2011, OMSZ has developed ensemble vertical profiles (*Ihász* and *Tajti*, 2011). These can support decision-making for precipitation type in winter and for the intensity of convective events in summer. In 2018, ECMWF developed a similar method for the ecCharts visualization system.

The version of ECMWF's Integrated Forecasting System introduced operationally in May 2015 (IFS Cycle 41r1) contained precipitation type as a new experimental product (*Forbes et al.*, 2015). At OMSZ, an ensemble precipitation type diagram was developed in autumn 2015 supporting the forecasters' decision making during the winter season. A similar ECMWF product was created in the framework of the EU-funded ANYWHERE project inspired by the bar chart product from OMSZ, exploiting the probabilistic information provided by ECMWF ensemble forecasts (*Gascon et al.*, 2018).

3. Study of the subgrid scale ensemble precipitation forecast based on the ecPoint Rainfall project

Forecasts of the precipitation amount and intensity are the most important challenges for the meteorologists; furthermore, the correct estimates are not negligible from the perspective of the society. Nowadays, when extreme storms are becoming common, one of the most relevant tasks is the most accurate prediction of convective rainfall. To make such predictions, forecasters use numerical model outputs, which often over- or underpredict the real measurements. Naturally, the resolution of the models significantly contribute to these inaccuracies, so the high resolution non-hydrostatic models, which describe the vertical upflow in an explicit way, give assistance to the convective predictions. Taking into account this information, there are excessive expectations of the local, extreme precipitation forecast, mostly in areas with complex orography, because the subgrid variability is difficult to represent.

The problem is exacerbated by the appearance of extreme weather conditions, which occur in significant numbers annually in Hungary. In such extreme situations, over a short period of time, huge precipitation is registered locally, which often results in flash flood events. A number of stations do not prepare for such suddenly forthcoming disasters, hence vast damages can happen in a few hours. Currently, the forecasters alarm for these situations by using the output of the high-resolution nonhydrostatic limited-area model and radar nowcasting on ultra-short range. This solution also holds some difficulties; for example, the warning lead time is reduced to only a few hours. At OMSZ, forecasters make warning up to four days. These warnings are based typically on ECMWF's high resolution and ensemble models.

To eliminate these problems, ECMWF developed a new post-processing method within the framework of the project ecPoint Rainfall (*Hewson* and *Pillosu*, 2020) between 2015 and 2018, that could support the more accurate prediction of extreme local precipitation across the globe. The new post-processed rainfall forecast is also called ecPoint Rainfall, which is a probabilistic product based on the ensemble forecasts.

3.1. The ecPoint Rainfall project lead by ECMWF

The new post-processing method developed by ECMWF usually warns about heavy rainfall earlier and more precisely than previous forecast systems. This ability plays a particularly important role in the estimation of flash flood events, which are one of the most devastating hazards, especially in mountainous areas. As ecPoint Rainfall is a global product, for the research it was worth to select partner countries from different climatic areas to see if the method performed similarly well in different locations. Only four countries joined the project, thus it was an outstanding honor that beside Costa Rica, Ecuador, and Peru, the Hungarian Meteorological Service could participate in the ecPoint Rainfall research as well, representing the areas of continental climate. With the accession, OMSZ gained a number of advantages – as opposed to non-participating countries –, including the GRIB files have been received from ECMWF and have been archived, which allowed this study to be completed.

The aim of ecPoint Rainfall is to offer some information on the probability of precipitation in the sub-grid area, because most users would like to know the expected weather at a specific location instead of an average value per gridbox (*Owens and Hewson*, 2018). The calibration of ensemble forecasts are taken as a basis in the method, which uses 5 different meteorological parameters (convective fraction, total precipitation, 700 hPa wind, convective available potential energy (CAPE) index, and 24 hour incident clear sky solar radiation) with appropriate emphasis to produce the 99 members of ecPoint Rainfall data set. In summary, with the new methodology we can estimate the range of total precipitation in the grid box and derive the probability value of different points within the grid using different statistical methods. During the one-year-long calibration, the short-term 12 hours rainfall forecasts were compared with synoptic observation data, and a forecasts error ratio (FER) was computed for each forecast. Since then, with proper use of FER, they have been improving the original ensemble predictions for anywhere on Earth based on an algorithm that learns the past.

3.2. Studies based on ecPoint Rainfall forecasts

In this study, first we examined the reliability of ecPoint Rainfall, for which Talagrand diagrams were made. Days were separately analyzed with extreme rainfall in 2018, and then they were evaluated the success of the new product using a verification algorithm. After the verifications, the new ensemble meteogram was reviewed. Last but not least, through a case study we described the benefits of the new ecPoint Rainfall product.

3.3. *Verification*

In case of every new product, including the ecPoint Rainfall project, it is vital to gain understanding of the reliability of the results. In order for all the new information to be applied in the most appropriate way in operational activities, it is necessary to review the main advantages and sources of error of ecPoint. For this purpose, first, a verification was made of the 2018 summer period (*Tóth*, 2020).

In the course of this research, we took into account those synoptic observation stations in Hungary, where a 12-hour precipitation amount can be derived. Thus, we were able to work with the verified data of a total of 310 stations that the Unit of Informatics Applications of the Hungarian Meteorological Service provided for us. To display the scattered observation stations on a map, the MAGICS software was chosen (*Fig. 1*). The map represents an inhomogeneous distribution, which is justified by the topography of Hungary. To separate the lowland stations from the hilly stations, we used various symbols and colors. The lowest measuring points were indicated with green, while those located higher than 600 meters with black.

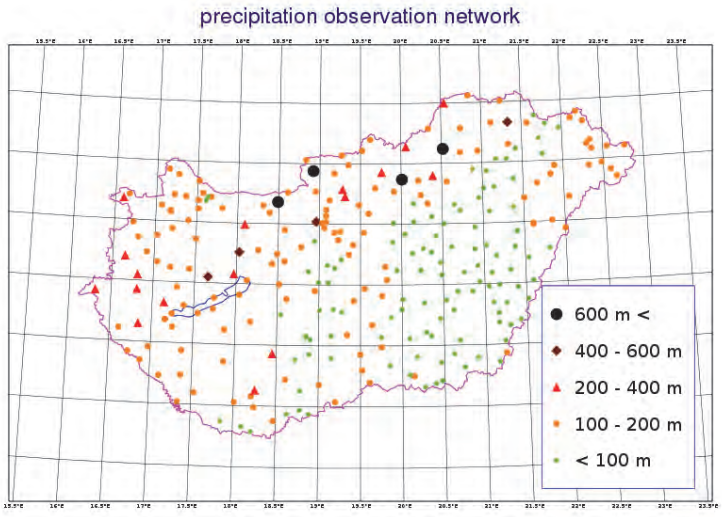

Fig. 1. Network of precipitation measurements in Hungary.

In addition to observation data, the 12 hours ecPoint Rainfall forecasts and ensemble forecasts have been used for verifications as well. All examinations

were made for the summer of 2018. First, the Talagrand diagrams were based on the +12 hours forecasts, then the diagram pairs were extended to a higher time step, so the verification of the +12, +36, +60, +84 and +108 hours forecasts were also completed.

The values of the horizontal axis of the Talagrand diagram are determined by the values of the sorted probability predictions. For the 99-member ecPoint Rainfall, the x values are specified by nearly 2 forecast values. Thus, on the x-axis - corresponding with the professional literature – the number of the ensemble member is displayed. The columns show the relative frequency of cases where the measured values fall between two adjacent ensemble members. A probabilistic prediction is applicable if all values can occur with nearly equal probability. As a result, if the Talagrand diagram shows a smooth, flat shape, the forecast is considered reliable. If outliers appear on either of the edges of the chart, i.e., the figure becomes L or J shaped, then the possibility of a systematic underestimation or overestimation should be taken into consideration. If this problem exists on both sides, then the measured values are mostly outside the range of probability predictions, and it becomes practical to extend the range of the ensemble.

Not all of the completed diagrams are presented as almost the same structure appeared in the figures, so for the sake of illustration, we only analyze the Talagrand diagrams made from the +12 hours (*Fig. 2*) and +108 hours (*Fig. 3*) forecasts.

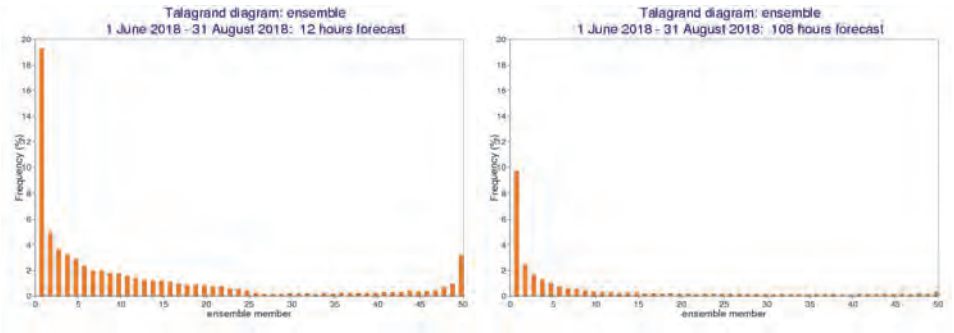

Fig 2. Talagrand diagrams of 12 hours forecast for ecPoint Rainfall (left) and ensemble foreast (right). The investigated time interval is June 1, 2018 –August 31, 2018.

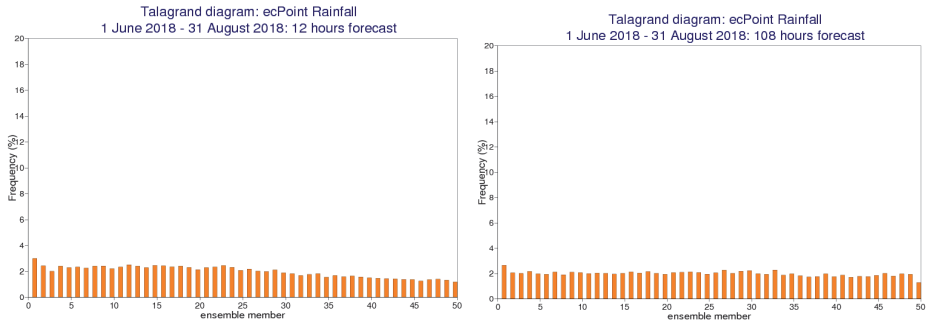

Fig. 3. Talagrand diagrams of 108 hours forecast for ecPoint Rainfall (left) and ensemble forecast (right). The investigated time interval is June 1, 2018 –August31, 2018.

Summarizing the verification diagrams, it was demonstrated that the ecPoint Rainfall forecasts proved to be much more reliable in the period we examined than the ensemble forecasts for both low and high ensemble serial numbers. In the Talagrand diagram, each value occurred with a relative frequency of 2–4%, suggesting low systematic failures of ecPoint Rainfall. Meanwhile, on the ensemble Talagrand diagrams an L-shape stands out, alluding to a systematic overestimation. If we compare the chart made from the +12 hours forecasts with the +108 hours forecast, significant differences can not be determined; however, a less wavering form is outlined. As the ECMWF ensemble model targeting to provide good quality in medium range (2–10 days) ensemble precipitation forecasts have typically less wide ensemble-spread than it is needed in ultra-short range or short range scales.

After that, we have started to examine days of extreme rainfall in Hungary. We selected those days when the observed precipitations exceeded the 20 mm/12 hours limit from the 92 days of the summer of 2018 at any of the 310 stations examined in our research. If the precipitation anywhere in the country exceeded the predefined limit, it was already included in the extreme days. Firstly, we studied the interval from midnight to noon and we found 24 days of extreme rainfall. Then we used the same algorithm searching for extremes in the ecPoint database as well.

The ecPoint Rainfall is a post-process ensemble output that consists of 99 members, so we were looking for days in excess of 20 mm precipitation for different percentiles. Based on our research, we determined that the use of the 85th percentile level is one of the most optimal values, because in this case the ecPoint Rainfall warns of almost all extreme events, meaning its predictions do

not significantly differ from reality. So when we used the 99th percentile level, we found more extreme events than in the observed database, and towards the smaller percentile levels we found fewer. (The study of extreme rainfall days was also performed for several precipitation limits.)

After filtering out the days of extreme rainfall, we displayed them on both the observation and the ecPoint Rainfall database and made subjective verifications. From the 24 extreme rainy days, we analyzed an event occurred on June 9, because several consecutive thunderstorm systems arrived in Hungary on this day. The morning thunderstorms arriving from the south concentrated between the Danube and the Tisza, where 60 mm/12 hours rainfall was measured (*Fig. 4*). At the same time, there was cloudless, sunny weather in the eastern, northeastern regions of the country.

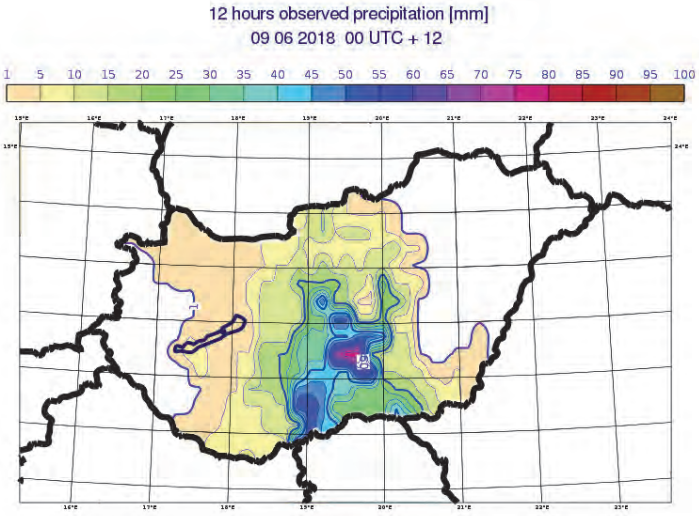

Fig 4. Observed 12h amount of precipitation at 12 UTC, June 9, 2018.

If we examine the short-term +12 hours forecasts of one of the most optimal percentiles, i.e., the 85th ecPoint Rainfall member, we can see that an intense rainfall covering a large area was expected in the central and western parts of Hungary. On the map made from ecPoint Rainfall data (*Fig. 5*), the rainy areas are nicely outlined, similarly to the map containing the measured values. Naturally, the model forecast designates a somewhat wider zone than was affected in reality, but in terms of its structure, it assigned the rainy and dry areas precisely.

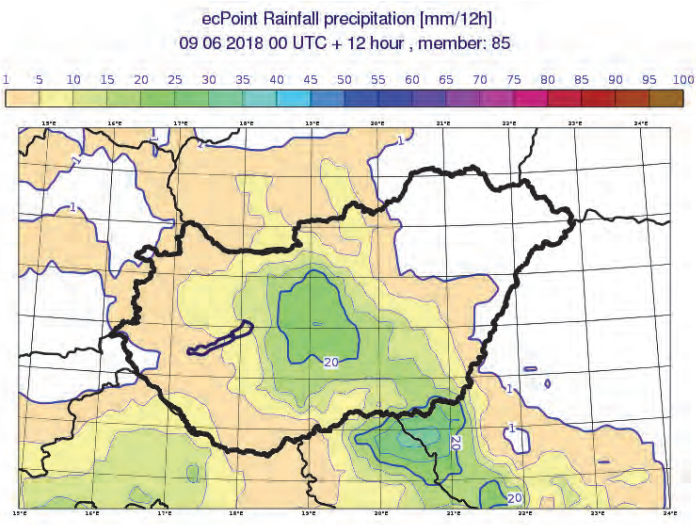

Fig. 5. 12h amount of precipitation provided by the 85th member of ecPoint Rainfall at 12 UTC, June 9, 2018.

Analyzing the 24 cases, the results showed that the position error is typically smaller over mountainous areas than over flat areas; however, ecPoint Rainfall provides more precise forecasts for frontal systems and squall lines. This can be explained by the fact that in the lowland, the orographic force does not play a significant role in the formation of thunderstorms, thus the locations of extreme precipitation become random. Even in the case of locally occurring thunderstorms, the new product provided excellent estimates of precipitation at the regional level, and its various percentiles also adequately warned of the likelihood of more extreme precipitation.

Following the visual analysis of the maps, we invented a new kind of scoring technique for the verifications, which can also illuminate the spatial accuracy of the ecPoint Rainfall. Before we started the verification study, we interpolated the observation values to a grid of ecPoint Rainfall with a spatial resolution of 0.16×0.16. During the interpolation, we fitted each measured value to the closest grid point, as long as it did not exceed a distance of 25 km. With this solution, we tried to avoid substituting missing data areas with false values. After the interpolation, the data were available on the same grid, so the spatial accuracy had become verifiable.

The success of the forecasts had been assessed with a point system within the predefined threshold index of precipitation. If the value of the measured and the ecPoint member remained below the threshold index, we gave 0 point, if it

exceeded it, we gave 1 point. If the two data differed in their estimation in either direction, we gave -1 point. Upon the summation of these points, we displayed them on a map using the MAGICS program. The ecPoint Rainfall performed well in areas where the figures were dominated by positive values; however, where the negative values prevailed, the forecasts were less accurate. We obtained an almost homogeneous map with a value of around 0 point. This was the first attempt to compare forecasts to observed values. The deviation between one observed grid point and one forecasted grid point was examined.

Since a forecast can be accepted even if it predicts extreme precipitation amounts a few grid points away, it has become expedient to further develop the new verification method. In the following, we did not examine a specific grid point, but a specific area. Firstly, we compared one forecasted gridpoint to 5 surrounding grid points in each direction (i.e., 11*11 grid points). The area used in the examination of the success of the forecast became an area with a diameter of almost 200 km. On the maps made this way, we drew only values above 0 in order to provide a better illustration. As a result, we achieved much more encouraging results, because the areas with a positive score dominated across the country. Regions where ecPoint Rainfall underestimated or overestimated the measured values remained white.

As the aim of the new product is to forecast the local precipitation zones as accurately as possible, it was worth narrowing the deviation of 5–5 grid points and examining the results of ecPoint Rainfall under even stricter conditions. Under this, we compared one forecasted grid point to 3 observed grid points in each direction (i.e., 7*7 grid points, approximately 50 km in each direction).

The results thus obtained were also quite encouraging. The maps were prepared for several ecPoint Rainfall members for different precipitation thresholds as well, of which a map representing the 85th and 95th percentiles belonging to the 15 mm threshold index was presented. The ranges with a positive score were slightly narrower compared to the maps that allowed a deviation of 5–5 grid points (based on the maps for the 85th member) (*Fig. 6*); however, excluding the Great Plain areas, the performance of ecPoint Rainfall still dominated.

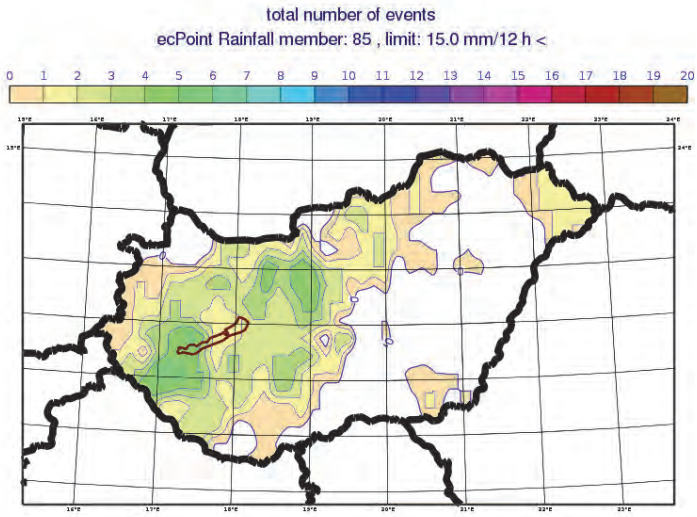

Fig. 6. Total number of events for the 85th member of ecPoint Rainfall exceeding 15 mm/h.

Because the members of ecPoint Rainfall are sorted probability members, the higher percentiles belong to higher precipitation amounts. It is no accident that higher scores appeared on the map for member 95, as there were several events when the ecPoint rainfall forecast exceeded the predefined threshold index (*Fig. 7*).

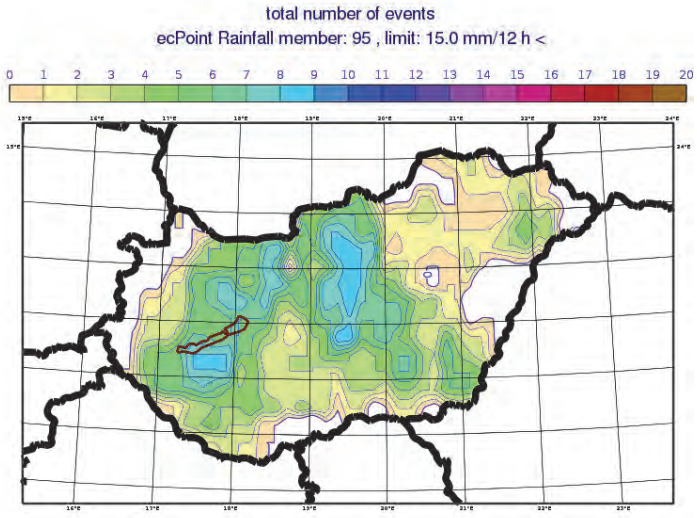

Fig 7. Total number of events for the 95th member of ecPoint Rainfall exceeding 15 mm/h.

It is worth highlighting that the higher percentile members often overestimate the real measurement, thereby larger areas are marked with positive points. These members estimate more extreme precipitations in a wider band. To conclude, the spread of the ecPoint Rainfall probability forecast informs the forecasters from the most favorable conditions to the most extreme events. Based on the new verification method, it can also be established that the 85th member provides one of the most optimal forecasts.

In the second half of the study, we began to deal with the under- and overestimation of ecPoint Rainfall. Using an algorithm similar to the previous verification, we developed a point-based verification method to determine the extent of under- and overestimations for extreme rainy days. If the value of the measured and the ecPoint member remained below or exceeded the threshold index, we gave 0 point for the forecast. In cases where the observation values were below the selected threshold index while the ecPoint Rainfall values were above, we gave 1 point; otherwise, we gave -1 point for the given forecast. During this verification examination, we allowed 3–3 grid point deviations in each direction from the given grid point, and then we summed the scores thus calculated onto each grid point. On the map, the underestimated, negative value areas were marked blue, while the overestimated, positive areas were marked orange. Areas where neither underestimation nor overestimation occurred were illustrated in white.

In the course of this analysis, we also performed studies for several precipitation thresholds, of which we presented the maps produced from the 85th and 95th percentiles belonging to the 15 mm threshold index. The results in *Fig. 8* unquestionably confirm the previously described result, that the 85th member of the ecPoint Rainfall provides the most accurate prediction, while the higher percentiles often overestimate the actual measured values. A significant part of the country was white on the map representing the 85th percentile, as opposed to the map displaying the 95th percentile that reflected absolute overestimation with orange dominating the map (*Fig. 9*).

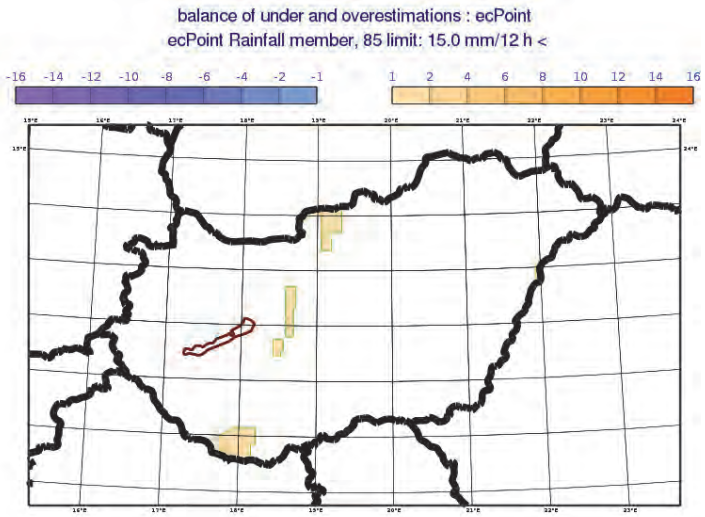

Fig. 8. Map produced from the 85th percentiles belonging to the 15 mm threshold index.

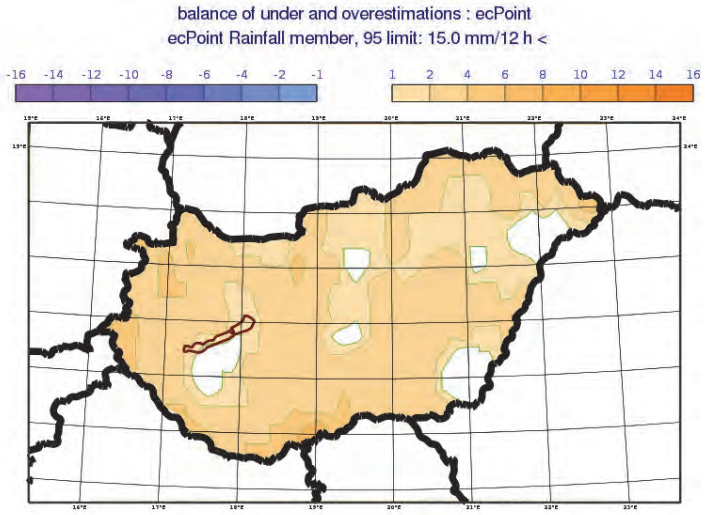

Fig. 9. Map produced from the 95th percentiles belonging to the 15 mm threshold index.

3.4. Case study

Finally, after the verification results, we would like to highlight the main benefits of the ecPoint Rainfall product, which is the most effective in the predictions of summer, convective situations, with a case study. This is important, because the number of thunderstorms with extreme rainfall is increasing in Hungary. Orographic factors also contribute to the phenomena of flash flood formed by intense storms. Extreme precipitation may be one of the most dangerous causes of natural disasters. To avoid any damages, it is very important to make an accurate forecast as soon as possible enabling preparation and protection. The aim of the new method is to determine the chances of heavy rainfall, especially in critical regions, a few days in advance.

For a case study, we examined a flash flood event in Szilvásvárad, which occurred on June 10–11, 2018 (*Tóth*, 2020). On this day in Bánkút, which is the closest meteorological station to Szilvásvárad, 174 mm/24 hours precipitation was registered between 06 UTC, June 10, 2018 and 06 UTC, June 11, 2018 (*OMSZ*, 2018). The rainfall seemed to be a completely local problem in the Bükk area, because a few km away from Szilvásvárad, only 4 mm/24 hours precipitation was measured in Eger (*OMSZ*, 2018).

Even experimental ecPoint Rainfall GRIB files, containing 12 hours precipitation amount were available with 6 hourly frequency for us, but due to archiving limitations, only 00–12 UTC and 12–00 UTC GRIB files were archived in OMSZ. Currently, ecPoint Rainfall GRIB files are not available from ECMWF's MARS archive. ECMWF plans to provide 6 hours and 24 hours ecPoint Rainfall post-processed products in the future, but during our study, the 24 hours post-processed products could not be used for the usual synoptical period, covering from 06 UTC to 06 UTC interval.

In our study, we concentrated on the investigation of the capability of the ecPoint Rainfall products, so we made a 24 hours observed precipitation chart covering from 12 UTC to 12 UTC based on the high density precipitation observation network of the OMSZ. Even in this case we have definitely less observations, approximately 310 stations than the standard 06–06 UTC synoptical period, but we can easily see the geographical density of the observation network used for validation. In addition to above mention reasons, as major part of intensive precipitation occurred in the second part of June 10, 2018 and first part of June 11, 2018 we made a map containing 24 hours precipitation covering this interval (*Fig. 10*). This map shows that the highest value, 92 mm/24 hours was measured in Bükkszentlélek and 18 mm/24 hours was measured in Eger.

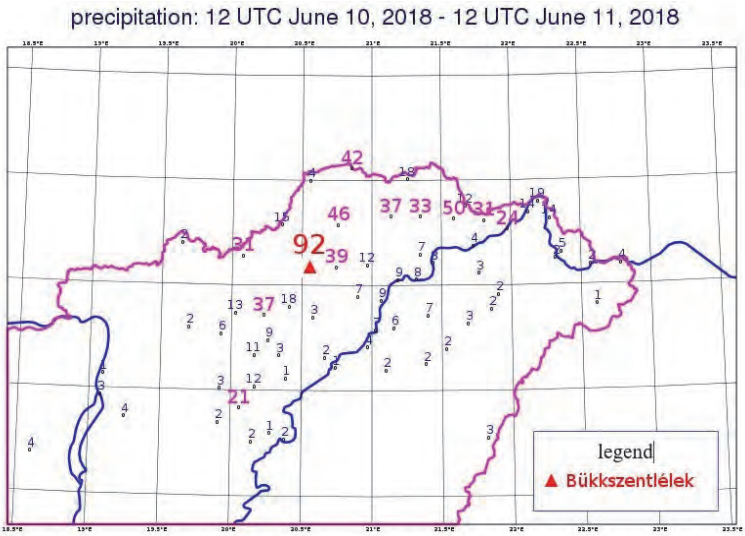

Fig. 10. Observed 24 hours precipitation between 12 UTC, 10 June, 2018 and 12 UTC, June 11, 2018.

In the north and southwest parts of Europe cyclones shaped the weather, while Central Europe was located in the warm sector. Over the Iberian and Balkan peninsulas, the high-altitude cold vortex emerged in those days had unstabilized the atmosphere, thus showers and thunderstorms interrupted the sunlight in many places. In Hungary, the formation of unstable atmospheric conditions was due to the shallow cyclone in southeast Europe, which gradually marched over the country. As a result, there was a strong cumulus cloud formation in the Northern Central Mountains in the afternoon, to which the lifting effect of the mountains significantly contributed. Due to the slow flow system, the rapidly developing thunderstorm cells did not move from the area for hours, which led to the accumulation of extreme rainfall.

The most intensive precipitation zone was reported from the Bükk area, where a total of 174 mm/24 hours of precipitation was measured. Such a large amount of precipitation is most characteristic of the monsoon regions, so it occurs rarely in Hungary, approximately every 10–20 years. It is no accident that predicting these types of local, extreme amounts of precipitation zones is one of the biggest challenges for meteorologists, even with fine resolution of models. To alleviate this problem, ECMWF has developed the ecPoint Rainfall product, which has already estimated the rainstorm in June 2018 more accurately.

Figs. 11 and *12* display probability maps of ecPoint Rainfall in percentages: the accumulation of 10 mm/12 hours (*Fig. 11*) or more precipitation on one map and the accumulation of 30 mm / 12 hours (*Fig. 12*) or

more precipitation on the other. The forecasts were made on June 8 at 00 UTC for a period between +72 and +84 hours and on June 10 at 00 UTC for a period between +24 and +36 hours. Based on these maps, the expectation of higher rainfall in the Bükk is quite obvious. While precipitation was probable with different probability values in all of the north and northeast parts of Hungary on the map that uses the 10 mm threshold index, on the map of 30 mm threshold index the local precipitation zone is nicely outlined. Although these maps predict the expected extreme and local precipitations with relatively low possibility, this information is very important for forecasters mainly because of the convective season in the hilly regions.

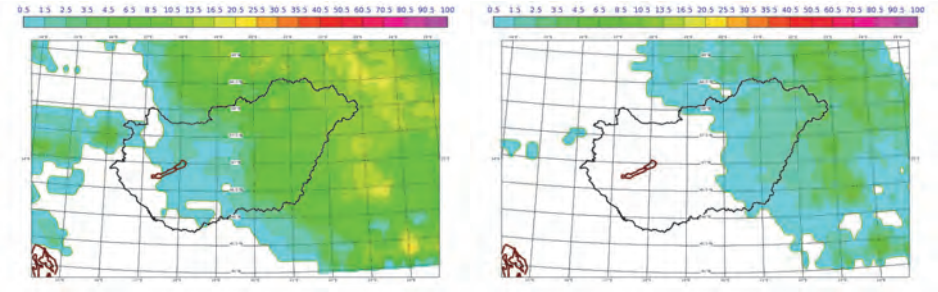

Fig. 11. Probability of precipitation exceeding 10 mm/12hours (left) and 20 mm/12 hours (right). EcPoint Rainfall forecasts were made on June 8 at 00 UTC for a period between +72 and 84 hours.

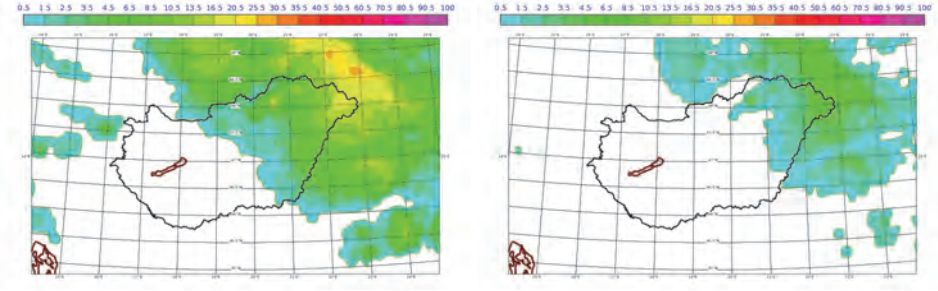

Fig. 12. Probability of precipitation exceeding 10 mm/12h (left) and 20 mm/12 hours (right). EcPoint Rainfall forecasts were made on June 10, at 00 UTC for a period between +24 and 36 hours.

It is necessary to highlight that the new product was not available to the forecasters by this flash flood event. If in the summer of 2018 ecPoint Rainfall had been available, the forecasters could have identified the endangered areas 3 or 4 days earlier.

A new ensemble meteogram of ecPoint Rainfall predictors was created (*Fig. 12*) in order the forecasters get a comprehensive view of the weather situations and that the new product can be used properly. If synoptic meteorologists look at the ensemble meteogram, they will immediately see how the predictors used in the production of ecPoint Rainfall behave. Using the ensemble meteogram, they can conclude which predictors are crucial for the forecast of the ecPoint Rainfall; moreover, it contributes to decision-making of forecasters.

Fig. 13 shows the ensemble meteogram for the case study in Szilvásvárad. The diagram was divided to 4 parts, which are 4 variables. At the top, there is the 12 hours precipitation forecast of the ecPoint Rainfall and the ensemble in mm. When the ecPoint Rainfall 12 hours values of that Sunday were summed, more than 70 mm precipitation was predicted, while the ensemble forecast expected much less. In the second part, there is a convective precipitation rate, which from Sunday afternoon gradually increased. Located under the convective precipitation rate is the 700 hPa wind speed in m/s. Due to slow flow, the previously formed storm cells stood in one place, which caused a significant amount of precipitation. At the bottom of the figure there is the CAPE index in J/kg, which has grown constantly in the investigated period, and at 18 UTC the CAPE index was about 1500–2000 J/kg. Analyzing the meteogram, an extreme precipitation event could be expected, because the high CAPE index associated with the orographic buoyancy further increased the probability of flash flood events. In conclusion, the new ecPoint Rainfall product is a promising innovation for forecasting these events in advance.

In the case of June 10, 2018, the main problem was the amount of water flowing down from the mountains. At dawn, Szilvásvárad was flooded with water, which caused huge damage to the persons and to the community as well. The new product developed by the ECMWF may prove to be a consequential tool for the early detection of such natural disasters, which is completely supported by this study.

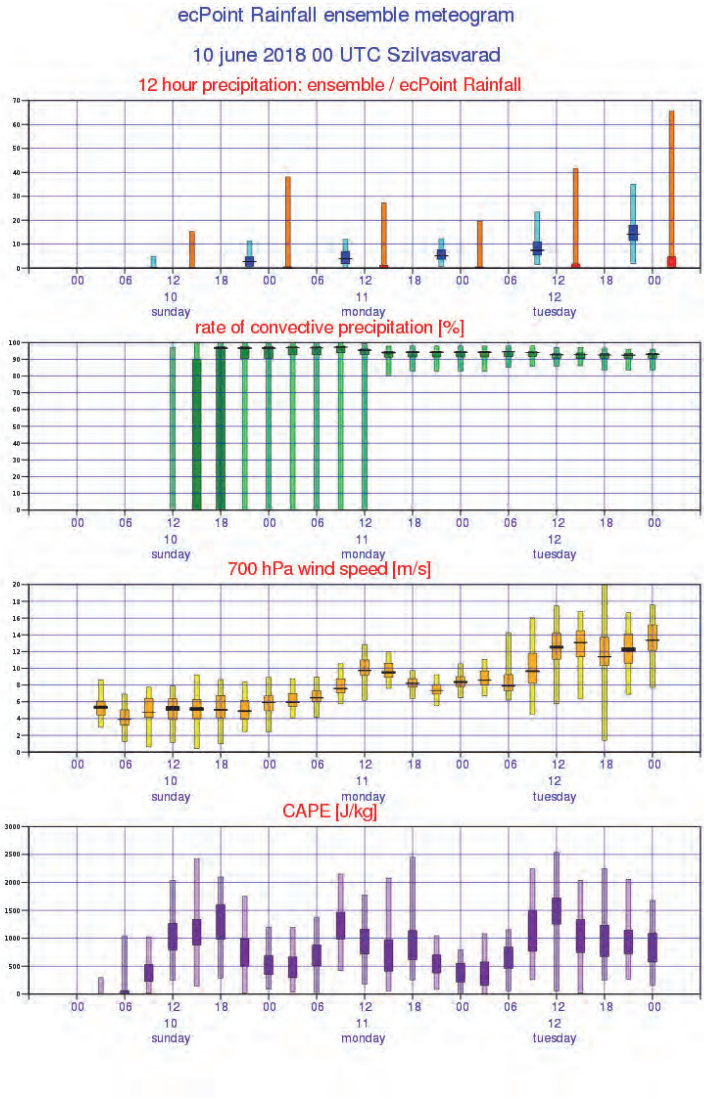

Fig. 13. Ensemble meteogram based on predictors of ecPoint Rainfall.

4. Conclusion

Accurate forecast of ecPoint of the precipitation amount is quite challenging even for modern numerical weather forecasting models. In our work, a comprehensive validation of a new innovative post-processing tool, the ECMWF's ecPoint Rainfall products was aimed. EcPoint Rainfall products can successfully provide information about the probability of subgrid scale precipitation, so extreme events, including flash floods can be warned in time.

During our work, the capability of this method was studied by different verification methods, approximately 75 cases were selected from a very intensive convective period covering the summer of 2018. As a result of this work, ecPoint Rainfall products operationally support decision makers in the warning of the extreme precipitation events at OMSZ.

References

Bodolainé, J.E., 1983: Árhullámok szinoptikai feltételei a Duna és a Tisza vízgyűjtő területén. *OMSZ Hivatalos Kiadványai 56*, Budapest. (in Hungarian)

Bonta, I. and *Újváry K.*, 2011: Hidrológiai célú mennyiségi csapadékelőrejelzés hazánkban. *Magyar Tudomány 172*, 1449–1458. (in Hungarian)

Bölöni, G., Kullmann, L., and *Horányi, A.*, 2009: Use of ECMWF lateral boundary conditions and surface assimilation for operational ALADIN model in Hungary. *ECMWF Newsletter 119*, 29–35.

Forbes, R., Tsonevsky, I., Hewson, T., and *Leutbecher, M.*, 2014: Towards predicting high-impact freezing rain events. *ECMWF Newsletter 141*, 15–21.

Gascon, E., Hewson, T., and *Sahin, C., 2018:* New meteogram and map ecCharts products for precipitation type probabilities. *ECMWF Newsletter 154*, 2–3.

Hewson, T., Pillosu, F., Bonet, A., Russell, I., Sahin, C., and *Pappenberger, F.*, 2019: New point rainfall products in ecCharts. *ECMWF Newsletter 159*, 9.

Hewson, T. and *Pillosu, F.*, 2021: A new low-cost technique improves weather forecasts across the world. *Nature*, Preprint at https://arxiv.org/abs/2003.14397

T. Hewson, T, and Pillosu, F. , 2021 : A new low-cost technique improves weather forecasts across the world. *Commun. Earth Environ. 2*, 132. https://www.nature.com/articles/s43247-021-00185-9

|*Horányi, A., Ihász, I.*, and *Radnóti, G.*, 1996: ARPEGE/ALADIN: A numerical weather prediction model for Central-Europe with the participation of the Hungarian Meteorologi.cal Service. *Időjárás 100*, 277–300.

Horányi, A., Kertész, S., Kullmann, L, and *Radnóti, G.*, 2006: The ARPEGE/ALADIN mesoscale numerical modelling system and its application at the Hungarian Meteorological Service., *Időjárás 110*, 203–227.

Horányi, A., Mile, M., and *Szűcs, M.*, 2011: Latest developments around the ALADIN operational short-range ensemble prediction system in Hungary. T*ellus 63A*, 642–651.

Ihász, I., 1992: Hogyan működik az első operatív hazai numerikus előrejelző modell? Légkör *37, 12–36.* (in Hungarian)

Ihász, I., 2004: Experiments of clustering for central European area especially in extreme weather situations. Proceedings of the Ninth ECMWF Workshop on Meteorological Operational Systems, Reading UK, 10-14 November 2003, 112–116.

Ihász. I., Üveges, Z., Mile, M., and *Németh, Cs.*, 2010: Ensemble calibration of ECMWF's medium-range forecasts. *Időjárás 114*, 275–286.

Ihász, I. and *Tajti, D.*, 2011: Use of ECMWF's ensemble vertical profiles at the Hungarian Meteorological Service. ECMWF Newsletter, *129*, 20–24.

Ihász, I., 2014: Az operatív numerikus modellezés kezdeti évei Magyarországon: A svéd modell alkalmazása. In (eds. *Horányi, A.* and *Szépszó, G.*) Dévényi Dezső emlékkötet. *63-69.* (in Hungarian)

Ihász. I., Mátrai, A., Szintai, B., Szűcs, M., and *Bonta, I.*, 2018: Application of European numerical weather prediction models for hydrological purposes. *Időjárás 122*, 59–79. DOI:10.28974/idojaras.2018.1.5.

Ihász, I. and *Modigliani, U.*, 2019: 25 years of the cooperation between the Hungarian Meteorological Service and ECMWF. *ECMWF Newsletter, 160*, 9–10.

Kaba, M., 1995: Csatlakozásunk a Középtávú Időjárási Előrejelzések Európai Központjához. *Légkör 40*, 34. (in Hungarian)

Mátrai, A. and *Ihász, I.*, 2017: Calibrating forecasts of heavy precipitation in river catchments. *ECMWF Newsletter 152*, 32–35.

Mile, M., Bölöni, G., Randriamampianina, R., Steib, R., and Kucukkaraca, E., 2015: Overview of mesoscale data assimilation developments at the Hungarian Meteorological Service. *Időjárás 119*, 213–237.

OMSZ, 2018: Mint a monszun – új napi csapadékrekord a Bükkben (VI. 10.). (in Hungarian) https://www.met.hu/omsz/OMSZ_hirek/index.php?id=2576&m=2 (last access: 8 December 2020)

Owens, R.G. and *Hewson, T.D.*, 2018: ECMWF Forecast User Guide. Reading. ECMWF. doi: 10.21957/m1cs7h.

Pillosu, F. and *Hewson, T.*, 2017: New point-rainfall forecasts for flash flood prediction. *ECMWF Newsletter 153*, 2–3.

Szintai, B., Szűcs, M., Randriamampianina, R., and *Kullmann, L.*, 2015: Application of the AROME non-hydrostatic model at the Hungarian Meteorological Service: physical parameterizations and ensemble forecasting. *Időjárás 119*, 241–265.

Szűcs, M., Sepsi, P., and *Simon, A.*: 2016: Hungary's use of ECMWF ensemble boundary conditions. *ECMWF Newsletter 148, 24–31*.

Tóth, B., 2020: Kistérségű extrém csapadékmennyiség valószínűségének becslése ECMWF ensemble előrejelzések alapján. Master Thesis, Budapest. (in Hungarian)

Woods, A., 2005: Medium-Range Weather Prediction – The European Approach. *Springer*, 270 p.

DOI:10.28974/idojaras.2021.3.3

IDŐJÁRÁS

Quarterly Journal of the Hungarian Meteorological Service
Vol. 125, No. 3, July – September, 2021, pp. 419–430

Evapotranspiration estimation at the Kis-Balaton wetland

Angela Anda*, **László Menyhárt**, and **Brigitta Simon**

Hungarian University of Agriculture and Life Sciences, Georgikon Campus of Keszthely
Corresponding author's e-mail:*

**Corresponding author E-mail: anda.angela@uni-mate.hu*

(Manuscript received in final form March 31, 2020)

Abstract— Evapotranspiration rate, ET_a and vegetation composition strongly influence the water budget of wetland impacting available water and water resource management. One of the goals of this study was to estimate the areal ET_a of the Kis-Balaton wetland, KBW (natural ecosystem) between 1997 and 2012. This time period was free of any human intervention. ET_a was accounted for different vegetation classes through the multiplication of the reference evapotranspiration, ET_0 by previously determined crop coefficients in each vegetation/open water classes. Besides common reed and cattail, five other groups were separated, including open water as an independent class. The evapotranspiration sums were strongly impacted by annual mean air temperature, T_a. One degree increment in annual average T_a will increase the yearly ET_a sums in about 100 mm. The yearly areal ET_a of KBW ranged from 737.08 mm to 896.63 mm with an average of 802.07 mm during the 16-year study.

1. Introduction

Crops, including wetlands, under the impact of solar radiation are influenced by such variables as temperature, water transport processes, crop growth, and production (*Burba et al.*, 1999). Partitioning of radiation and actual evapotranspiration, ET_a are strongly associated with the stage of vegetation.

Among others, *Abtew* and *Obeysekera* (1995) and *Allen et al.* (1998) discussed the methodology available for wetland's ET_a estimations. These wetland's areal ET_a approximations are similar to those of used in ET_a calculations of arable crops. Two options include direct measurements (lysimeter use, energy balance Bowen ratio, and/or eddy covariance techniques) and modeling approach.

The main limitations of direct measurements are the high cost of lysimeter maintenance and difficulties in their operation for other crops than wetlands (*Valiantzas*, 2006; *Zhou* and *Zhou*, 2009). This method also requires an expert laboratory (*Allen et al.*, 2011; *Wang* and *Dickinson*, 2012). In everyday practice, to get ET_a, crop coefficients, K_c are multiplied by reference evapotranspiration, ET_0. Limited generalizability of K_c exists from plant side, as types and distribution of crops differ greatly from place to place (*Drexler et al*., 2004). Parallel with this assumption, different kinds of microclimatological models use a large number of hardly accessible inputs (meteorological and canopy surface data).

Anthropogenic interventions have modified the water level of Lake Balaton during the past two centuries. Two hundred years before, the establishment of the sluice of Sió canal and the extension of agricultural land declined the lake's water level drastically, causing serious water quality issues, mainly in the Keszthely-bay. To mitigate water quality deterioration, a new reconstruction project, the so-called Kis-Balaton Water Protection System (KBWS) was started at the end of the last century. Previously, severe cyanobacterial blooms deteriorated the water quality of the lake, that was published by *Tátrai et al*., (2000). Two steps (I and II) were launched as the reconstruction of the Kis-Balaton wetland (KBW). The first step was completed in 1985, while an eutrophic pond (Hídvégi pond) was created by five-step flooding (*Korponai et al*., 2010). The Hídvégi pond retained the nutrient loads causing overall improvement of the Balaton's water quality (*Hatvani et al.*, 2011). Phase II (Fenéki pond) operated the water level management of the wetland ecosystem synchronizing different habitats to avoid different conflicts. Reconstruction of KBWS was finished in 2016; an area is partly flooded, while other regions remained "untouched" habitats.

The geographical location of the study site, the Carpathian Basin which comprises Lake Balaton and the surrounding extended marshland, makes this region extremely vulnerable. Temperate zone formed in the basin has highly variable inter- and intra-annual precipitation and ET_a. This region is expected to have severe episodic droughts and floods, creating significant hydrologic lesions in response to human climate modification. In addition to weather variability, the on-site wetland ecosystems have little seasonal variability in green leaf area despite large seasonal variation in ET_a. A similar tendency was observed by *Garbulsky et al*. (2008) and *Anderson et al*. (2012) for Mediterranean wetlands. Due to these combined environmental specialties of temperate zone wetlands, attention was paid to improve the understanding of their ET_a peculiarities and their relevant controlling factors (weather variables and crop features). Wetlands differ in their energy regimes and exchange processes due to extent, fluctuating water levels, vegetation types, and geographical positions (*Kellner*, 2001). Therefore, on-site determined ET_a on daily timescale seems to be not appropriate to answer the many-sided questions relating to wetland's ET_a (*Admiral et al*., 2006). One part of the study was dedicated to these local ET_a concerns on such a natural ecosystem as KBW. The reason for studying the selected period (1997–2012) was

the uninterrupted phase in the life of the KBW. There was no human intervention during this time; the ecosystem could be treated as a natural one. This phenomenon is not common in the history of KBW from the end of the 19th century.

2. Materials and methods

A 16-year-long areal evapotranspiration study was conducted at the KBW, and the Agrometeorological Research Station (ARS) of Keszthely (latitude: 46° 44′ N, longitude: 17° 14′ E, elevation: 124 m above sea level), Hungary. This meteorological station belongs to the observational network of the Hungarian Meteorological Service. A QLC-50 climate station (Vaisala, Helsinki, Finland) with a pyranometer (Kipp & Zonen Corp., Delft, the Netherlands) is operational at the ARS. Combined air temperature, T_a and humidity sensors are placed at a standard height of 2 m above the surface level. Signals from meteorological sensors are collected every 2 seconds, and 10-min averages are logged. Data of the station were used in both ecosystem parts, including soybean.

K_c of dominant macrophytes of KBW were measured previously (2005–2011) in the growing chambers of Thornthwaite-Mather type compensation evapotranspirometers with unlimited water supply. The surface area of growing chambers was 4 m^2, with a depth of 1 m. These containers were settled at the meteorological station located on the northern edge of the KBW. Daily water losses were expressed as a residual member of the water budget equation. Later on, based on these measured evapotranspirations, the K_c of different macrophytes was expressed. More details on this experiment were published in *Anda et al*. (2014). (The same instruments were used in the determination of soybean ET_a between 2017 and 2018; see also Section 2.1).

Wetland maps of the KBW were produced by the Central- and West-Transdanubian Water Directorate. To produce digital orthophotos, triangulation was used to get the absolute orientation elements of the aerial photographs. A high resolution digital elevation model (DEM) transformed the original images into orthogonally projected images (*Winkler*, 2004) with a final pixel size of 0.5 m. The long-term data were analyzed by a pixel-based approach in the Environment for Visualizing Images, ENVI version 4.7 software package (ITT, 2009). The used classification method was the maximum likelihood to get the main classes of the sample area (Fenéki pond). Training areas for the classification were selected from field observations. To draw the vegetation map, ArcMap version 9.3.1 software (ESRI User Manual 2009, CA, US) was applied. See more details in *Anda et al*. (2014).

The ET_a of Fenéki pond was estimated by multiplying the ET_o with the K_c of the related macrophyte class and by accounting the cover ratio of that class as follows:

$$ET_a = \frac{\sum_{i=1}^{6}(ET_0 K_{cai} A_i)}{\sum_{i=1}^{6} A_i}, \quad (1)$$

where A is the area covered by the macrophyte and open water classes (1-6).

2.1. Statistics

The distribution of each ET_a series was checked by the Shapiro-Wilks test for normality. Square root transformation was performed to satisfy the assumption of normality. Long-term annual ET_a totals with a normal distribution (mm year^{-1}) were analyzed by a two-tailed t-test. All tests were carried out with SPSS Statistics version 17.0 software (IBM Corp., New York, USA).

3. Results and discussion

3.1. Composition of KBW

Based on the maps (ortophotograps) of the Hungarian Water Authority, the composition of the wetland was established between 1997 and 2012 (*Fig. 1*). Six classes were distinguished containing one open water and five macrophytes (*Crundell*, 1986) as follows:

Class 1. **Tall emergent macrophytes:** weed and two cattail species. As there was no significant difference in ET_a (including C_k) between the reed and cattail, they were put together in the same category.

Class 2. **Leafy emergent macrophytes:** Three species of sedge included in the second class of macrophytes.

Class 3. **Woody shrub:** willow.

Class 4. **Grassland:** fescue, French ryegrass, foxtail.

Class 5. **Woody deciduous:** alder, cottonwood.

Class 6. **Open water:** incorporating seaweed.

The ratio and composition of the classes with their spatial ranges are presented in *Table 1*.

Due to the presence of seaweed in the water of Kis-Balaton, to derive the accurate evaporation, the Class A pan evaporation was modified, filling the pans with seaweed and littoral sediments (*Anda et al*., 2018). About 15–20% increase in the "filled" pan evaporation was measured due to the above intervention.

The first two categories dominated the wetland canopy (40%+30%=70%). Outside of these two dominant classes, there was only one (Class 5), in which the cover ratio of a given class exceeded 10%. The cover percentage of all other groups fell well below 10%.

Table 1. Composition of KBW using vegetation and open water classes in the period of 1997–2012

Classes	**Type of habitat**	**Typical species (Latin names)**	**Common names**	**Cover**		
				Mean %	**Min %**	**Max %**
Class 1	Tall emergent macrophytes	*Phragmites australis, Typha angustifolia, Typha latifolia*	reed cattail	40	39	42
Class 2	Leafy emergent macrophytes	*Carex acutiformis, Carexe lata, Carex riparia*	sedge	30	27	33
Class 3	Woody shrub	*Salix cinerea, Salix alba*	willow	5	4	6
Class 4	Grassland	*Festuca rupicola, Arrhenatherum elatior, Alopecurus pratensis*	fescue French ryegrass foxtail	8	6	9
Class 5	Woody deciduous	*Salix fragilis, Alnus glutinosa, Populus tremula*	willow alder cottonwood	11	10	11
Class 6	Open water (with submerged crops)	*Ceratophyllum demersum, Ceratophyllum submersum, Najas marina*	seaweed	6	6	7

Fig. 1. Composition of macrophyte and open water classes in the KBW (*Anda et al*., 2015). (class 1: tall emergent macrophytes; class 2: leafy emergent macrophytes; class 3: woody shrub; class 4: grassland; class 5: woody deciduous; class 6: open water ± seaweed)

3.2. ET_a of the wetland with T_a

On the basis of daily on-site measurements in evapotranspirometer/A pan and calculated ET_0 (*Allen et al.*, 1998), their ratios, the C_k/pan coefficients were derived for class 1, class 2, and class 4 from 2005 to 2011. In the remaining two vegetation classes (class 3, class 5) data of *Irmak et al*. (2013) were adopted. The actual ET_a equals to the multiplication of ET_0 by C_k. A detailed description of the process and C_k results were published in *Anda et al*. (2014).

Long-term daily mean ET_a of six wetland classes with different covers ranged from 2.87 (class 5) to 4.04 (class 1) mm day^{-1}, with the maximum of 4.45 mm day^{-1} (class 1) in 2012 and minimum of 2.62 mm day^{-1} (class 5) in 2005 (*Table 2*). The highest ET_a was always observed in reed canopy (class 1) and not in open water. Open water evaporation can also limited by the temperature profile over the water surface. When the water surface is colder than the surrounding air, and there is only weak wind, a cold cap can limit the evaporation processes, since in the cold

air, the atmospheric humidity is higher. Although the derived l6-year daily mean ET_a of Fenéki pond (3.63 mm day^{-1}) was closer to the open water evaporation (3.66 mm day^{-1}) than that of the ET_a of classes with different crop covers. It is worth to remark that the cover of open water in KBW ranges between 6 and 7% only. The lowest daily mean ET_a was always observed in woody deciduous class, while the highest ones were in the two dominant macrophyte classes (class 1 and class 2). These two latter categories' results were comparable with that of 4.4 mm day^{-1} revealed by *Lenters et al.* (2011) for reed and cattail dominated wetland in Nebraska, USA, for almost the same environmental conditions as at the KBW. Similar daily mean ET_a results of 4.3 mm day^{-1} were obtained by *Irmak et al*. (2013) for a riparian plant community for Nebraska, for the same growing site as the previous citation of *Lenters et al.* (2011) mentions.

Table 2. Daily mean evapotranspiration (mm/day) of six the wetland classes with different covers and areal evapotranspiration of the whole Fenéki pond between 1997 and 2012

Year	Class 1	Class 2	Class 3	Class 4	Class 1	Class 6	Fenéki pond
			[mm day^{-1}]				
1997	3.87	3.36	3.04	3.13	2.77	3.53	3.47
1998	3.76	3.25	2.97	3.05	2.68	3.42	3.38
1999	3.81	3.29	2.99	3.07	2.71	3.45	3.41
2000	4.36	3.77	3.42	3.53	3.09	3.96	3.92
2001	4.10	3.52	3.19	3.30	2.86	3.70	3.66
2002	4.22	3.61	3.24	3.37	2.98	3.77	3.77
2003	4.32	3.73	3.40	3.49	3.09	3.92	3.89
2004	3.75	3.27	3.01	3.06	2.69	3.44	3.39
2005	3.71	3.20	2.88	2.99	2.62	3.35	3.33
2006	3.83	3.29	2.98	3.07	2.71	3.44	3.43
2007	4.24	3.64	3.30	3.41	2.97	3.81	3.80
2008	4.05	3.51	3.19	3.28	2.88	3.68	3.65
2009	4.07	3.53	3.24	3.31	2.91	3.72	3.68
2010	3.75	3.21	2.92	3.01	2.64	3.36	3.36
2011	4.36	3.80	3.46	3.55	3.13	4.00	3.94
2012	4.45	3.86	3.54	3.61	3.20	4.05	4.02
Mean	**4.04**	**3.49**	**3.17**	**3.27**	**2.87**	**3.66**	**3.63**

During the observation period, the 16-year annual ET_a totals of different classes ranged from 745.98 (class 5) to 974.81 mm (class 1) with a weighted average of 896.63 mm for the Fenéki-pond. The most important statistical characteristics are presented in *Fig. 2*. According to the daily mean ET_a results of vegetation and open water classes, the highest yearly ET_a sums were observed in reed (cattail) followed by the open water, which result was very close to spatial ET_a sum of the whole Fenéki pond. In case of Fenéki-pond, the annual weighted mean ET_a of warm years increased with 11.45% ($p<0.001$) in comparison to cool year's ET_a water losses, suggesting that almost 100 mm difference in wetland's ET_a was manifested in favor of warm periods.

On the basis of the 16-year study, the largest water consumer in the Kis-Balaton was the reed and cattail (class 1), occupying almost half of the wetland area (*Fig. 3*). The second in line is the sedge (class 2), contributing at about a third of the total water use. Annual mean water losses *(*ET_a or evaporation) of all the other vegetation/open water classes contributed less than 10%.

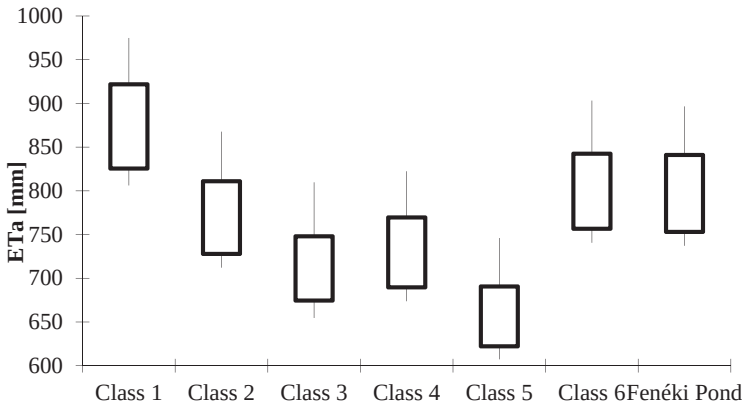

Fig. 2. Box-plot for the annual evapotranspiration totals, ET_a in different vegetation and open water classes between 1997 and 2012. The bottom and top of the boxes represent the 25th and 75th percentiles. The vertical lines that end in horizontal strokes above and below each box are from the upper and lower hinges to the upper and lower adjacent values.

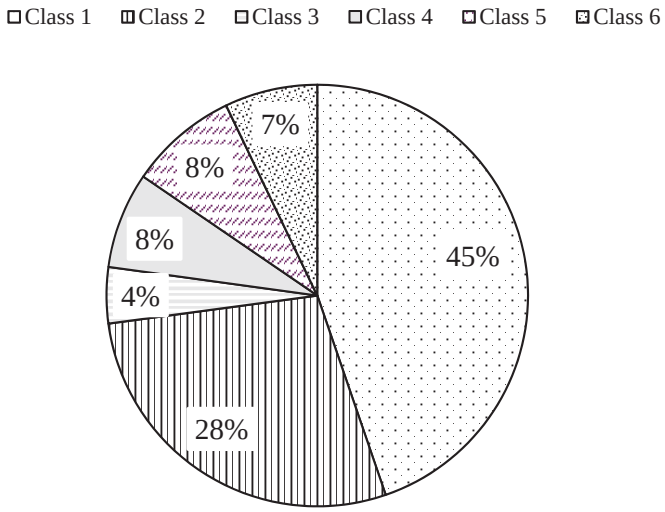

Fig. 3. Contribution of different vegetation/open water classes to the evapotranspiration of the Fenéki pond.

Yearly mean T_a of KBW was 10.8 °C between 1997 and 2012. The 1971 to 2000 climate norm of 10.3 °C was half-degree lower than that of the annual mean T_a during the investigation period. Out of sixteen years studied, seven cool (T_a<10.8 °C: 1997, 1998, 1999, 2004, 2005, 2005, 2010) and nine warm years (T_a>10.8 °C: 2000, 2001, 2002, 2003, 2007, 2008, 2009, 2011, 2012) were distinguished, which might be decisive for the wetland's ET_a. The difference in annual average T_a between cool (10.1 °C) and warm years (11.3 °C) equalled to 1.2 °C ($p<0.001$). It is worth to notice that all warm years were registered after 2000.

To evaluate the potential impact of annual mean T_a versus ET_a total, linear regression was fitted (*Fig. 4*). Based on the slope, 1 °C increment in annual T_a significantly increased the ET_a totals by 61.7 mm, with a relatively low RMSE of 23.9 mm/year. The scatter in the data was higher at cooler years.

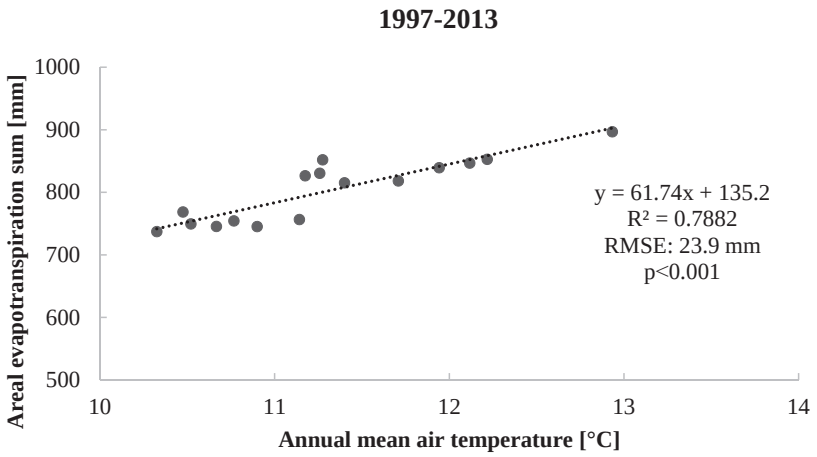

Fig. 4. Regression between annual mean air temperatures vs areal evapotranspiration totals at the KBW between 1997 and 2012.

4. Conclusions

In the KBW, the climatic norm (1971–2000) of annual precipitation sum is 634.2 mm with the wettest and driest monthly precipitation sums of 78.5 mm in July and 31.1 mm in January, respectively. Comparison between long-term annual ET_a sums and climate norm of precipitation confirmed only 70.7% of the ET_a entering by precipitation at the KBW. Other inputs are also needed to balance the water budget of the wetland. The governing terms of a wetland water balance are the ET_a and the precipitation (*Soja et al.*, 2013), making the system vulnerable to the negative impacts of the climatic change through variable rainfall events. Monitoring these governor factors would help for water authorities to mitigate issues related to the water level of KBW and Lake Balaton that are embedding on the system due to upcoming climate change.

Acknowledgements: The publication is supported by the EFOP-3.6.3-VEKOP-16-2017-00008 project. The project is co-financed by the European Union and the European Social Fund.

References

Abtew, W. and *Obeysekera, J.*, 1995: Lysimeter study of evapotranspiration of cattails and comparison of three estimation methods. *Trans. ASAE 38*, 121–129. https://doi.org/10.13031/2013.27820

Admiral, S.W., Lafleur, P.M., and *Roulet, N.T.*, 2006: Controls on latent heat flux and energy partitioning at a peat bog in eastern Canada. *Agric. Forest Meteor. 140*,308–321. https://doi.org/10.1016/j.agrformet.2006.03.017

Allen, R. G., L. S. Pereira, T. A. Howell, Jensen, M. E., 2011: Evapotranspiration information reporting: I. Factors governing measurement accuracy. *Agric. Water Manage. 98*, 899–920. https://doi.org/10.1016/j.agwat.2010.12.015

Allen, R.G., Pereira, L.S., Raes, D., and *Smith, M.*, 1998: Crop Evapotranspiration: Guidelines for Computing Crop Requirements. FAO Irrigation and Drainage Paper 56 FAO, Rome, Italy.

Anda, A., Simon, B., Soós, G., Menyhárt, L., Teixeira da Silva, J. A., Kucserka, T., 2018: Extending Class A pan evaporation for a shallow lake to simulate the impact of littoral sediment and submerged macrophytes: a case study for Keszthely Bay (Lake Balaton, Hungary). Agric. Forest Meteorol. 250–251, 277–289. https://doi.org/10.1016/j.agrformet.2018.01.001

Anda, A., Soos, G., Teixeira da Silva, J.A., and *Kozma-Bognár, V.*, 2015: Regional evapotranspiration from a wetland in Central Europe, in a 16-year period without human intervention. A*gric. Forest Meteorol. 205*, 60–72. https://doi.org/10.1016/j.agrformet.2015.02.010

Anda A., Teixeira da Silva J.A., and *Soos, G.*, 2014: Evapotranspiration and crop coefficient of the common reed at the surroundings of Lake Balaton, Hungary. *Aquatic Bot. 116*, 53–59. https://doi.org/10.1016/j.aquabot.2014.01.008

Anderson, R.G., Yufang, J., and *Goulden, M.L.*, 2012: Assessing regional evapotranspiration and water balance across a Mediterranean montane climate gradient. *Agric. Forest Meteorol. 166–167*, 10–22. https://doi.org/10.1016/j.agrformet.2012.07.004

Burba, G.G., Verma, S.B., and *Kim, J.*, 1999: Surface energy fluxes of Phragmites australis in a prairie wetland. Agric. Forest Meteor. 94: 31–51. https://doi.org/10.1016/S0168-1923(99)00007-6

Crundell, M. E.. 1986: A Review of hydrophyte evapotranspiration. *Rev. Hydrobiol. Trop. 19*, 215–232.

Drexler, J.Z., Snyder. R,L,, Spano, D., and *Paw U, K.T.*, 2004: A review of models and meteorological methods used to estimate wetland evapotranspiration. *Hydrol. Proc. 18*, 2071–2101. https://doi.org/10.1002/hyp.1462

Garbulsky, M.F., Penuelas, J., Papale, D., and *Filella, I.* 2008. Remote estimation of carbon dioxide uptake by a Mediterranean forest. *Global Change Biol. 14*, 2860–2867. https://doi.org/10.1111/j.1365-2486.2008.01684.x

Hatvani, I.G., Kovács, J., Székely Kovács, I., Jakusch, P., and *Korponai, J.* 2011. Analysis of long-term water quality changes in the Kis-Balaton Water Protection System with time series-, cluster analysis and Wilks' lambda distribution. *Ecol. Engineer. 37*, 629–635. https://doi.org/10.1016/j.ecoleng.2010.12.028

Irmak S, Kabenge I, Rudnicka D, Knezevic S, Woodward D, and *Moravek, M*., 2013. Evapotranspiration crop coefficients for mixed riparian plant community and transpiration crop coefficients for common reed, cottonwood and peach-leaf willow in the Platte River Basin. Nebraska-USA. *J. Hydrol. 481*,177–190. https://doi.org/10.1016/j.jhydrol.2012.12.032

ITT, 2009: ENVI Program Package 2009. ITT corporation ENVI 4.7 software, 1133 Westchester Avenue, White Plains, NY 10604, USA.

Lenters, J.D., Cutrell, G.J., Istanbulluoglu, E., Scott, D.T., Herrman, K.S., Irmak, A., and *Eisenhauer, D.E.*, 2011: Seasonal energy and water balance of a Phragmites australis-dominated wetland in the Republican River basin of south-central Nebraska (USA). *J. Hydrol. 408*, 19–34. https://doi.org/10.1016/j.jhydrol.2011.07.010

Kellner, E., 2001: Surface energy fluxes and control of evapotranspiration from a Swedish Sphagnum mire. *Agric. Forest Meteorol. 110*:101–123. https://doi.org/10.1016/S0168-1923(01)00283-0

Korponai, J., Braun, M., Buczkó, K., Gyulai, I., Forró, L., Nedli, J., and *Papp, I.* 2010. Transition from shallow lake to a wetland: a multi-proxy case study in Zalavari Pond, Lake Balaton, Hungary. *Hydrobiologia 641*, 225–244. https://doi.org/10.1007/s10750-009-0087-0

Soja G., Züger J., Knoflacher M., Kinner, P., and *Soja, A.M.,* 2013. Climate impacts on water balance of a shallow steppe lake in eastern Austria (Lake Neusiedl). *J Hydrol. 480*,115–124. https://doi.org/10.1016/j.jhydrol.2012.12.013

T*átrai, I., Mátyás, K., Korponai, J., Paulovits, G.,* and *Pomogyi, P.,* 2000: The role of the Kis-Balaton Water Protection System in the control of water quality of Lake Balaton. *Ecol. Eng. 16,* 73–78. https://doi.org/10.1016/S0925-8574(00)00091-4

Valiantzas, J.D., 2006: Simplified versions for the Penman evaporation equation using routine weather data. *J. Hydrol. 331,* 690–702. https://doi.org/10.1016/j.jhydrol.2006.06.012

Zhou, L. and *Zhou, G.S.,* 2009: Measurement and modelling of evapotranspiration over a reed (Phragmites australis) marsh in Northeast China. *J. Hydrol. 372,* 41–47. https://doi.org/10.1016/j.jhydrol.2009.03.033

Wang, K. and *Dickinson, R.E.,* 2012. A review of global terrestrial evapotranspiration: Observation, modeling, climatology, and climatic variability, *Rev. Geophys., 50,* RG2005, doi:10.1029/2011RG000373. https://doi.org/10.1029/2011RG000373

WMO Report, 1975: Drought and Agriculture. WMO Techn. Note No. 138.

Winkler, P., 2004: The national orthophoto program of Hungary completed under strict quality control. The International Archives of the Photogrammetry, *Remote Sens. Spatial Inform. Sci. 34*. FÖMI, Budapest.

DOI:10.28974/idojaras.2021.3.4

IDŐJÁRÁS

Quarterly Journal of the Hungarian Meteorological Service
Vol. 125, No. 3, July – September, 2021, pp. 431–448

Analysis of heating and cooling periods in Budapest using station data

Csenge Dian[1,*], **Attila Talamon**[2], **Rita Pongrácz**[1], and **Judit Bartholy**[1]

[1]*Department of Meteorology*
Eötvös Loránd University
Pázmány Péter st. 1/A, H-1117, Budapest, Hungary

[2]*Institute of Architecture*
Óbuda University, Budapest, Hungary

**Corresponding author E-mail: diancsenge@staff.elte.*hu

(Manuscript received in final form July 27, 2020)

Abstract— The built environment has a very complex role in cities. On the one hand, various urban climatological phenomena are caused and influenced by buildings (e.g., urban heat island effect, local wind conditions, air pollution). On the other hand, buildings are important contributors to energy use via heating and cooling, e.g. they account for about 40% of total energy consumption on average in Europe. Daily average outdoor temperature is taken into account to design the heating and cooling systems of residential, commercial, or office buildings. That is why we analyzed the available temperature time series of the capital of Hungary, Budapest for the period between 1901 and 2019. The aims of this study are (i) to investigate the changes in temperature data series that influence building energy design parameters, (ii) to analyze the heating and cooling periods in the last 119 years based on different definitions, and (iii) to define a third (transitional) period between the heating and cooling periods. Based on the results, it can be concluded that the variability of warm days is smaller than that of cold days, consequently, the optimal design of heating systems is a greater challenge compared to cooling systems. Furthermore, the length of the temperature-based heating period decreased substantially, while the length of the cooling period increased as a consequence of overall regional warming.

Key-words: air temperature, heating system design parameter, heating and cooling period definitions, frequency distribution, regional warming, warm and cold extremes

1. Introduction

Nowadays, one of the most important global environmental problems is climate change. In addition to warming trends, other substantial changes can also be observed in the past few decades, for example, the increase of the frequency of extreme temperatures (*IPCC*, 2013, *Meehl* and *Tebaldi*, 2004). The changes draw a spatial pattern with different trends in different regions (*Seneviratne et al.*, 2006). Several studies have also been conducted for the Carpathian Basin. For instance, *Bartholy* and *Pongrácz* (2007) and *Pongrácz et al.* (2009) examined the effect of climate change on temperature and precipitation extremes using station data and regional climate model simulations. Furthermore, *Spinoni et al.* (2015) analyzed the increasing trends of heat waves and the decreasing trends of cold waves on the basis of gridded data. Climate change has an impact on the urban climate as well (*Masson et al.*, 2014, *Bokwa et al.*, 2018) in addition to several special effects due to artificial surfaces and built-up areas (e.g., the urban heat island effect, see *Oke*, 1973).

More than half of the world total population lives in cities, and the ratio is even greater in Europe (*United Nations*, 2015); therefore, it is necessary to analyze the climatological conditions affecting the urban areas. Buildings have fundamental roles in cities, because on the one hand, buildings are key factors in determining the urban climate, on the other hand, they substantially contribute to the energy use, e.g., they account for 40% of total energy consumption in the European Union (*Directive 2010/31/EU*, 2010). The energy consumption of buildings and the design parameters of energy systems depend on the outdoor air temperature. *Cho et al.* (2004) examined the relationship between energy consumption and temperature, and a regression model was built for a commercial building located in a South Korean city. Furthermore, *Roberts* (2008) investigated the impacts of climate change on buildings, and highlighted the effects of warming among the possible impacts. Further studies were carried out on the effects of urban heat island intensity and heat load on buildings and built-up areas, *Short et al.* (2004) focused on Great Britain, whereas *Bokwa et al.* (2019) studied five Central European cities (i.e., Bratislava, Brno, Krakow, Szeged, Vienna) taking into account the possible regional climatic changes. Since a specific temperature interval ideal for personal preferences has to be maintained inside buildings, neither too cold, nor too warm outdoor conditions are acceptable indoors, consequently, the energy demand of buildings highly depends on the outdoor temperature, from which the ideal conditions should be set. Too cold (warm) conditions can be specified by heating (cooling) demands, heating (cooling) degree-days, etc. Some studies aimed to analyze the heating and cooling degree-days, i.e., for Lithuania (*Martinaitis*, 1998) and Serbia (*Janković et al.*, 2019). *Kaynakli* (2008) determined the heating period for 14 years to optimize the insulation of buildings in Bursa, Turkey. According to the conclusions, the length of the heating periods was between 206 and 239 days

in the fourth most populated city located in northwestern Turkey, moreover, the maximum energy demand did not occur in the case of the longest heating period.

As it is mentioned above, the heating and cooling periods have an important role in building energy calculations, but their definitions are not uniform in different regions, they are based partly on actual temperature measurements and partly on calendar days. For example, Italy can be divided into the following six climatological zones, where heating systems start and end on different dates (*Bottio et al.*, 2014):

- Zone 1: from December1 to March 15,
- Zone 2: from December 1 to March 31,
- Zone 3: from November 15 to March 31,
- Zone 4: from November 1 to April 15,
- Zone 5: from October 15 to April 15,
- Zone 6: no heating is necessary throughout the year.

These zones represent the substantial extension of Italy from south to north. As we move towards the north, the overall climate becomes colder and the heating period becomes longer. Another example illustrates this climatic feature from Central Europe, namely, the official heating period lasts from September 1 to May 31 in Slovakia. More precisely, the heating must be started during this period, when the average daily temperature remains below 13 °C for two consecutive days (*Ministry of Economy*, 2005). Unlike these two countries, there is no official definition in Germany, however in practice, the heating period is between October 1 and April 30 (heating period definition in Germany).

The target area of our study is Budapest, the most populated city and capital of Hungary. Several studies have already evaluated the urban climatological conditions in Budapest, e.g., the extreme temperature values (*Göndöcs et al.*, 2018) or the urban heat island intensity using satellite data (*Pongrácz et al.*, 2010). In addition, the relationship between energy parameters and air temperature has also been analyzed for Hungary (*Talamon et al.*, 2016). The main aim of the present paper is to investigate the heating and cooling periods in Budapest, however, there are several definitions for the beginning and end of these periods, which will be compared. According to the current official regulations (*Government Decree* 157/2005. (VIII.15.)), the heating period is between September 15 of the actual year and May 15 of the following year. It is divided into three parts by the *FŐTÁV Zrt.* (2020): pre-heating period (between September 15 to October 14), heating period (between October 15 to April 15) and post-heating period (April 16 to May 15). In addition, there are unofficial definitions for the heating period, which fix the beginning and end of the period using different temperature threshold values. The part of the year outside the heating period is called the cooling period (*Talamon*, 2014).

We aim to address the following objectives: (1) to examine the extreme cold and extreme warm days, (2) to compare temperature-based and calendar-

based cooling and heating periods, (3) to define a third, transitional period, and to determine the average temperature and average length of the three periods, (4) to investigate the relationship between the climate change and the heating/cooling periods using the different definitions.

2. Data

In general, daily average temperature values are used for the building energy planning (e.g., *Matzarakis* and *Balafoutis*, 2004, *Christensen et al*., 2006, *Mourshed*, 2016, *Cheng and Li*, 2018), including the heating system design parameters. Because of its common use, we also used daily temperature data for Budapest. The station data series of five Hungarian cities are publicly available on the website of the Hungarian Meteorological Service for the period 1901–2019. The daily datasets include the following variables: mean temperature, maximum and minimum temperature, precipitation amount, precipitation type, sunshine duration. In this study we focus on Budapest, because this is the largest and most populated city of Hungary. The official measuring station of Budapest was relocated twice during the whole measuring period. The temperature measurements were performed near the Chain Bridge in the Buda side of the city, in Fő Street (47°30'3"N, 19°2'15"E) between January 1, 1901 and February 2, 1910. Then, the station was relocated to the instrumental garden near the Meteorological Institute in Kitaibel Pál Street (47°30'46"N, 19°1'34"E) and continued the measurements between March 1, 1910 and March 31, 1985. Since April 1, 1985, measurements have continued at Kitaibel Pál Street 1. On January 1, 1998, traditional thermometers were replaced with electric thermometers (https://www.met.hu/).

In order to evaluate the effect of instrument relocations and replacements, the mean temperature time series are compared to other databases. The entire study period can be covered using the Climate Research Unit Time-series (CRU TS) dataset. The CRU TS 4.03 version contains monthly average temperature values between 1901 and 2018 in high-resolution (0.5 degree) grids (*Harris et al.*, 2020, CRU dataset: http://www.cru.uea.ac.uk/). Moreover, the E-OBS v20.0e dataset (*Cornes et al*., 2018, E-OBS dataset: https://www.ecad.eu/) is available from January 1, 1950 to July 31, 2019, and CarpatClim is available between 1961 and 2010 (*Szalai et al*., 2013).

As a first step in the data evaluation, we selected the nearest grid points for the different geographical coordinates of the instrument from each database. As a second step, the root mean square error (RMSE) and the mean absolute error (MAE) were calculated for 3 years before and 3 years after each relocation and instrument replacement. *Table 1* shows the comparison with CRU TS dataset based on monthly data for the three above-mentioned dates occurring over the entire period. The largest difference in RMSE and MAE were observed at the

first relocation in 1910, the differences are about -0.65 °C and -0.75 °C, respectively. For the second instrument relocation (1985), the RMSE and MAE differences are also around 0.1 °C, while RMSE is less than 0.05 °C and MAE is around 0.07 in the case of the transition to a digital instrument (in 1998).

Table 1. Time series comparison with CRU TS dataset, RMSE and MAE values 3 years before and 3 years after the relocation and instrument change based on monthly data

		3 years before March 1, 1907 – February 28, 1910	**3 years after March 1, 1910 – February 28, 1913**	**difference between after and before values**
compared with CRU TS dataset	RMSE (°C)	2.230	1.580	-0.649
	MAE (°C)	2.208	1.456	-0.752

		3 years before April 1, 1982 – March 31,1985	**3 years after April 1, 1985 – March 31,1988**	**difference between after and before values**
compared with CRU TS dataset	RMSE (°C)	2.112	2.008	-0.104
	MAE (°C)	2.069	1.969	-0.100

		3 years before January 1, 1995 – December 31, 1997	**3 years after January 1, 1998 – December 31, 2000**	**difference between after and before values**
compared with CRU TS dataset	RMSE (°C)	1.978	1.932	-0.047
	MAE (°C)	1.943	1.876	-0.068

The comparison between E-OBS and CarpatClim daily mean temperatures is shown in *Table 2* for the second relocation in 1985 and the instrument change in 1998. In both cases, MAE values are lower than RMSE values. RMSE and MAE values with CarpatClim dataset are very similar to RMSE and MAE values with CRU TS dataset. In contrast, the comparison with E-OBS shows much lower values than when the comparison is done with CRU TS, thus the similarity between station data and E-OBS gridded data is greater.

In addition, the distributions of the values 3 years before and 3 years after the two relocations and replacement were compared using a χ^2 homogeneity test. In the case of the two relocations, the before and after distributions can be considered homogeneous at the significance level of 0.95, while distributions before and after the replacement are homogeneous at the significance level of 0.90.

On the basis of the comparison and the χ^2 homogeneity test we conclude that the suspected breakpoints of the temperature time series can be eliminated.

Thus, for building energy planning we can use the mean temperature time series of the Hungarian Meteorological Service.

Table 2. Time series comparison with E-OBS and CarpatClim datasets, RMSE and MAE values 3 years before and 3 years after the relocation and instrument change based on daily data

		3 years before April 1, 1982 – March 31, 1985	**3 years after April 1, 1985 – March 31, 1988**	**difference between after and before values**
compared with E-OBS dataset	RMSE (°C)	0.201	0.216	0.016
	MAE (°C)	0.151	0.168	0.017
compared with CarpatClim dataset	RMSE (°C)	1.903	1.899	-0.003
	MAE (°C)	1.719	1.670	-0.049

		3 years before January 1, 1995 – December 31, 1997	**3 years after January 1, 1998 – December 31, 2000**	**difference between after and before values**
compared with E-OBS dataset	RMSE (°C)	0.235	0.377	0.142
	MAE (°C)	0.177	0.285	0.109
compared with CarpatClim dataset	RMSE (°C)	1.787	1.810	0.023
	MAE (°C)	1.548	1.556	0.008

3. Methodology

3.1. Analyzing the extreme low and high temperatures

It is important to take into account the extremes of daily average temperature in building energy planning, because the extremes determine the entire range of temperature from where the optimal indoor temperature interval should be maintained. Buildings must be prepared for the cold extremes during the heating season and for the warm extremes during the cooling season. For the purpose of this analysis, the coldest and warmest days were selected from each year, namely, altogether 10% of the whole year, i.e., 18 days for cold extremes and 18 days for warm extremes.

First, the cold extremes are shown in *Fig. 1.* These selected yearly extremes are represented by decadal box-whiskers diagrams. Furthermore, a linear trend is fitted to the 119-year-long time series of the average temperature of the 18 coldest days of each year. These cold days form a quite wide interval within the

earlier decades of the entire period. The greatest difference between the minimum and maximum values is around 20 °C (in the 1920s and 1940s). Then, the whole range of the selected extremes decreased, the smallest range is only 10 °C in the 1990s, and it remained under 13 °C during the last two decades of the current analysis. This detected change stems from the lack of very extreme cold days with a mean temperature below -12 °C, whereas the higher cold extremes (i.e., the 5th percentiles) within the decades remained within the interval of freezing temperature, i.e., (-1 °C; 1 °C). Moreover, an overall warming trend of 1.9 °C/100 years can be clearly detected in Budapest based on the fitted linear trend to the yearly average temperature of the 18 cold days. This warming of the coldest days should certainly be taken into account when designing heating systems. It is clearly shown that lower values (even lower than -20 °C) occurred more frequently in the first half of the entire analyzed time period. In contrast, the median value of decades became higher since 1970, namely, more than half of the coldest 5% of the days of individual years were over -5 °C.

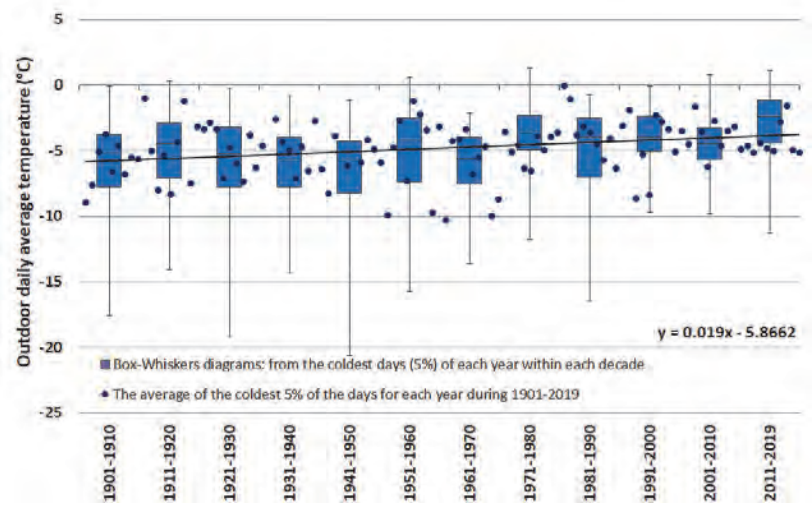

Fig. 1. The coldest 18 days of each year (5%) per decade on a box-whiskers diagram (with minimum, lower quartile, median, upper quartile, maximum) and the time series of the average of these 18 days per year (blue dots) with the fitted linear trend (the regression equation is also shown)

The same methodology was applied for the warmest 5% of days (*Fig. 2*). Temperature values of warm days form much narrower intervals than that of cold days. The greatest difference between maximum and minimum values is only 10 °C, which is the lowest difference in case of cold days. Moreover, the

observed warming trend is slightly greater in warm days (2.2 °C/100 years) than in cold days. The decadal temperature intervals of warm extremes do not exhibit the decreasing width that can be detected in the cold days. This coincides with the increase of the intensity and frequency of heat extremes and heat waves due to climate change (*Lakatos* and *Bihari*, 2011; *Göndöcs et al.*, 2018).

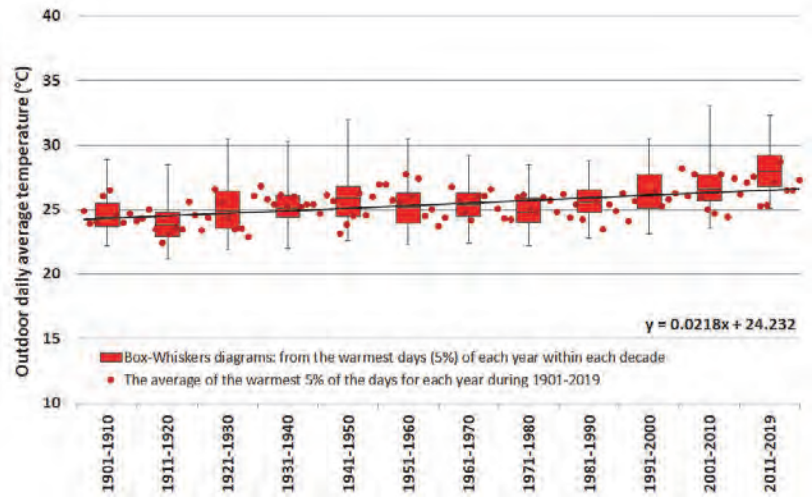

Fig. 2. The warmest 18 days of each year (5%) per decade on a box-whiskers diagram (with minimum, lower quartile, median, upper quartile, maximum) and the time series of the average of these 18 days per year (red dots) with the fitted linear trend (the regression equation is also shown)

3.2. Analysis of standard deviation and empirical density function of temperature time series

We evaluate the standard deviation and empirical density function of the 119-year-long time series in each decade as the second part of the analysis. Daily mean temperatures were ranked for each year from the coldest day to the warmest day. Then, the standard deviations for all the 365 ranked members were calculated for each decade. We selected two decades from the beginning (1901–1910, 1911–1920), middle (1951–1960, 1961–1970), and end (2001–2010, 2011–2019) of the study period, for which the results are shown in *Fig. 3* together with the average standard deviation for the whole 119-year period. This average standard deviation of extreme temperatures reaches 3 °C on the coldest days, whereas the standard deviation of the coldest days is 4 °C in the early 20th century. In general, the standard deviations of daily mean temperature during the

ranked cold days decrease fast and are close to the 119-year average, except during 2001–2010, when they are much lower (between 1 °C and 1.5 °C). Then, the standard deviations during the rest of the year (i.e., when it is not so cold, more specifically, above the 15th percentiles) are within the interval of 0.5–1.5 °C. An overall slight decrease can be detected in the standard deviation, however, it is not monotonous and contains local maxima during the individual decades. There is a smaller second maximum (exceeding 1 °C) in the standard deviations of the warmest days of most decades as well as in the 119-year average standard deviations. Consequently, on the one hand, it is difficult to design heating systems due to the large variance in the temperatures of cold days. On the other hand, the smaller standard deviation values of the warmest days cause less challenge for the design of cooling systems.

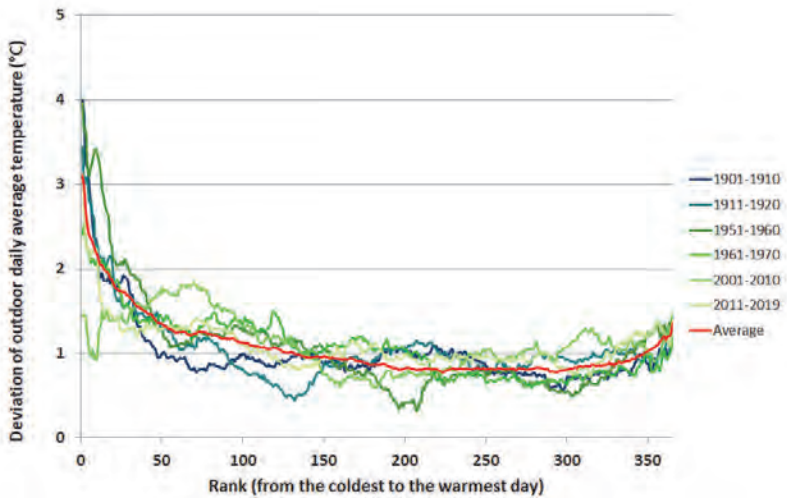

Fig. 3. The standard deviation of the sorted daily average temperatures from the coldest day to the warmest day for the beginning, middle, and end of the study period; in addition, the average of 119 years is also shown.

Finally, the empirical density functions of the selected decades and the total average of the 119 years are compared in *Fig. 4*. This calculation determines the average annual occurrence frequency of daily mean temperature from -10 °C to +35 °C using 1 °C resolution for the entire range. As the diagram shows, there are two peaks in the density functions, around 2–3 °C and around 20 °C. These two maximum locations occur because of considering the daily average

temperatures of the entire year. The colder maximum represents the winter half-year, whereas the warmer maximum of the empirical density function refers to the summer half-year. The asymmetry between the left and right tails is because of the fact that cold extremes show much higher variability than warm extremes (as it was already demonstrated in *Figs. 1–3*). The greatest variability between decades can be seen in the range of 0–22 °C. Moreover, in case of high temperatures, the frequency was clearly higher in the last two decades than at the beginning or the middle of the century. The warmest extremes after 2000 are about 2–4 °C higher than before. So, all these imply that temperature-related changes in summer appears to be more obvious and clearer than in winter, therefore, building energy planning is easier on the basis of warm days than cold days.

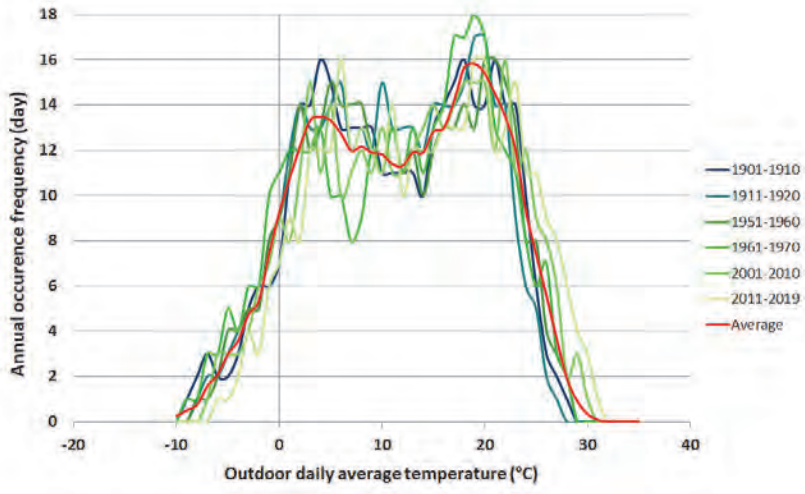

Fig. 4. The average annual occurrence frequency of the daily mean temperatures for the beginning, middle, and end of the study period; in addition, the average for the entire 119-year-long period is also shown.

4. Results and discussion

The previous section shows that cold and warm days changed to different degrees and with different variability over the past 119 years. Therefore, it is worth examining the cold and warm days separately. Our aim is to determine and analyze the heating and cooling periods based on the empirical density function presented in the previous section.

Three definitions were used to determine the heating and cooling periods:

1. TA (*Talamon*, 2014) definition:
   virtual heating and cooling periods are based on outdoor daily average temperature (lengths vary)
2. OA (October-April) definition:
   heating period is between October 15 and April 15 (length: 183 days),
   cooling period is between April 16 and October 14 (length: 182 days).
3. SM (September-May) definition:
   heating period is between September 15 and May 15 (length: 243 days),
   cooling period is between May 16 and September 14 (length: 122 days).

TA definition uses the properties of daily average temperature time series to determine the heating and cooling period (*Talamon*, 2014). As it was shown in Section 3 the standard deviation of cold days is much larger than the deviation of warm days. Furthermore, decadal density functions show clearer changes at higher temperatures. Therefore, we first determine the empirical density curve for the cooling season (i.e., summer) from the average density function of the 119 years. For this purpose, a partially symmetric density function is generated in the warm range using the temperature value of the highest frequency and the maximum temperature value. To obtain the empirical density curve of the virtual cooling period, the values of annual density function are reflected below its inflection point. Then, the virtual heating period is determined as the difference between the annual density function and the virtual cooling curve. In the OA and SM definitions heating and cooling periods were simply separated on the basis of calendar days. The density functions of the annual average and the heating and cooling periods for the three definitions are shown in *Fig. 5*. Because of the asymmetry in the annual average density function, the heating period covers a wider range of temperature values than the cooling period. Therefore, the occurrence frequencies of the cooling period are higher except for the SM definition (when the two parts of the year include substantially different number of days). The virtual heating and cooling curves based on the TA definition are very similar to the curves of the OA definition. The intersection of the heating and cooling curves coincides in the case of these two definitions around 11 °C. As a consequence of the SM definition, the heating period according to SM is clearly longer than the cooling period.

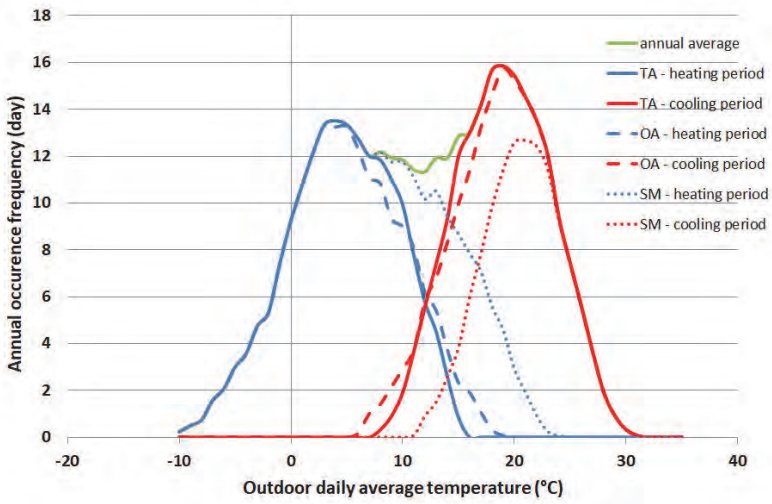

Fig. 5. The annual average empirical density function and the curves of heating and cooling periods for the average 119 years based on the three definitions.

As presented above, the whole year is divided into two parts from the aspects of building energy, namely, the heating and cooling period. However, the SM definition also includes a pre- and post-heating period representing the relatively fast inter-weekly temperature decrease and increase, respectively. Since the temperature of specific periods of the year changes from one year to the other, and also, an overall warming trend is identified due to global climate change (*Lakatos* and *Bihari*, 2011), a third period with higher inter-annual variability should be distinguished between the heating and cooling periods. For example, the autumn is becoming warmer (when cooling may be needed), while the typically winter low temperature values are extended to March or even April (with occasional heating demands). So instead of dividing the annual average density function into two parts, we separated the year into three different periods in the rest of the analysis. The common part of the heating and cooling curves is called the transitional period. Thereafter, the heating and cooling season does not include the transitional period. This procedure is applied to all the three definitions. *Fig. 6* shows the relationship between the average temperature of a period and the number of days within each period for the three definitions. According to the SM definition, more than half of the year belongs to the heating period (~ 200 days), while the cooling and the transitional periods last about the same number of days (~ 80 days each). When using this definition, the average temperatures are higher than in the other definitions, by 5 °C in the

transitional period, and by 2 °C both in heating and cooling periods. The average temperatures of the different periods using the TA and OA definitions are similar, around 3-3.5 °C in the heating period, 20 °C in the cooling period, and 12 °C in the transitional period. The transitional period is longer when using the TA definition than the OA definition. The comparison also shows that the TA definition, which is based on temperature, results in similar values overall to the OA definition (which is the most often used definition in Hungary), but it is more flexible and can reflect climate changes better.

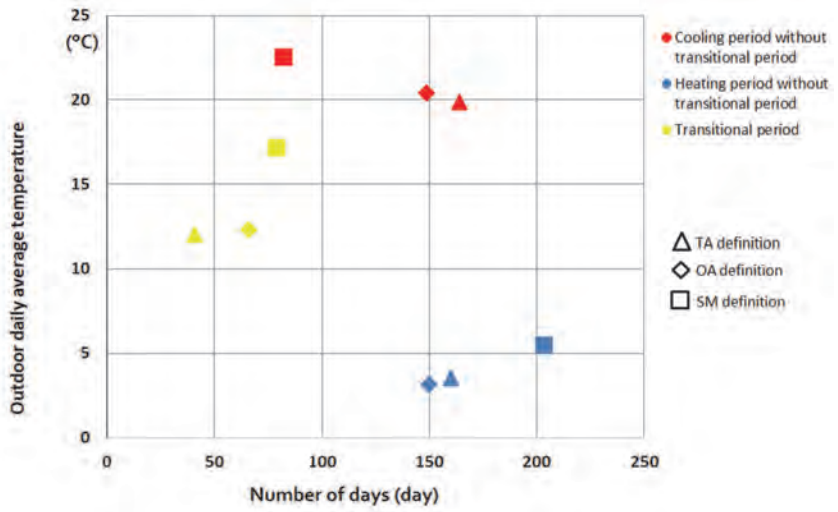

Fig. 6. The average temperature and the number of days in the heating, cooling, and transitional periods based on the TA, OA, and SM definitions.

After comparing the different definitions, *Fig. 7* shows the average temperature and the length of three periods using the OA and TA definitions (*Fig. 7*) for the previously selected six decades. When using the OA definition (*Fig. 7a*), the difference between the early 20th century and the early 21st century is about 2 °C in each period. Moreover, the length of the cooling and heating period decreased in the last two decades, while the yearly average total number of days in the transitional period increased. In contrast, when using the TA definition (*Fig. 7b*), which is based on outdoor daily average temperature, the cooling period was more than 20 days longer in the early 21st century than in the early 20th century, while the length of the heating period decreased by more than 40 days.

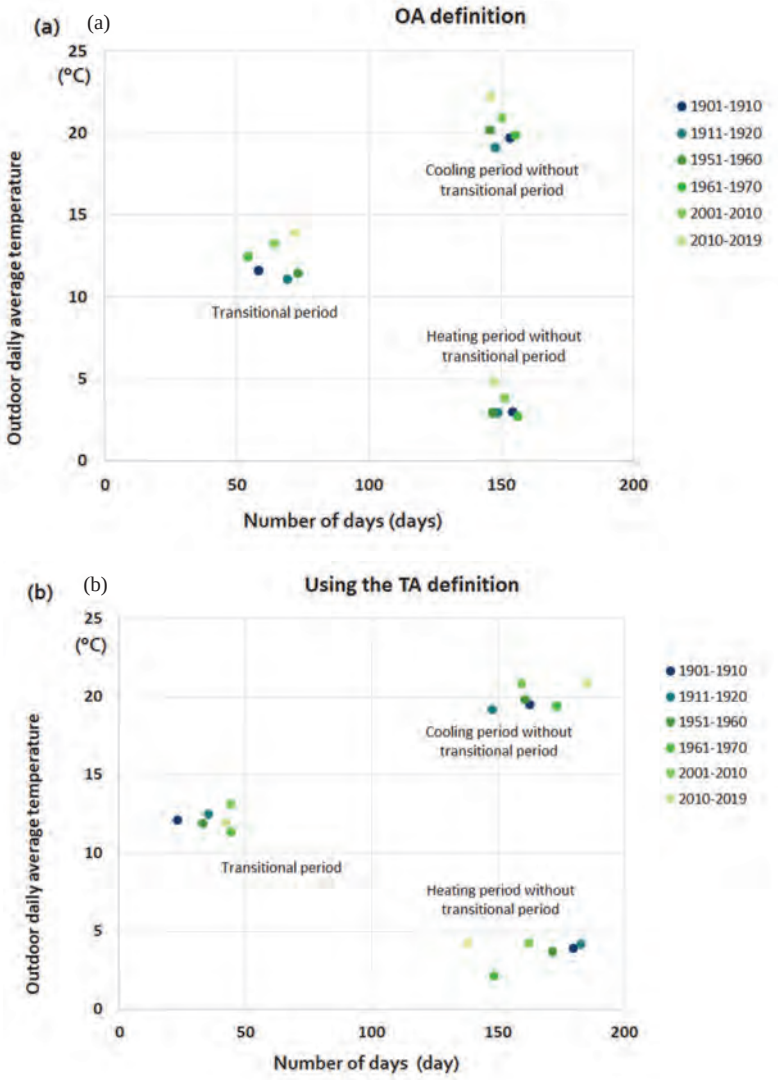

Fig. 7. The average temperature and the number of days in heating, cooling, and transitional periods for the six selected decades using the (a) OA definition and (b) TA definition.

The average temperature difference from the 119-year average was calculated for each decade for heating, cooling, and transitional periods using the OA and TA definitions (*Fig. 8*). *Fig. 8a* shows the results for OA definition. These difference values were below the average until about 1980, but after that large increases can be detected in the differences for all the three periods due to

the regional warming trend (e.g., *Lakatos* and *Bihari*, 2011) in the last few decades. When using the definition of TA, no such warming trend is seen in average temperatures for the three periods (*Fig. 8b*). However, the temperature differences simultaneously increase or decrease in the heating, cooling and transitional periods from the middle of the 20th century.

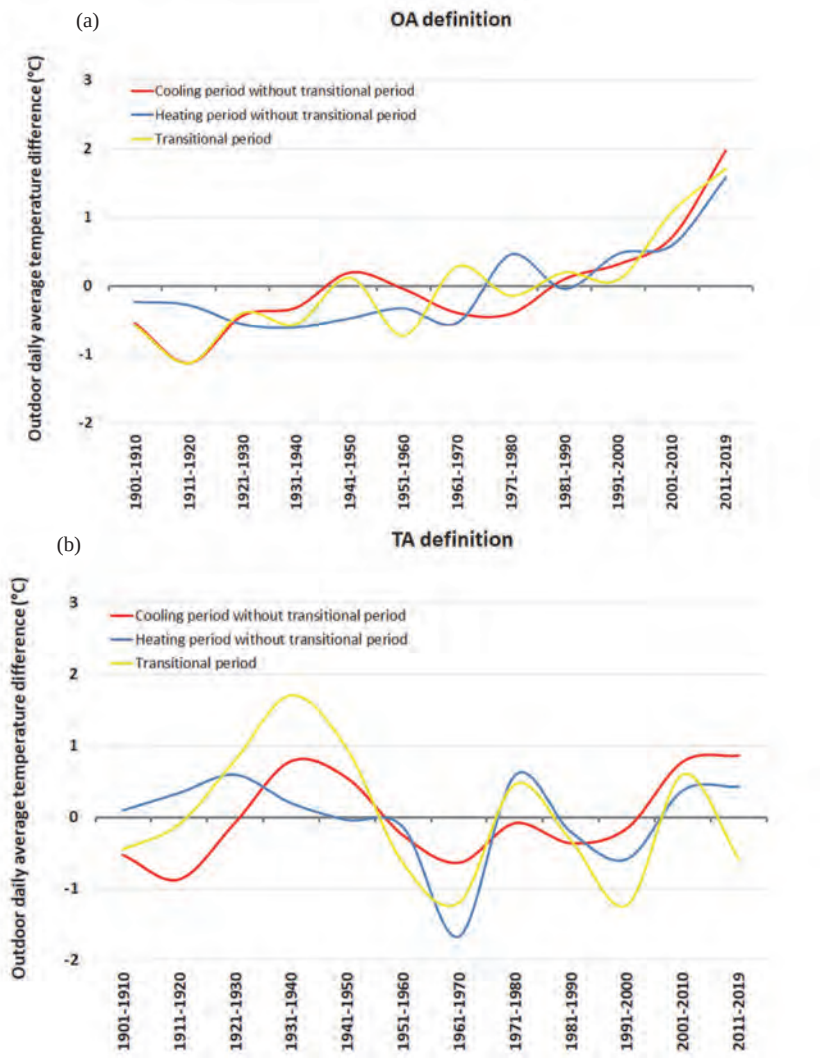

Fig. 8. Difference of the outdoor daily average temperature from the 119-year average for all the decades during 1901-2019 using (a) the OA definition and (b) the TA definition.

Based on these results, it is necessary to revise the parameters of building energy designs, especially when they depend on temperature.

5. Conclusions

In this study, we examined the daily average outdoor temperature of Budapest, the capital of Hungary, because it is an important meteorological parameter for building energy planning. For this purpose, the publicly available daily mean temperature time series of the Hungarian Meteorological Service were analyzed.

Since indoor temperature should be maintained within a stable interval throughout the year, the outdoor temperature of extremely cold and warm days is especially important in energy planning. In the case of cold days, a warming trend of 1.9 °C/100 years can be observed in Budapest, while the detected warming trend was 2.2 °C/100 years in warm days. The average standard deviation of the lower temperatures is about 2 °C greater than the deviation of the warm days. Thus, cold and warm days, with different energy demands, can be well separated if the entire year is divided into heating and cooling periods and analyzed correspondingly. For this purpose, we used three different definitions for heating and cooling periods. Furthermore, a third period (i.e., transitional period between heating and cooling periods) was also determined in the case of each definition.

Based on the analysis presented in this paper, the following main conclusions can be drawn. (1) The curves of heating and cooling periods using OA and TA definitions were quite similar for the average of 119 years. (2) The average temperature was 2 °C higher in the early 20th century than in the early 21st century in each period due to the detected regional warming trend, when using the OA definition. (3) The length of the heating period decreased by around 40 days, while the length of the cooling period increased by more than 20 days using the TA definition. (4) The use of temperature-based definitions in determining the building energy demand is certainly beneficial due to the overall warming trend. This can be especially important when developing adaptation strategies for the coming decades and the entire century.

Acknowledgement: Research leading to this paper has been supported by the following sources: the Hungarian National Scientific Research Fund under grants K-120605 and K-129162. Cs. Dian was supported by the ÚNKP-20-3 New National Excellence Program of the Ministry for Innovation and Technology from the source of the National Research, Development and Innovation Fund. Thanks for CarpatClim database: CARPATCLIM Database © European Commission - JRC. 2013. We acknowledge the E-OBS dataset from the EU-FP6 project UERRA (http://www.uerra.eu) and the Copernicus Climate Change Service, and the data providers in the ECA&D project (https://www.ecad.eu). We also acknowledge the CRU TS 4.03 dataset produced by Climatic Research Unit, University of East Anglia (http://www.cru.uea.ac.uk/). The station data of Budapest were downloaded from the public website of the Hungarian Meteorological Service (https://www.met.hu/eghajlat/magyarorszag_eghajlata/eghajlati_adatsorok/).

References

Bartholy, J. and *Pongrácz, R.*, 2007: Regional analysis of extreme temperature and precipitation indices for the Carpathian Basin from 1946 to 2001. *Glob. Planet. Change*. *57*, 83–95. https://doi.org/10.1016/j.gloplacha.2006.11.002

Bokwa, A., Dobrovolný, P., Gál, T., Geletič, J., Gulyás, Á., Hajto, M.J., Holec, J., Hollósi, B., Kielar, R., Lehnert, M., Skarbit, N., Šťastný, P., Švec, M., Unger, J., Walawender, J.P., and *Žuvela-Aloise, M.*, 2018. Urban climate in central European cities and global climate change. *Acta Climatologica 51–52*, 7–35. https://doi.org/10.14232/acta.clim.2018.52.1

Bokwa, A., Geletič, J., Lehnert, M., Žuvela-Aloise, M., Hollósi, B., Gál, T., Skarbit, N., Dobrovolný, P., Hajto, MJ., Kielar, R., Walawender, J.P., Šťastný, P., Holec, J., Ostapowicz, K., Burianová, J. and *Garaj, M.*, 2019: Heat load assessment in Central European cities using an urban climate model and observational monitoring data. *Energy Build. 201*, 53–69. https://doi.org/10.1016/j.enbuild.2019.07.023

Bottio, I., Tadiello, F., Magnelli, T., Eroe, K., Zanchini, E., Agnoloni M., and *Caliciotti, L.*, 2014: Il Teleriscaldamento in Italia. (in Italian) 53p. *AIRU and Legambiente*, Italy. https://figliodellafantasia.files.wordpress.com/2014/12/rapp_tlr_italia_2014.pdf

Cheng, X., and *Li, S.*, 2018: Interval Estimations of Building Heating Energy Consumption using the Degree-Day Method and Fuzzy Numbers. *Buildings 8*, 21 https://doi.org/10.3390/buildings8020021

Cho, S.H., Kim, W.T., Tae, C.S., and *Zaheeruddin, M.*, 2004: Effect of length of measurement period on accuracy of predicted annual heating energy consumption of buildings. *Energy Convers. Manage. 45*, 2867–2878. https://doi.org/10.1016/j.enconman.2003.12.017

Christenson, M., Manz, H., and *Gyalistras, D.*, 2006: Climate warming impact on degree-days and building energy demand in Switzerland. *Energy Convers. Manage. 47*, 671–686. https://doi.org/10.1016/j.enconman.2005.06.009

Cornes, R., van der Schrier, G., van den Besselaar, EJM., and *Jones, PD.*, 2018: An Ensemble Version of the E-OBS Temperature and Precipitation Datasets. *Journal of Geophysical Research: Atmospheres 123.* https://doi.org/doi:10.1029/2017JD028200

Directive 2010/31/EU, 2010: of the Directive 2010/31/EU European Parliament and of the Council of 19 May 2010 on the energy performance of buildings. Official J. Eur. Union, L 153, 18.6.2010, 13–35. https://eur-lex.europa.eu/legal-content/EN/TXT/PDF/?uri=CELEX:32010L0031&from=EN

E-OBS dataset: https://www.ecad.eu/ accessed on 15 April 2020

FŐTÁV Zrt.: Budapest District Heating Works Private Company Limited by Shares: http://www.fotav.hu/lakossagi-ugyfelek/kozos-kepviseletek-kepviselok-reszere/uzemviteli-megallapodas (in Hungarian) accessed on 10 February 2020

Göndöcs, J., Breuer, H., Pongrácz, R., and *Bartholy, J.*, 2018: Projected changes in heat wave characteristics in the Carpathian Basin comparing different definitions. *Int. J. Glob. Warming 16*, 119–135. https://doi.org/10.1504/IJGW.2018.10015777

Government Decree 157/2005. (VIII.15.): https://net.jogtar.hu/jogszabaly?docid=A0500157.KOR (in Hungarian) accessed on 25March 2020

Harris, I., Osborn, T.J., Jones, P., and *Lister, D.*, 2020: Version 4 of the CRU TS monthly high-resolution gridded multivariate climate dataset. *Sci. Data 7:109*. https://doi.org/10.1038/s41597-020-0453-3

Heating period definition in Germany:https://www.viessmann.at/de/wohngebaeude/ratgeber/heizperiode.html accessed on 20 July 2020

IPCC, 2013: Summary for policymakers of Climate Change 2013: The Physical Science Basis. Contribution of Working Group I to the Fifth Assessment Report of the Intergovernmental Panel on Climate Change. Cambridge University Press, Cambridge, United Kingdom and New York, NY, USA.

Janković, A., Podraščanin, Z., and *Djurdjevic, V.*, 2019: Future climate change impacts on residential heating and cooling degree days in Serbia. *Időjárás 123*, 351–370. https://doi.org/10.28974/idojaras.2019.3.6

Kaynakli, O., 2008: A study on residential heating energy requirement and optimum insulation thickness. *Renew. Energy 33*, 1164–1172. https://doi.org/10.1016/j.renene.2007.07.001

Lakatos, M., and *Bihari, Z.*, 2011: A közelmúlt megfigyelt hőmérsékleti és csapadéktendenciái. In: (eds. *Bartholy J., Bozó L., Haszpra L.*) Klímaváltozás – 2011. Klímaszcenáriók a Kárpát-medence térségére. Hungarian Academy of Science and Dept. of Meteorology, Eötvös Loránd University. Budapest. 146–169. (in Hungarian)

Martinaitis, V., 1998: Analytic calculation of degree-days for the regulated heating season. *Energy Build. 28*, 185–189. https://doi.org/10.1016/S0378-7788(98)00015-2

Masson, V., Marchadier, C., Adolphe, L., Aguejdad, R., Avner, P., Bonhomme, M., Bretagne, G., Briottet, X., Bueno, B., de Munck, C., Doukari, O., Hallegatte, S., Hidalgo, J., Houet, T., Le Bras, J., Lemonsu, A., Long, N., Moine, MP., Morel, T., Nolorgues, L., Pigeon, G., Salagnac, JL., Viguié, V., and *Zibouche, K.*, 2014: Adapting cities to climate change: A systemic modelling approach. *Urban Climate 10*, 407–429. http://dx.doi.org/10.1016/j.uclim.2014.03.004

Matzarakis, A., and *Balafoutis, C.*, 2004: Heating degree-days over Greece as an index of energy consumption. *International Journal of Climatology 24 (14)*, 1817–1828. https://doi.org/10.1002/joc.1107

Meehl, G.A., and *Tebaldi, C.*, 2004: More intense, more frequent, and longer lasting heat waves in the 21st century. *Science, 305, 5686*, 994–997. https://doi.org/10.1126/science.1098704

Mourshed, M., 2016: Climatic parameters for building energy applications:A temporal-geospatial assessment of temperature indicators. *Renewable Energy 94*, 55–71. http://dx.doi.org/10.1016/j.renene.2016.03.021

Ministry of Economy, 2005: Vyhláška č. 152/2005 Z. z. - Vyhláška Ministerstva hospodárstva Slovenskej republiky o určenom čase a o určenej kvalite dodávky tepla pre konečného spotrebiteľa. https://www.zakonypreludi.sk/zz/2005-152 accessed on 20 July 2020. (in Slovakian)

Oke, TR., 1973: City size and the urban heat island. *Atmos. Environ. 7*, 769−779. http://www.theurbanclimatologist.com/uploads/4/4/2/5/44250401/post6oke1973uhiscaling.pdf

Pongrácz R., Bartholy J., Szabó P., and Gelybó Gy., 2009: A comparison of observed trends and simulated changes in extreme climate indices in the Carpathian basin by the end of this century. *Int. J. Glob. Warming* 1 (1-2-3), 336–355. https://doi.org/10.1504/IJGW.2009.027097

Pongrácz, R., Bartholy, J., and *Dezső, Zs.*, 2010. Application of remotely sensed thermal information to urban climatology of Central European cities. *Phys. Chem. Earth 35*, 95–99. https://doi.org/10.1016/j.pce.2010.03.004

Roberts, S., 2008: Effects of climate change on the built environment. *Energy Policy 36*, 4552–4557. https://doi.org/10.1016/j.enpol.2008.09.012

Seneviratne, S.I., Lüthi, D., Litschi, M., and *Schär, C.*, 2006: Land–atmosphere coupling and climate change in Europe. *Nature, 443*, 205–209, https://doi.org/10.1038/nature05095

Short, C.A., Lomas, K.J., and *Woods, A.*, 2004: Design strategy for low-energy ventilation and cooling within an urban heat island. *Build. Res. Inform. 32*, 187–206. https://doi.org/10.1080/09613210410001679875

Spinoni, J., Lakatos, M., Szentimrey, T., Bihari, Z., Szalai, S., Vogt, J., and *Antofie, T.*, 2015: Heat and cold waves trends in the Carpathian Region from 1961 to 2010. *Int. J. Climatol. 35*, 4197–4209. https://doi.org/10.1002/joc.4279

Szalai, S., Auer, I., Hiebl, J., Milkovich, J., Radim, T., Stepanek, P., Zahradnicek, P., Bihari, Z., Lakatos, M., Szentimrey, T., Limanowka, D., Kilar, P., Cheval, S., Deak, Gy., Mihic, D., Antolovic, I., Mihajlovic, V., Nejedlik, P., Stastny, P., Mikulova, K., Nabyvanets, I., Skyryk, O., Krakovskaya, S., Vogt, J., Antofie, T., and *Spinoni, J.*, 2013: Climate of the Greater Carpathian Region. Final Technical Report. www.carpatclim-eu.org.

Talamon, A., 2014: Alacsony energiafelhasználású épületek lehetőségei Magyarországon.. PhD dissertation. University of Debrecen. 146. (in Hungarian) https://dea.lib.unideb.hu/dea/bitstream/handle/2437/204765/PhD_Disszertacio_TA_FINAL_t.pdf?sequence=5&isAllowed=y

Talamon, A., Sugár, V., and *Hartman, B.*, 2016: Fine adjustment of heating system design parameters considering the Urban Heat Island Effect in case of Hungary. Proceedings of the International Conference on Engineering and Natural Science: Summer Session (ICENS - Summer 2016). Kyoto, Japan, 297–308.

United Nations, 2015: World Urbanization Prospects: The 2014 Revision, (ST/ESA/SER.A/366). UN Department of Economic and Social Affairs, Population Division, 517. https://esa.un.org/unpd/wup/Publications/Files/WUP2014-Report.pdf

DOI:10.28974/idojaras.2021.3.5

IDŐJÁRÁS

Quarterly Journal of the Hungarian Meteorological Service
Vol. 125, No. 3, July – September, 2021, pp. 449–462

Influence of climate change on river discharges over the Sava River watershed in Bosnia and Herzegovina

Slobodan Gnjato[*], **Tatjana Popov**, **Dragutin Adžić**, **Marko Ivanišević**, **Goran Trbić**, and **Davorin Bajić**

University of Banja Luka
Faculty of Natural Sciences and Mathematics
Department of Geography
Mladena Stojanovića 2, Banja Luka,
Republic of Srpska, Bosnia and Herzegovina

**Corresponding Author e-mail: slobodan.gnjato@pmf.unibl.org*

(Manuscript received in final form September 1, 2020)

Abstract— The paper examines changes in air temperature, precipitation, and river discharges on seasonal and annual scale over the Sava River watershed in Bosnia & Herzegovina during the period 1961–2016. Based upon data gathered from 11 meteorological stations and 3 hydrological stations, hydroclimatic variables trends were established by utilizing the nonparametric Mann-Kendall test and the nonparametric Sen's slope estimator. The results show significant positive seasonal and annual trends (expect for autumn, during which upward trends were insignificant) in air temperature, whereas both positive and negative insignificant seasonal and annual precipitation trends are shown where determined for the entire watershed. Most prominent upward trends in air temperature were found in summer and afterwards in winter and spring, indicating a pronounced warming tendency over the Sava River watershed. Trends in river discharge displayed a negative tendency in all seasons. Nevertheless, a majority of estimated trends of river discharges were weak and statistically insignificant. Throughout the year, river discharges showed significant positive correlation with precipitation, whilst connection with air temperature was mostly significant and negative. The study results suggest that climate is an important factor affecting river regimes, as well as that changes in river discharges are reflecting recent abrupt changes in climatic variables.

Key-words: climate change, temperature, precipitation, river discharges, correlation, Sava River watershed

1. Introduction

On a global scale, river discharge patterns have been modified by climate system warming and numerous human actions (*Schneider et al.*, 2013; *Su et al.*, 2018). In many cases, climate change can amplify effects of human activities. Climate is one of a key drivers of freshwater ecosystem processes, as river discharge and river thermal regimes are closely tied to climatic variations. Alteration of principal climate connected drivers, such as increased temperature and modified precipitation patterns, have substantial influence on river discharge regimes and are predicted to affect hydrological cycle (*Kong* and *Pang*, 2013; *van Vliet et al.*, 2013). Hydroclimatic intensification in the context of recent global warming can result in shift in distribution and magnitude of wet/dry periods (*Madakumbura et al.*, 2019). The global rise in air temperature is expected to increase the portion of precipitation to fall as a rainfall along with the number of extreme rainfall events, reduce snowfall, and cause earlier spring melting of snow cover which will have severe impact, especially in alpine river basins which are strongly regulated by the accumulation of snow (*Kormann et al.*, 2015; *Rottler et al.*, 2020). Comprehension of hydrological dynamics of river discharge patterns, as response to recent climate variation is essential for beneficial water management as water resources in many regions have been affected in regard to volume and quality condition (*Biao*, 2017; *Jiménez Cisneros et al.*, 2014). Consequently, in order to analyze climate change impact on water resources and to build proper water management approaches, it is mandatory to determine trends and connections between river discharges and rainfall/temperature (*Gebremicael et al.*, 2017; *Lorenzo-Lacruz et al.*, 2012). Worldwide, extensive research on river discharges has been conducted at different spatio-temporal scales. Recent trends in river discharges had been determined in North America (*Déry et al.*, 2016; *Tamaddun et al.*, 2016), South America (*Pasquini* and *Depetris*, 2007), Africa (*Saraiva Okello et al.*, 2015; *Sidibe et al.*, 2018), Asia (*Souvignet, et al.*, 2014; *Tananaev et al.*, 2016), and Australia (*Zhang et al.*, 2016). Comparable researches were also undertaken in Europe. In recent pan-European studies *Masseroni et al.* (2020) and *Stahl et al.* (2010) both found downward river flow trends in the southern and eastern parts of Europe, whereas positive trends were determined in northern areas of the continent. Such patterns of river discharge changes have also been confirmed by studies on a lower scale – in Spain (*Yeste et al.*, 2018), Italy (*Billi* and *Fazzini*, 2017), the United Kingdom (*Hannaford* and *Buys*, 2012), the Nordic Region (*Wilson, et al.*, 2010), etc. Streamflow trends research over southeastern part of Europe, conducted at different spatial scales, also suggest downward tendencies of streamflow in this region. River discharge trends at 94 stations in Serbia displayed downward tendencies of annual, winter, spring, and summer discharges, whereas upward trends occurred in autumn (*Kovačević-Majkić* and *Urošev*, 2014). Observed trends were mainly insignificant (73% on annual and 76–86% on seasonal scale). Oppositely, in a study of river discharges at 24

stations in the central region of Serbia *Dimkić* (2018) reported more often occurrence of significant positive/negative annual trends claiming that they appear as a consequence of anthropogenic water consumption. Research on natural streamflow in North Macedonia indicates negative annual and seasonal trends over the whole territory, while no significant upward trend has been noted (*Radevski et al.,* 2018). Significant decline in mean annual discharges was found at 31% of stations, whereas most prominent decrease on seasonal level was found in summer at 39% of stations. A streamflow trend analysis from 44 near-natural river basins in Romania showed increase at 16% and decrease at 20% of total number of stations in mean annual river flows (*Birsan et al.,* 2014). Significant downward trends were found in summer, whereas significant increasing tendency was observed in winter and autumn. Trends in annual streamflow at 54 stations in Croatia for the most part were negative and statistically insignificant (*Čanjevac* and *Orešić,* 2015). As in previous cases, the most prominent downward trends were observed in summer, while upward trends were present in winter and autumn. The Morača River in Montenegro, which is the largest tributary of Skadar Lake, shows a significant downward trend in the mean annual flow for the period 1951–2010. However, in the period 1991–2010 there is an increasing trend of the mean annual flow, which is a consequence of the growth of the annual precipitation in the Morača River basin (*Burić et al.,* 2016). Mostly insignificant negative streamflow trends were observed throughout the Sava River basin (mainly in the lower and middle sections of the basin) at 50% of stations located over Slovenia, Croatia, Bosnia and Herzegovina (B&H), Montenegro, and Serbia (*Lutz et al.,* 2016). Relatively similar streamflow trend patterns were found for some Sava River sub-basins in Croatia (*Orešić et al.,* 2018), B&H (*Hadžić* and *Drešković,* 2014), and Serbia (*Burić et al.,* 2012).

Warming of the climate system in lately years and decades has been confirmed on global (*Fei et al.,* 2014; *IPCC,* 2014), continental [such as Europe (*van der Schrier et al.,* 2013)], and regional [such as Sava River Basin (*Bajat et al.,* 2015; *Burić et al.,* 2014; *Mamara et al.,* 2016)] levels. In B&H, increase in mean and extreme air temperatures was determined over the entire territory, especially in the northern areas which represent the lower parts of the Sava River watershed (SRW) (*Popov et al.,* 2018a; *Trbić et al.,* 2017). As opposed to air temperature, relatively distinguished precipitation patterns with insignificant trends have been reported on global scale (*Adler et al.,* 2017; *Gu & Adler,* 2015). Precipitation patterns in B&H and in the Sava River basin are principally manifested in insignificant increase/decrease in mean and extreme values (*Luković et al.,* 2014; *Popov et al.,* 2018b; *Gajić- Čipka et al.,* 2015). Area of the SRW in B&H is an important area to investigate changes in river discharges since this area is projected to experience severe climate change impact in the later half of 21st century (*Radusin et al.,* 2016). The objectives of this paper were to identify annual and seasonal trends in hydrological and climatic data series, whereas the main goal was to evaluate climate change connection/influence on river discharges in Sava River sub-basins in B&H.

In order to minimize the anthropogenic influence and to determine the influence of climate change on river discharges, unregulated rivers with continual long-term measurements were chosen for the investigation.

2. Study area

Approximately 40% (38,719 km^2) of SRW is located on the territory of B&H, while the rest of the watershed is shared by Slovenia, Croatia, Serbia, Montenegro and Albania. The total river length is about 944 km, whereas the length of the flow through Bosnia and Herzegovina is 302 km. The SRW in B&H covers central (Dinaric) and northern (Peripannonian) regions which make a total of 75% of the entire country (*Fig. 1*). The climate of the basin changes from mountain climate in the upper part to continental and moderate continental climate in the mid and lower floodplain sections of the watershed. From the southern mountainous part of the watershed towards the lowland area in the north, precipitation decreases, whereas air temperature increase (*Popov et al.*, 2018c; *Trbić et al.*, 2017). Major Sava affluents in B&H are the Una River (210 km), Vrbas River (250 km), Bosna River (275 km), and Drina River (345 km). The Sana River (146 km) is the greatest affluent of the Una River, while the Vrbanja River (95 km) is the major affluent of the Vrbas River. All major affluents of the Sava River are defined by the pluvial-nival river regimes (*Ilešič*, 1948), i.e., maximum values of discharge occur in the spring, while minimum values of river discharges take place in the summer season.

Fig. 1. Geographical location of the Sava River basin in Bosnia and Herzegovina with the meteorological and hydrological stations

3. Data and methods

Annual and seasonal discharges trends over the SRW during the period 1961–2016 were determined by using the data on mean monthly discharges from three hydrological stations (Prijedor, Vrbanja, and Doboj) located in the northern section of the watershed. The selected hydrological stations were chosen due to the fact they are the only three stations on unregulated streamflow in the whole country with continuous long-term measurements. The absence of a larger number of hydrological stations with long-term and undisturbed measurements was caused by the war events during the 1990s. As a result, the operation of a considerable number of stations was stopped for 10 or more years, while some stations stopped operating for good and some changed location.

Analysis of climatic variables in the period 1961–2016 was done based on data on mean monthly air temperatures and precipitation gathered from 11 weather stations positioned in various sections of the study area. Data on climatic and hydrological variables were delivered by the Republic Hydrometeorological Service (Republic of Srpska) and by the Federal Hydrometeorological Institute.

In order to identify statistically significant monotonic downward or upward trends, hydroclimatic data values were exposed to the nonparametric Mann-Kendall trend test and the nonparametric Sen's estimator of slope. The Mann-Kendall trend test is commonly applied to establish trends in hydroclimatic temporal sequences (*Wang et al.*, 2015), while it is especially suitable for identifying discharge trends, since the hydrological time series data are not affected by distribution and missing values (*Gebremicael et al.*, 2017). The Sen's nonparametric estimator is applied to assess trend magnitude. The statistical significance of the estimated trend values was specified at the 99% ($p \leq 0.01$) and 95% ($0.01 < p \leq 0.05$) levels. Connection among climatic variables and river discharges was determined by applying the Pearson correlation coefficient. Correlation analysis was performed for pairs of the nearest hydrological and meteorological stations. Correlation between river discharges and precipitation/air temperature can help us to reveal how climate affects river discharges as well as the connection between them. For instance, positive correlation among precipitation and river discharges suggests that changes in river discharges occur in consistency with changes in precipitation, while positive correlation among river discharges and air temperature could indicate the prevailing influence of snowmelt water in relation to evapotranspiration (negative correlation would indicate oppositely) (*Cuo et al.*, 2014).

All calculations were completed using the XLSTAT statistical software (version 2014.5.03).

4. Results and disscusion

1.1. Changes in climatic variables

Seasonal and annual averages of air temperatures and precipitation measured at 11 meteorologicaal stations over the SRW in B&H during the period 1961–2016 are displayed in *Table 1*. Mean annual temperature in the SRW increases from 1.5 °C in the southern mountain zone to 11.0–11.5 °C in the northern lowland region. Summer is the warmest season with mean air temperatures in the range from 9.4–16.0 °C in the upper to 20.6–21.3 °C in the lower part of the basin. Winter is the coldest season with mean temperatures ranging from -5.9–0.0 °C in the south to 1.3–1.4 °C in the north. Annual precipitation ranges from 1201 mm at the highest-located station in the south to 743 mm in the most northeastern station, and decreases as we move from the western and southern areas of the watershed towards the northeast. Precipitation regime across the vast majority of the watershed is characterized by wet autumn seasons and drier winters.

Table 1. Average values of seasonal and annual climatic variables measured at 11 meteorologicaal stations over the Sava River watershed in Bosnia and Herzegovina in the period 1961–2016

Staion	Winter		Spring		Summer		Autumn		Year	
	T (°C)	R (mm)	T (°C)	R (mm)	T (°C)	R (mm)	T (°C)	R (mm)	T (°C)	R (mm)
SM	1.0	226	10.7	264	19.6	272	10.8	281	10.6	1042
PR	1.0	197	11.3	231	20.6	246	11.2	263	11.0	934
BL	1.4	227	11.4	266	20.6	284	11.3	266	11.2	1040
DB	1.3	198	11.3	232	20.3	274	11.3	228	11.1	929
BN	1.4	159	11.8	191	21.1	221	11.7	175	11.5	743
TZ	1.0	184	10.6	228	19.4	284	10.7	212	10.4	906
ZE	0.9	171	10.9	197	19.8	219	10.9	219	10.6	805
BU	0.0	186	9.4	208	18.2	206	9.8	248	9.3	846
SO	-2.6	181	6.8	209	16.0	233	7.5	239	6.9	859
SA	0.6	226	9.8	228	18.9	234	10.5	259	10.0	943
BJ	-5.9	273	-0.4	269	9.4	297	2.8	366	1.5	1201

Seasonal and annual linear trends of climatic variables in the period 1961–2016 are shown in *Table 2* and *Fig. 2*. Significant ($p<0.01$) positive trends in mean annual temperatures were established across the whole study area. Estimated warming trend in the SRW was in the scope of 0.2–0.5 °C/10years with the lowest and highest warming rate recorded at Bjelašnica (highest-located station) and at

Prijedor and Banja Luka, respectively. Despite the fact that positive upward trends were observed throughout the year, the most striking warming tendency was determined in summer, during which significant ($p<0.01$) trends were present over the entire watershed. Summer temperature rise was in the scope of 0.4–0.6 °C/10years. Most prominent trends were determined for the northern part of the SRW (Prijedor, Banja Luka, and Bijeljina). Almost the entire area has also faced significant positive temperature trends in winter (0.4–0.6 °C/10years) and spring (0.2–0.4 °C/10years), whereas mainly insignificant positive trends were observed in autumn (0.1–0.3 °C/10years). Significant tendency in autumn was only determined in Prijedor and Banja Luka.

Unlike consistent temperature patterns, annual and seasonal precipitation were subjected to mainly insignificant trends of both signs. Insignificant rise in annual precipitation over most of the SRW was detected, whereas insignificant decrease was found in Prijedor, Banja Luka, and Tuzla. Estimated trend values were statistically insignificant at majority of the stations, apart from two mountain stations, Bjelašnica and Sokolac (84.3 mm/10years and 38.1 mm/10years, respectively). Most prominent positive seasonal trends were determined over the SRW in autumn (4.2–27.2 mm/10years) and spring (0.5–24.2 mm/10years). Significant upward trends in those seasons were registered in the southern basin area (Bjelašnica and Sokolac). Summer precipitation displayed trends mixed in sign with decline (-14.0–-3.4 mm/10years) in the northern areas and increase (2.5–6.7 mm/10years) in the southern part (expect in Sarajevo). Mainly insignificant trends of both sings were found in winter, where precipitation revealed spatially incoherent patterns of change.

Table 2. Decadal linear trends in average seasonal and annual climatic variables measured at 11 meteorologicaal stations over the Sava River watershed in Bosnia and Herzegovina in the period 1961–2016

Station	Winter		Spring		Summer		Autumn		Year	
	T (°C)	R (mm)	T (°C)	R (mm)	T (°C)	R (mm)	T (°C)	R (mm)	T (°C)	R (mm)
SM	**0.4**	4.9	**0.3**	2.1	**0.4**	-14.0	0.1	11.1	**0.3**	4.4
PR	**0.4**	0.7	**0.4**	0.7	**0.6**	-12.1	*0.2*	11.3	**0.5**	-2.0
BL	**0.5**	1.4	**0.4**	0.5	**0.6**	-14.0	**0.3**	7.0	**0.5**	-7.8
DB	**0.4**	0.4	**0.3**	8.4	**0.4**	-3.7	0.1	8.5	**0.3**	19.8
BN	**0.4**	-1.1	**0.4**	9.4	**0.6**	-4.3	0.2	5.3	**0.4**	9.9
TZ	*0.4*	-4.6	*0.2*	2.1	**0.4**	-3.4	0.1	9.3	**0.3**	-0.6
ZE	**0.6**	1.2	**0.3**	2.3	**0.5**	6.6	0.3	5.0	**0.4**	8.4
BU	**0.5**	-6.7	**0.3**	5.8	**0.6**	3.8	0.2	5.4	**0.4**	7.4
SO	**0.6**	6.2	**0.3**	**11.4**	**0.5**	6.7	0.2	12.0	**0.4**	**38.1**
SA	*0.4*	-5.8	*0.2*	4.2	**0.5**	-2.9	0.1	4.2	**0.3**	1.7
BJ	0.0	*28.1*	*0.2*	**24.2**	**0.4**	2.5	0.0	*27.2*	**0.2**	**84.3**

Statistical significance: **$p<0.01$** and *$p<0.05$*

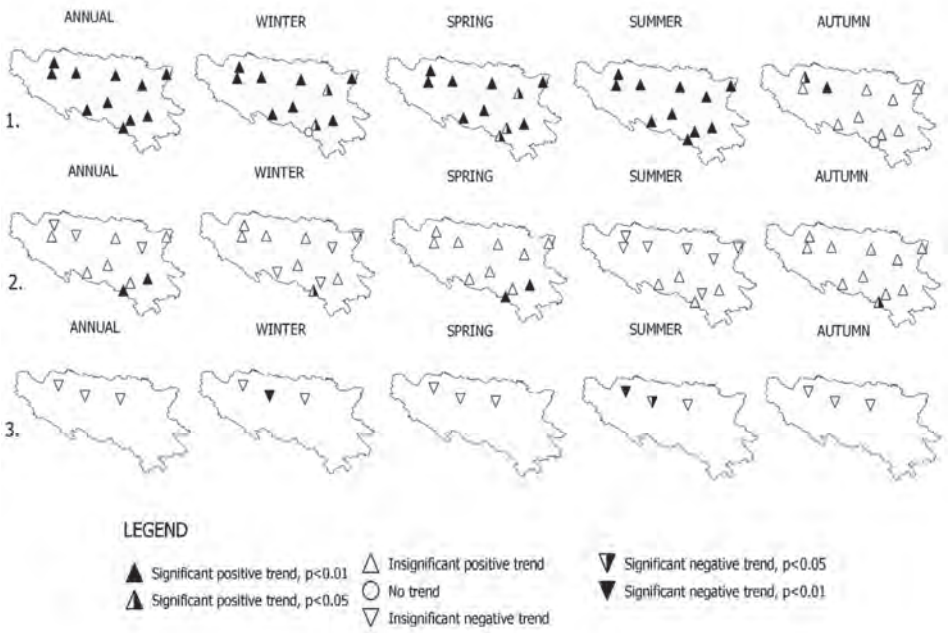

Fig. 2. Annual and seasonal trends in air temperature (1), precipitation (2), and river discharges (3).

1.2. Changes in river discharges

Decadal linear trends in mean seasonal and annual river discharges measured at 3 hydrological stations in the SRW in B&H in the period 1961–2016 are presented in *Table 3*. Mean annual river discharges displayed statistically insignificant downward tendency at all analyzed hydrological stations. The observed negative trends were also found throughout the year at all stations. Most prominent decrease in river discharges were determined in summer at the Prijedor and Vrbanja stations (-3.9 m^3/s/10years and -2.2 m^3/s/10years, respectively), whereas only significant ($p<0.01$) negative trend in winter was found at the Vrbanja station. Observed negative trends reflect the warming tendency which has been found particularly in summer and winter, along with weak positive/negative precipitation trends. However, despite the pronounced warming and weak precipitation trends, statistically insignificant discharges trends indicate that precipitation has the greatest impact on river flow. No statistically significant

negative trend was recorded at the Doboj hydrological station. This probably stems from the fact that the Bosna River basin has the largest watershed with greater capacity to address adverse influence of climate warming compared to the other two sub-basins. The weakest downward tendency was displayed in autumn (i.e., at the Prijedor and Vrbanja stations the trend was almost non-existent) which is in concordance with the low values of air temperature and precipitation trends.

Table 3. Decadal linear trends in average seasonal and annual river discharges (m^3/s) measured at 3 hydrological stations over the Sava River watershed in Bosnia and Herzegovina in the period 1961–2016

River Station	Winter		Spring		Summer		Autumn		Year	
	Q m^3/s	Trend m^3/s-1/10years	Q m^3/s	Trend m^3/s-1/10years	Q m^3/s	Trend m^3/s-1/10years	Q m^3/s	Trend m^3/s-1/10years	Q m^3/s	Trend m^3/s-1/10years
Sana (Prijedor)	98.2	-2.1	119.7	-0.5	42.0	**-3.9**	59.2	-0.6	79.6	-2.6
Vrbanja (Vrbanja)	19.5	**-2.2**	23.9	-0.2	10.5	*-1.2*	9.4	-0.5	15.8	-0.6
Bosna (Doboj)	198.9	-11.6	246.0	-4.0	105.5	-5.5	106.4	-2.6	163.9	-6.5

Statistical significance: **$p<0.01$** and *$p<0.05$*

1.3. Correlation among climatic variables and river discharges

The correlation test results are given in *Table 4 and Fig. 3.* Considering the strong connection between river discharges and climatic variables we can infer that climate is a key factor which affects river discharges in the SRW. Climatic variables displayed a good correlation with river discharges at annual scale. River discharges were significantly and positively ($p<0.01$) correlated with precipitation, whereas negative and mainly significant correlation was established between temperature and river discharges. Strong positive correlation between precipitation and river discharges (along with negative correlation between air temperatures and river discharges) throughout the year suggests that precipitation is the primary factor controlling river discharge regimes in the SRW. Moreover, significant ($p<0.01$) link amongst precipitation and river discharges was found throughout the year, especially in summer and then in winter and autumn. Higher correlation values in the summer are results of maximum, late spring/early summer rainfall events, whereas values of winter correlation coefficients suggest that the share of precipitation that falls as rain increases due to the significant warming tendency in this season. Otherwise, solid precipitation would be stored as a snow and melted later in the spring. Statistically significant connection between air temperature, and river discharge was also detected throughout the

year, except in the smaller Vrbanja River basin, where discharges greatly depend on precipitation. As expected, the strongest linkage among air temperature and river discharge were determined for summer, when high temperatures amplify the evapotranspiration process. Observed warming trends in the summer across the SRW, along with decrease in precipitation are manifested in negative tendency at each selected hydrological stations. Significant correlation was also found in spring reflecting the upward warming tendency in this season.

Table 4. Correlation among seasonal and annual climatic variables and river discharges over the Sava River watershed in Bosnia and Herzegovina in the period 1961–2016

Vrbanja station	Winter	Spring	Summer	Autumn	Year
Precipitation	**0.566**	**0.642**	**0.704**	**0.691**	**0.725**
Temperature	**-0.426**	*-0.323*	**-0.439**	-0.245	-0.393
Prijedor station	Winter	Spring	Summer	Autumn	Year
Precipitation	**0.763**	**0.624**	**0.716**	**0.680**	**0.768**
Temperature	-0.158	**-0.418**	**-0.511**	-0.174	**-0.391**
Doboj station	Winter	Spring	Summer	Autumn	Year
Precipitation	**0.719**	**0.614**	**0.776**	**0.628**	**0.671**
Temperature	-0.171	**-0.462**	**-0.457**	**-0.304**	*-0.493*

Statistical significance: **p<0.01** and *p<0.05*

Fig. 3. Correlation among river discharges and air temperature (1) / precipitation (2)

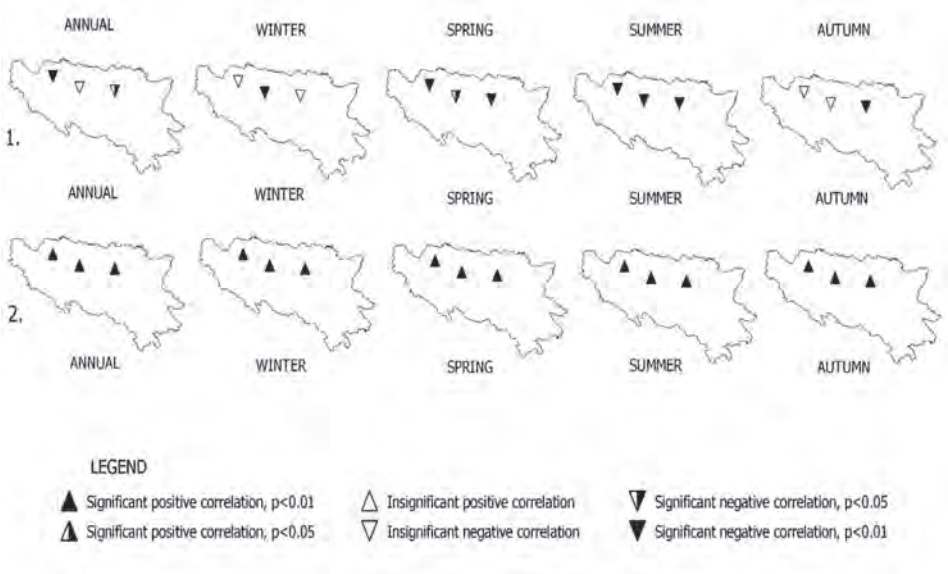

5. Conclusion

The paper investigates changes in mean hydroclimatic variables over the SRW in B&H. We provided evidence of a prominent warming tendency along with negative river discharge trends across the study area. Alterations in annual and seasonal climatic and hydrological variables over the SRW during the period 1961–2016 were analyzed based on data sets of average temperatures and precipitation from 11 meteorological stations and 3 hydrological stations. It was proved that climate is significant factor affecting the river discharge regime over the study area. Referring to the correlation analysis it was affirmed, that changes in river discharges are strongly influenced by changes in climatic variables over the entire region. The obtained results suggest that during the 1961–2016 period the whole SRW in B&H displayed prominent warming tendency on annual scale. Increasing trends in temperature were also found throughout the year, whereas precipitation displayed mainly insignificant trends mixed in sign. As expected, river discharges reflected changes in climatic variables. In a line with observed climatic trends, river discharges showed predominantly negative trends that were mainly insignificant. Given that the most prominent upward tendency was determined for summer and winter along with mainly decreasing precipitation, river discharges displayed the most notable downward tendency in these seasons. Significant positive correlation between precipitation and river discharges points out a very close connection, where changes in precipitation variability have a primary impact on the pattern of changes in river flow. Strongest link between air temperatures and river discharges found for summer indicates that significant climate warming in this part of the year has strong impact over the basin during this season. Increasing temperature and precipitation variability would probably magnify freshwater demand leading to water deficiency (especially in small watersheds) and to various negative natural and economic implications in the SRW. Efficient water management strategy is the key for sustainable water consumption. On this point, this study represents one of the first steps in an attempt to provide detailed hydroclimatic analysis of the SRW as a base for future research. Moreover, big obstacle for more efficient water management is the generally small number of hydrological stations, as well as the absence of long-term measurements. One of the major efforts regarding climate and hydrological monitoring in the future should be orientated towards increasing hydroclimatic station density over the SRW, which will allow us to adopt a more improved adaptation strategy.

Acknowledgements: The paper is the result of the research funded by the Ministry of Scientific and Technological Development, Higher Education and Information Society of the Republic of Srpska.

References

Adler, R.F., Gu, G., Sapiano, M., Wang, J-J. and *Huffman, G.J.*, 2017: Global Precipitation: Means, Variations and Trends During the Satellite Era (1979–2014). *Surv. Geophys. 38*, 679–699. https://doi.org/10.1007/s10712-017-9416-4

Bajat, B., Blagojević, D., Kilibarda, M., Luković, J. and *Tošić, I.*, 2015: Spatial analysis of the temperature trends in Serbia during the period 1961–2010. *Theor. Appl. Climatol. 121*, 289–301. https://doi.org/10.1007/s00704-014-1243-7

Biao, E. I., 2017: Assessing the impacts of climate change on river discharge dynamics in Oueme River Basin (Benin, West Africa). Hydrology. *4*, 47. https://doi.org/10.3390/hydrology4040047

Billi, P. and *Fazzini, M.*, 2017: Global change and river flow in Italy. *Glob. Planet. Change 155*, 234–246. https://doi.org/10.1016/j.gloplacha.2017.07.008

Birsan, M. V., Zaharia, L., Chendes, V. and *Branescu, E.*, 2014: Seasonal trends in Romanian streamflow. *Hydrol. Process. 28*, 4496–4505. https://doi.org/10.1002/hyp.9961

Burić, D., Ducić, V. and *Doderović, M.*, 2016: Poplave u Crnoj Gori krajem 2010. godine sa osvrtom na kolebanje proticaja Morače. Glasnik Odjeljenja prirodnih nauka, CANU, *21*, 47–64. (in Montenegrin)

Burić, D., Luković, J., Ducić, V., Dragojlović, J. and *Doderović, M.*, 2014: Recent trends in daily temperature extremes over southern Montenegro (1951–2010). *Nat. Hazards Earth Syst. Sci. 14*, 67–72. https://doi.org/10.5194/nhess-14-67-2014

Burić, D., Stanojević, G., Luković, J., Gavrilović, Lj. and *Živković, N.*, 2012: Climate change and river discharge: case study Kolubara River, Beli brod hydrological gauge. *Bull. Serbian Geogr. Soc. 92*, 123–134. https://doi.org/10.2298/GSGD1201123B

Čanjevac I, and *Orešić, D.*, 2015: Contemporary changes of mean annual and seasonal river discharges in Croatia. *Hrvat. Geog. Glas. 77*, 7–27. https://doi.org/10.21861/HGG.2015.77.01.01

Cuo, L., Zhang, Y, Zhu, F. and *Liang, L.* 2014: Characteristics and changes of streamflow on the Tibetan Plateau: A review. *J. Hydrol. 2*, 49–68. https://doi.org/10.1016/j.ejrh.2014.08.004

Déry, S. J., Stadnyk, T. A., MacDonald, M. K. and *Gauli-Sharma, B.*, 2016: Recent trends and variability in river discharge across northern Canada. Hydrol. *Earth Syst. Sci. 20*, 4801–4818. https://doi.org/10.5194/hess-20-4801-2016

Dimkić, D., 2018: Observed Climate and Hydrologic Changes in Serbia—What Has Changed in the Last Ten Years. *Proceedings 2(11)*, 616. https://doi.org/10.3390/proceedings2110616

Fei, J., Zhaohua, W., Jianping, H. and *Chassignet, E.P.*, 2014: Evolution of Land Surface Air Temperature Trend. *Nat. Clim. Change. 4*, 462–466. https://doi.org/10.1038/nclimate2223

Gajić-Čapka, M., Cindrić, K. and *Pasarić, Z.*, 2015: Trends in precipitation indices in Croatia, 1961–2010. *Theor. Appl. Climatol. 121*, 167–177. https://doi.org/10.1007/s00704-014-1217-9

Gebremicael, T. G., Mohamed, Y. A., Zaag, P. v. and *Hagos, E, Y.*, 2017: Temporal and spatial changes of rainfall and streamflow in the Upper Tekeze–Atbara river basin, Ethiopia. Hydrol. *Earth Syst. Sci. 21*, 2127–2142. https://doi.org/10.5194/hess-21-2127-2017

Gu, G. and *Adler, R.F.*, 2015: Spatial Patterns of Global Precipitation Change and Variability during 1901–2010. *J. Climate, 28*, 4431–4453. https://doi.org/10.1175/JCLI-D-14-00201.1

Hadžić, E. and *Dreško vić, N.*, 2014: Analysis of the impact of temperature and precipitation fluctuations on river flow in the Sarajevo valley. *Vodoprivreda, 46*, 65–75.

Hannaford, J. and *Buys, G.*, 2012: Trends in seasonal river flow regimes in the UK. *J. Hydrol. 475*, 158–174. https://doi.org/10.1016/j.jhydrol.2012.09.044

Ilešič, S., 1948: Rečni režimi v Jugolsaviji. Geogr. Vestn. *19*, 71–110. (in Slovenian)

IPCC, 2014: Climate change 2014: impacts, adaptation, and vulnerability. Part A: Global and sectoral aspects. Contribution of Working Group II to the Fifth Assessment Report of the Intergovernmental Panel on Climate Change [*Field, C. B., Barros, V. R., Dokken, D. J., Mach, K. J., Mastrandrea, M. D., Bilir, T. E., Chatterjee, M., Ebi, K. L., Estrada, Y. O., Genova, R. C., Girma, B., Kissel, E. S., Levy, A. N., MacCracken, S., Mastrandrea, P. R., White, L. L.* (eds.)]. Cambridge University Press, Cambridge, United Kingdom and New York, NY, USA.

Jiménez Cisneros, B. E., Oki, T., Arnell, N. W., Benito, G., Cogley, J. G., Döll, P., Jiang, T., Mwakalila, S. S., 2014: Freshwater resources. In (Eds.: *Field, C. B., Barros, V. R., Dokken, D. J., Mach, K. J., Mastrandrea, M. D., Bilir, T. E., Chatterjee, M., Ebi, K. L., Estrada, Y. O., Genova, R. C., Girma, B., Kissel, E. S., Levy, A. N., MacCracken, S., Mastrandrea, P. R.* and *White, L. L.*) Climate change 2014: impacts, adaptation, and vulnerability. Part A: global and sectoral aspects. Contribution of Working Group II to the Fifth Assessment Report of the Intergovernmental Panel on Climate Change. Cambridge University Press, Cambridge, 229–269.

Kong, Y. and *Pang, Z.*, 2013: Statistical analysis of stream discharge in response to climate change for Urumqi River catchment, Tianshan Mountains, central Asia. *Quat. Int. 336*, 44–51.. https://doi.org/10.1016/j.quaint.2013.05.002

Kormann, C., Francke, T., Renner, M. and *Bronstert, A.*, 2015: Attribution of high resolution streamflow trends in Western Austria – an approach based on climate and discharge station data. Hydrol. *Earth Syst. Sci. 19*, 1225–1245. https://doi.org/10.5194/hess-19-1225-2015

Kovačević-Majkić, J. and *Urošev, M.*, 2014: Trends of mean annual and seasonal discharges of rivers in Serbia. *J. Geogr. Inst. Cvijic. 64*, 143–160. https://doi.org/10.2298/IJGI1402143K

Lorenzo-Lacruz, J., Vicente-Serrano, S.M., López-Moreno, J.I., Morán-Tejeda, E. and *Zabalza, J.*, 2012: Recent trends in Iberian streamflows (1945–2005). *J. Hydrol. 414–415*, 463–475. https://doi.org/10.1016/j.jhydrol.2011.11.023

Luković, J., Bajat, B., Blagojević, D. and Kilibarda, M., 2014: Spatial pattern of recent rainfall trends in Serbia (1961–2009). *Reg. Environ. Change 14*, 1789–1799. https://doi.org/10.1007/s10113-013-0459-x

Lutz, S.R., Mallucci, S., Diamantini, E., Majone, B., Bellin, A. and *Merz, R.*, 2016: Hydroclimatic and water quality trends across three Mediterranean river basins. *Sci. Total Environ. 571*, 1392–1406. https://doi.org/10.1016/j.scitotenv.2016.07.102

Madakumbura, M.D., Kim, H., Utsumi, N., Shiogama, H., Fischer, E. M., Seland, Ø., Scinocca, J, F., Mitchell, D. M., Hirabayashi, Y. and *Oki, T.*, 2019: Event-to-event intensification of the hydrologic cycle from 1.5 °C to a 2 °C warmer world. *Sci. Rep. 9*, 3483. https://doi.org/10.1038/s41598-019-39936-2

Mamara, A., Argiriou, A.A. and *Anadranistakis, M.*, 2016: Recent trend analysis of mean air temperature in Greece based on homogenized data. *Theor. Appl. Climatol. 126*, 543–573. https://doi.org/10.1007/s00704-015-1592-x

Masseroni, D., Camici, S., Cislaghi, A., Vacchiano, G., Massari, C. and *Brocca, L.*, 2020: 65-year changes of annual streamflow volumes across Europe with a focus on the Mediterranean basin. *Hydrol. Earth Syst. Sci. Discuss.* Preprint. https://doi.org/10.5194/hess-2020-21

Orešić, D., Čanjevac, I. and *Plantak, M.*, 2018: Changes in flow and the discharge regime on the Ilova river. *Acta Geogr. Cro. 43–44*, 1–20.

Pasquini, A. I. and *Depetris, P. J.*, 2007: Discharge trends and flow dynamics of South American rivers draining the Southern Atlantic seaboard: An Overview. *J. Hydrol. 33*, 385−399. https://doi.org/10.1016/j.jhydrol.2006.09.005

Popov, Gnjato, S., Trbić, G. and *Ivanišević, M.*, 2018a: Recent trends in extreme temperature indices in Bosnia and Herzegovina. Carpath. *J. Earth. Env. 13*, 211–224. https://doi.org/10.26471/cjees/2018/013/019

Popov, Gnjato, S., Trbić, G. and *Ivanišević, M.*, 2018b: Analysis of extreme precipitation indices in the East Herzegovina (Bosnia and Herzegovina). *J. Geogr. Inst. Cvijic. 69*, 1–16. https://doi.org/10.2298/IJGI1901001P

Popov, T., Gnjato, S. and *Trbić, G.*, 2018c: Analysis of extreme precipitation over the Peripannonian region of Bosnia and Hercegovina. *Időjárás 122*, 433–452. https://doi.org/10.28974/idojaras.2018.4.5

Radevski, I., Gorin, S., Taleska, M. and *Dimitrovska, O.*, 2018: Natural regime of streamflow trends in Macedonia. *Geografie 123*. 1–20. https://doi.org/10.37040/geografie2018123010001

Radusin, S., Medić, V., Cero, M., Abdurahmanović, I., Avdić, S., Oprašić, S., Avdić, S., Bajrović, A.S., Muharemović, A., Prašović, S., Trbić, G., Husika, A., Krajinović, B., Stojanović, B., Zorić, B., Bajić, D., Vojinović, Đ., Arnautović-Aksić, D., Zahirović, E., Krečinić, E., Omerčić, E., Kupusović, E., Tica, G., Čustović, H., Musić, I., Čizmić, I., Koprena, J., Čolović-Daul, M., Tais, M., Voloder, M., Ljuša, M., Karabegović, M., Mataruga, M., Kotur, M., Rudan, N., Drešković,

N., Begović, P., Dekić, R., Gnjato, R., Radić, R., Hodžić, S., Kopranović, S., Stupar, S., Blagojević, V., Đurđević, V., Vujković Z., Hydrometeorological Service & Federal Hydrometeorological Service. 2016: Third national communication and second biennial update report on greenhouse gas emissions of Bosnia and Herzegovina under the United Nations framework convention on climate change. UNDP, Sarajevo

Rottler, E., France, T., Bürger, G. and *Bronstert, A.,* 2020: Long-term changes in central European river discharge for 1869–2016: impact of changing snow covers, reservoir constructions and an intensified hydrological cycle. Hydrol. *Earth Syst. Sci. 24,* 1721–1740. https://doi.org/10.5194/hess-24-1721-2020

Saraiva Okello, A. M. L., Masih, I., Uhlenbrook, S, Jewitt, G. P. W., van der Zaag, P. and *Riddell, E.,* 2015: Drivers of spatial and temporal variability of streamflow in the Incomati River basin. Hydrol. *Earth Syst. Sci. 19,* 657–673. https://doi.org/10.5194/hess-19-657-2015

Schneider, C., Laize, C. L. R., Acreman, M, C. and *Florke, M.,* 2013: How will climate change modify river flow regimes in Europe? Hydrol. *Earth Syst. Sci. 17,* 325–339. https://doi.org/10.5194/hess-17-325-2013

Sidibe, M., Dieppois, B., Mahé, G., Paturel, J.-E., Amoussou, E., Anifowose, B., and *Lawler, D.,* 2018: Trend and variability in a new, reconstructed streamflow dataset for West and Central Africa, and climatic interactions, 1950–2005. *J. Hydrol. 561,* 478−493. https://doi.org/10.1016/j.jhydrol.2018.04.024

Souvignet, M., Laux, P., Freer, J., Cloke, H., Thinh, D. Q., Thuc, T., Cullmann, J., Nauditt, A., Flügel, W. A., Kunstmann, H. and *Ribbe, L.,* 2014: Recent climatic trends and linkages to river discharge in Central Vietnam. *Hydrol. Process. 28,* 1587–1601. https://doi.org/10.1002/hyp.9693

Stahl, K., Hisdal, H., Hannaford, J., Tallaksen, L., Van Lanen, H., Sauquet, E., Demuth, S., Fendekova, M. and *Jordar, J.,* 2010: Streamflow trends in Europe: evidence from a dataset of near-natural catchments. *Hydrol. Earth Syst. Sci. 14,* 2367–2382. https://doi.org/10.5194/hess-14-2367-2010

Su, L., Miao, C., Kong, D., Duan, Q., Lei, X., Hou, Q., and *Li, H.,* 2018: Long-term trends in global river flow and the causal relationships between river flow and ocean signals. *J. Hydrol. 563,* 818–833. https://doi.org/10.1016/j.jhydrol.2018.06.058

Tamaddun, K., Kalra, A. and *Ahmad, S.,* 2016: Identification of Streamflow Changes across the Continental United States Using Variable Record Lengths. *Hydrology 3,* 24. https://doi.org/10.3390/hydrology3020024

Tananaev, N. I., Makarieva, O.M. and *Lebedeva, L. S.,* 2016: Trends in annual and extreme flows in the Lena River basin, Northern Eurasia. *Geophys. Res. Lett. 43,* 10764–10772. https://doi.org/10.1002/2016GL070796

Trbić, G., Popov, T. and *Gnjato, S.,* 2017: Analysis of air temperature trends in Bosnia and Herzegovina. Geogr. *Pannonica 21,* 68–84. https://doi.org/10.5937/GeoPan1702068T

van der Schrier, D., van den Besselaar, E.J.M., Klein Tank, A.M.G. and *Verver, G.,* 2013: Monitoring European average temperature based on the E-OBS gridded data set. *J. Geophys. Res. Atmos. 118,* 5120–5135. https://doi.org/10.1002/jgrd.50444

van Vliet, M, T, H., Franssen, W. H. P., Yearsley, J. R., Ludwig, F., Haddeland, I., Lettenmaier, D, P. and *Kabat, P.,* 2013: Global river discharge and water temperature under climate change. *Glob. Environ. Change 23,* 450–464. https://doi.org/10.1016/j.gloenvcha.2012.11.002

Wang, W., Wei, J., Shao, Q., Xing, W., Yong, B., Yu, Z. and *Jiao, X.,* 2015: Spatial and temporal variations in hydro-climatic variables and runoff in response to climate change in the Luanhe River basin, China. *Stoch. Environ. Res. Risk. A. 29,* 1117–1133. https://doi.org/10.1007/s00477-014-1003-3

Wilson, D., Hisdal, H. and *Lawrence, D.,* 2010: Has streamflow changed in the Nordic countries? – Recent trends and comparisons to hydrological projections. *J. Hydrol. 394,* 334–346. https://doi.org/10.1016/j.jhydrol.2010.09.010

Yeste, P., Dorador, J., Martin-Rosales, W., Molero, E., Esteban-Parra, M. J. and *Rueda, F. J.,* 2018: Climate-driven trends in the streamflow records of a reference hydrologic network in Southern Spain. *J. Hydrl. 566,* 55–72. https://doi.org/10.1016/j.jhydrol.2018.08.063

Zhang, X.S., Amirthanathen, G.E., Bari, M. A., Laugesen, R. M., Shin, D., Kent, D.M., MacDonlad, A. M., Turner, M. E. and *Tuteja, N. K.,* 2016: How streamflow has changed across Australia since the 1950s: evidence from the network of hydrologic reference stations. *Hydrol. Earth Syst. Sci. 20,* 3947–3965. https://doi.org/10.5194/hess-20-3947-2016

DOI:10.28974/idojaras.2021.3.6

IDŐJÁRÁS

Quarterly Journal of the Hungarian Meteorological Service
Vol. 125, No. 3, July – September, 2021, pp. 463–476

Impact of meteorological drought on vegetation in non-irrigated lands

Tahereh Sadat Mirmohammadhosseini [1], **Seyed Abbas Hosseini*** [1], **Bagher Ghermezcheshmeh** [2], and **Ahmad Sharafati** [1]

[1]*Department of Civil Engineering*
Science and Research Branch
Islamic Azad University, Tehran, Iran.

[2]*Soil Conservation and Watershed management institute*
Agricultural Research, Education and Extension Organization (AREEO)
Tehran, Iran.

**Corresponding Author e-mail: abbas_hoseyni@srbiau.ac.ir*

(Manuscript received in final form August 12, 2020)

Abstract— Drought is a natural phenomenon that causes a lot of damages annually in various sectors, including agriculture and natural resources. The aim of this study is to evaluate the influence of meteorological drought index on vegetation index. For this purpose, the standard precipitation index (SPI) as a meteorological drought index is calculated using the precipitation data of 28 meteorological stations located on the area of Lorestane province, Iran, during the years 1987–2017. Then, the vegetation condition index (VCI) is computed using normalized difference vegetation index (NDVI) images that obtained from MODIS images of Terra satellite during 2000–2017. Dry, normal, and wet years were obtained based on the SPI results for 2008, 2013, and 2016, respectively. SPI and VCI were correlated using Pearson's correlation method. The results of the relationship between VCI and SPI showed that the highest Pearson correlation coefficient related to 9-month SPI in November was equal to 0.64. Multivariate linear regression was also performed between SPI and VCI, and the results showed that SPI was significantly correlated with VCI at 5% level over a period of 9 and 12 months. Finally, a confusion matrix was used to evaluate the compliance of the SPI and VCI drought classes. Results showed that the VCI had the highest compliance in the moderate drought class with SPI.

Key-words: remote sensing, drought, standardized precipitation index, normalized difference vegetation index, vegetation condition index

1. Introduction

Drought is one of the major natural hazards and can have significant environmental and economic effects. Compared to other natural hazards, such as floods and storms, the drought scope is generally much higher (*Hagman et al*., 1984; *Wilhite* and *Vanyarkho*, 2000).Therefore, forecasting drought can be a great help in reducing the damages that caused by it. Four categories of drought can be defined as meteorological drought, hydrological drought, agricultural drought, and economical drought (*Heim Jr*, 2002; *Dai et al.*, 2004; *Bates et al.*, 2008; *Zhang et al.*, 2017; *Agana* and *Homaifar*, 2018). Reduction of precipitation causes meteorological drought, and a shortage of available water for plant growth results agricultural drought. Hydrological drought alludes to deficiency of the surface and subsurface water supply (*Zhang* and *Jia*, 2013; *Zhang et al.*, 2017). Agricultural drought usually occurs after meteorological drought and before hydrological drought.

The first economic sector affected by drought is usually agriculture. Drought leads to a decrease in agricultural production, which is affected by the intensity, duration, and spatial extent of drought stresses (*Dutta et al.*, 2015). Monitoring drought needs to be done to minimize such drought impacts. Different drought indices have been developed by a number of previous studies to determine the duration and severity of drought (*Zargar et al.*, 2011). The standardized precipitation index (SPI) is a meteorological drought index that shows the level of drought due to rainfall deficit. The SPI introduced by *McKee et al.* (1993) has been widely used. For calculation of the SPI, the precipitation depth can be employed as an input variable, and it has been extensively used to define dry and wet conditions in many countries and regions (*Guhathakurta et al.*, 2017; *Hosseini et al.*, 2020). With the availability of different satellite data and the widespread use of them, it has become possible to study drought using this method (*Dutta et al.*, 2015).

Studying the drought using remote sensing data has become possible with the availability of different satellite data and the widespread use of them. Using remote sensing indicators, the drought effects on plants and agriculture can be studied, and more accurate and effective results can be achieved for drought modeling (*Heim Jr*, 2002).

So far, many studies have been done on the extraction of drought indicators from satellite images, most of them show uncertainty that sometimes leads to the inefficiency of drought forecasting models. More careful selection and processing of images to extract indicators can increase their quality and ultimately lead to greater efficiency in drought forecasting models (*Rhee et al*., 2010).

Based on the studies, the relationship between the NDVI and SPI was investigated over three periods of 1, 3, and 6 months in Australia (*Caccamo et al.*, 2011). The results showed that the highest correlation coefficient between NDVI and SPI was obtained at the 6 months period.

In a similar study in the United States, among 1 to 12-month SPIs, the highest correlation coefficient was reported between the NDVI and 3-month SPI (*Ji* and *Peters*, 2003).

There are important factors such as vegetation characteristics, the studied period, soil characteristics, and the distribution and intensity of rainfall that affect the occurrence of the highest correlation coefficient between NDVI and SPI (*Moreira et al.*, 2008).The effectiveness of using the VCI in monitoring drought in different parts of the world has also been evaluated (*Shahabfar et al.*, 2012).

There is a high correlation between the VCI that obtained from Advanced Very High Resolution Radiometer (AVHRR) images and agricultural production in South America, Africa, North America, Europe and Asia, especially, in the critical periods of growth (*Singh et al.*, 2003).

Shad et al. (2017) examined the drought monitoring using vegetation indicators and MODIS data in Isfahan province. For this purpose they used 3-month SPI and obtained Pearson correlation coefficients for the SPI index with NDVI, VCI, and TCI. The correlation coefficients showed that the NDVI and VCI can be good indices for monitoring drought in that region. *Dutta et al.* (2015) used long-term NDVI images to monitor agricultural drought. Comparison of SPI with VCI showed correlation coefficient value equal to 0.75, which supported the efficiency of this remote sensing index to assess agricultural drought.

Zhang et al. (2017) concluded in their research that VCI can detect the onset of drought and the impact of it. The obvious advantage of VCI is the ease of calculation and the lack of need to view the station.

Previous studies indicate that there is a relationship between the meteorological drought and agricultural drought. Both types of drought are basically caused by a lack of rainfall, and agricultural drought occurs with a time lag from meteorological drought. The relationship between the two droughts varies according to location, climate, and morphometry. Another point is how these two droughts relate to each other, and this relationship may be linear or nonlinear and may be different for each region.

In this study, first the relationship between the meteorological and agricultural drought is investigated by using the SPI and VCI, then the time lag between occurrences of vegetation drought and meteorological drought in Lorestan province (western part of Iran) is examined, and also the rate of adaptation of drought classes for SPI and VCI is determined. Finally, based on the meteorological drought, vegetation drought is predicted.

In this research, non-irrigated vegetation of Lorestan province is considered to be studied because of being the dominant vegetation in that region. The results of this study will help farmers find out when the crop cultivation should be done according to the region's precipitation, in order to get a good harvest.

2. The study area and data used

Lorestan province is located in the western part of Iran on the Zagros mountain range. The area is highly mountainous and covers about 28559 square kilometers. Most of the province's areas are covered by the Zagros Mountains. *Fig. 1* shows the position of the studied area and the rain gauge stations located in this area.

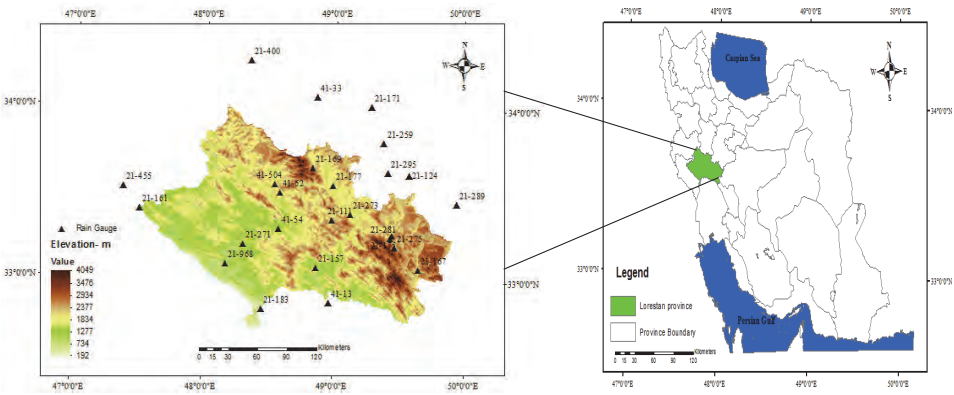

Fig 1. Geographic location of the studied area along with selected rain gauge stations

Lorestan is a highly elevated province with different climates, changing from north to south and from east to west. The maximum recorded temperature in the province is +47.4 °C and the minimum is -35 °C. The average annual precipitation is 550 mm. For this study, the monthly rainfall data of 28 rain gauge stations located in and around the province were used. The stations were selected based on the length of the statistical period, appropriate spatial coverage and statistical accuracy in Lorestan province, and on the reliability of their statistical data. The time period studied in this study was considered from 1987 to 2017. The data were collected from the ministry of water and power of the country. The data quality analysis was performed using the double mass curve method, and it was revealed that the database is homogeneous. The missing data gaps were filled using a regression method and by considering high determination coefficients with the nearest suitable station. *Table 1* shows the specifications of the selected stations.

Table1. Specifications of the selected stations

No.	Station name	Station code	Latitude (degree)	Longitude (degree)	Elevation (m.a.s.l)
1	Afrineh	21-177	33.31	47.89	820
2	Aghjanbolaghi	21-111	34.85	48.05	1803
3	Alraj	21-504	34.12	49.32	1870
4	Astaneh	41-54	33.89	49.36	2060
5	Aznacham	21-271	33.40	49.40	1830
6	Chamanjir	21-175	33.44	48.25	1140
7	Chamchit	21-281	33.56	48.98	1290
8	Daretakht	21-275	33.58	49.38	1940
9	Dartoot	21-157	33.74	46.65	907
10	Dehnu	21-167	33.52	48.78	1770
11	Emarat	41-959	33.87	49.58	2100
12	Ghahavand	41-62	34.86	49.00	1625
13	Ghelyan	21-968	33.05	49.38	1750
14	Kakareza	21-169	33.72	48.25	1530
15	Kamandan	21-273	33.31	49.43	2080
16	Kazemabad	21-400	33.13	49.68	2000
17	Khandab	41-33	34.40	49.18	1650
18	Kheiabad	21-32	34.47	48.62	1763
19	Khomein	41-13	33.64	40.07	1800
20	Poldokhtar	21-183	33.16	47.71	650
21	Polezal	21-189	32.81	48.08	300
22	Sarab	21-171	33.79	48.20	1520
23	Sazmanab	21-124	33.78	48.80	1490
24	Sorkhab	21-289	33.14	48.63	770
25	Talezang	21-295	32.87	48.77	440
26	Vanayi	21-259	33.91	48.59	2000
27	Vargach	21-161	33.57	46.82	783
28	Zoorabad	21-455	32.06	48.57	42

3. Methodology

3.1. Standardized precipitation index (SPI)

SPI was introduced by McKee in 1993 based on the probability of precipitation for each time period (*McKee et al*., 1993). It can be calculated for different ranges

(*Mishra et al.*, 2009). SPI is computed by fitting the gamma density function on the distribution of rainfall frequency for a given station, and the cumulative distribution function is turned into the standard normal distribution (with mean zero and variance of unity) via equal probabilities. The classification of the SPI were proposed by *Mckee et al.* (1993) according to *Table 2*.

Table 2. Drought classification based on SPI values (*Mckee et al.*, 1993)

SPI Value	Classification
≥2	Extreme wet
(1.5) - (1.99)	Very wet
(1.0) - (1.49)	Moderate wet
(0.99) - (-0.99)	Normal
(-1.0) - (-1.49)	Moderate drought
(-1.5)- (-1.99)	Severe drought
≤ -2	Extreme drought

3.2. Remote sensing data

3.2.1. Normalized difference vegetation index (NDVI)

The normalized difference vegetation index (NDVI) is an index of plant greenness or photosynthetic activity, and it is one of the most commonly used vegetation indices (*Bhandari et al.*, 2012; *Vrieling et al.*, 2013; *Zhu et al.*, 2013; *Choubin et al.*, 2019; *Viana et al.*, 2019). Vegetation indices are based on the observation that different surfaces reflect different types of light differently. A photosynthetically active vegetation, in particular, absorbs most of the red light that hits it while reflecting much of the near infrared light. NDVI is calculated based on the following equation:

$$\mathrm{NDVI} = (\mathrm{NIR} - \mathrm{R})/(\mathrm{NIR} + \mathrm{R}) , \quad (1)$$

where the NIR is the infrared band and R is the red band, and the band number is obtained in different satellite images. Images of the monthly MODIS-NDVI time series (MODIS-13) used in this study were taken from the Terra satellite for the years 2000 to 2017. Data from this index were used at 16-day intervals at a resolution of 250 meters.

3.2.2. Vegetation condition index (VCI)

Vegetation condition index (VCI) was first obtained by Kogan in 1995 based on NDVI images to eliminate the effect of climatic and topographic differences (*Kogan*, (1995). This index is defined according to the following equation:

$$VCI = \frac{NDVI_j - NDVI_{min}}{NDVI_{max} - NDVI_{min}} \times 100 , \quad (2)$$

where $NDVI_{max}$ and $NDVI_{min}$represent maximum and minimum NDVI of each pixel calculated for each month and j represents the index of the current month.

The results of VCI are better than the NDVI in terms of rainfall, especially in areas that are geographically heterogeneous. Using the time series data of the NDVI that extracted, the vegetation condition index (VCI) time series data were calculated based on Eq. (2).

3.3. Non-irrigated lands extraction

By using the Google Earth satellite imagery feature, the range of non-irrigated lands in Lorestan province was extracted and then about 200 points were determined on the areas that were extracted as non-irrigated lands. NDVI and VCI values for each of the 200 points were extracted using the GIS software. By using SPI calculated for 28 stations, SPI values were interpolated by the inverse distance weighting (IDW) method for the rest of the province. Thus, SPI were obtained for every 200 extracted points. It should be noted that these points were selected in such a way that at a distance of at least 500 meters, their use is completely non-irrigated, thus VCI index cells are completely pure non-irrigated and do not interfere with other uses.

3.4. The confusion matrix of meteorological drought index and vegetation

In this study, the degree of compatibility of drought classes between the meteorological and agricultural drought was examined using a confusion matrix, and it was showed, which class of these two droughts have a higher compatibility with each other during drought occurrences. Therefore, in order to use this matrix, it is necessary to make the same classification between the SPI and VCI. For this purpose, drought classification for both indices was performed in five classes based on *Table 3*.

Table 3: Classification of the SPI and VCI values (*Kogan*, 2001)

Class No.	SPI	Classification	VCI
1	≤ -1/5	Extreme	< 20
2	-1/5<SPI<0	Moderate	20-40
3	0<SPI<1	Normal	40-60
4	1<SPI<1/5	Moderate wet	60-70
5	≥ 1/5	Severe wet	70 <

4. Results and discussions

Using monthly precipitation data from 28 rain gauge stations, the 1, 3, 6, 9, and 12-month SPIs from 1987 to 2017 were calculated. The SPI chart against the year was drawn for each of the stations. SPI changes range from -2 to +2, with negative values indicating dry years and positive values indicating wet years. Drought fluctuations are greater in the short term compared to the long term.

According to the calculated SPIs, the year, in which the SPI values were negative and covered the entire area of the region, and also the year before and after that was usually in the dry period, was considered to determine the representative of the dry year. Similarly, the year in which the SPI values were positive and covered the entire area of the region, and also the year before and after that was usually in the wet period, was considered to determine the representative of the wet year. For the normal year, the year, in which the SPI values were between -0.99 and 0.99, and the year before and after that was in the normal year period was considered as the representative of the normal year. Thus, 2008, 2013, and 2016 were considered as dry, normal, and wet years, respectively. *Fig. 2* shows the SPI and VCI classification maps for 2008, 2013 and 2016.

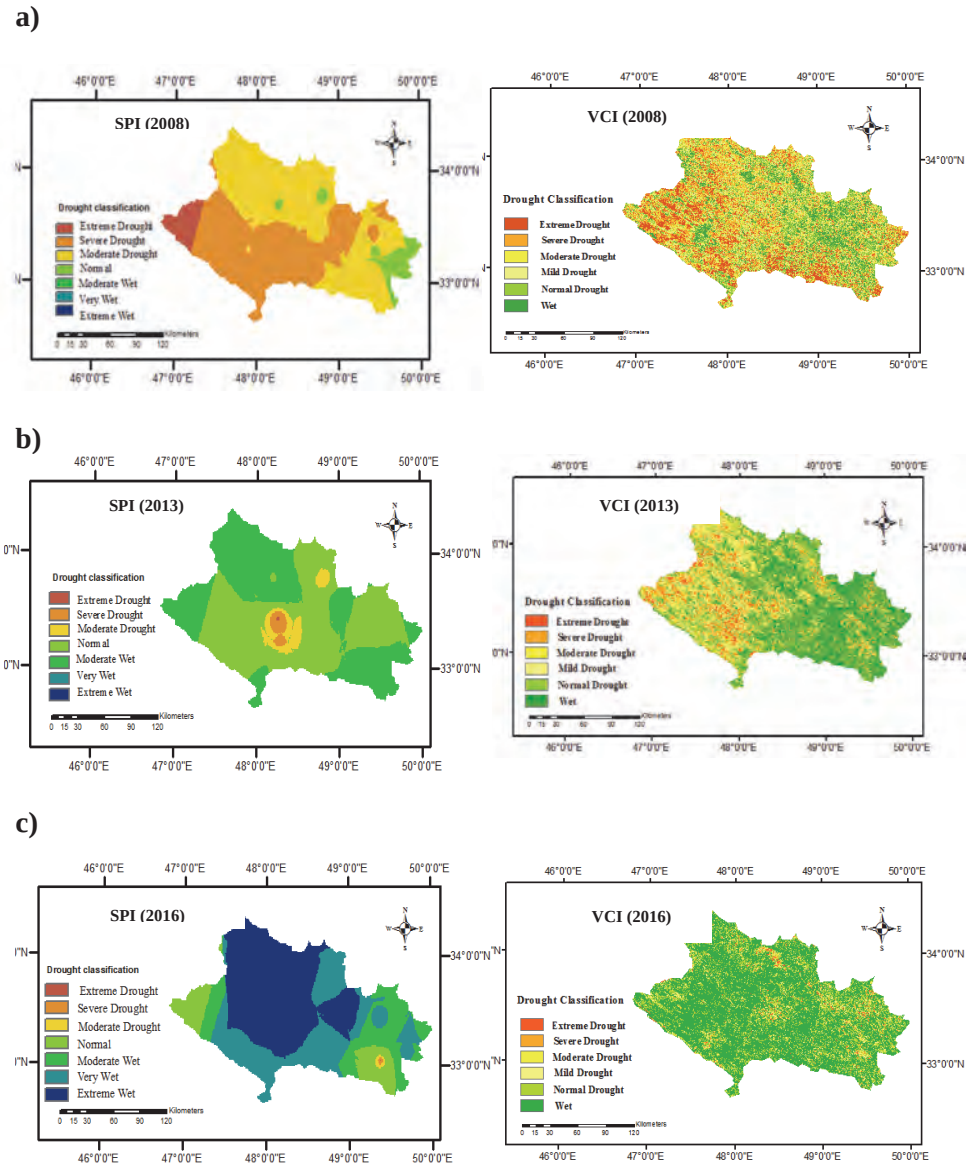

Fig. 2. SPI and VCI classification maps in Lorestan province in the years: a) 2008, b) 2013, and c) 2016.

The Pearson correlation coefficient was used to investigate the relationship between SPI and VCI. For this purpose, the correlation between SPI and VCI was

calculated for three years (2008, 2013, and 2016). The Pearson correlation coefficients were calculated between SPI values for the months (January, February, March, April, May June, October, and December), and VCI during the growth period (March, April, May, and June) for 200 selected points in non-irrigated land. Also, a multivariate linear regression was performed between SPI and VCI to obtain the best relationship between SPI with different time series and VCI by the correlation coefficient between them.

The results of the correlation between the VCI in March and SPI showed that in 2008, the highest correlation coefficient was related to the 9-month SPI in November by a value of 0.64. Also, in the same year, the highest correlation coefficient of multivariate linear regression was related to the 9 and 12-month SPI and was equal to 0.55. It shows that the value of this correlation increases at the beginning of the growing season. *Table 4* Correlation coefficients between VCI in March and SPI in 2008.

Table 4. Correlation coefficients between VCI in March and SPI in 2008

SPI	Apr	May	Jun	Oct	Nov	Dec	Jan	Feb	Mar	Multi regression
SPI 1	-0.17	0.33	0.19	0.16	0.35	0.33	0.1	0.22	0.22	0.37
SPI 3	0.15	0.25	0.25	0.29	0.36	0.37	0.32	-0.21	-0.16	0.38
SPI 6	0.27	-0.29	0.27	0.11	0.36	0.37	0.32	0.33	0.30	0.45
SPI 9	0.50	0.50	0.31	0.51	**0.64**	0.47	0.51	0.52	0.51	**0.55**
SPI 12	0.50	0.51	0.51	0.53	0.52	0.29	0.34	0.39	0.43	**0.55**

Also, the correlation results that obtained from the relationship between VCI in April, May, and June with SPI showed that the highest correlation coefficient for multivariate regression is related to the 9 and 12-month SPI and is equal to 0.57, 0.62, and 0.75, respectively.

Table 5 shows the correlation coefficients between the 9 and 12-month SPI and VCI in April, May, and June.

Table 5. Correlation coefficients between the 9 and 12-month SPI and VCI in April, May, and June in 2008

VCI	SPI9	SPI12	Multi regression
April	0.5	0.41	0.57
May	0.56	0.59	0.62
June	0.61	0.55	0.75

According to *Table 5*, the highest correlation coefficient between SPI and VCI in March, April, May, and June was observed for VCI in June. The results of the previous research showed that the highest correlation coefficient between SPI and vegetation index is related to the 9-month SPI (*Liu et al.*, 2020). *Yagci et al.* (2015) also observed a good correlation between VCI and SPI values, and VCI was introduced as a suitable index for using in the product value prediction model along with NDVI.

The results of the present study showed that the correlation coefficient for multivariate linear regression (April, May, June, October, October, November, and December) has higher value than that of the single-variable regression of each month.

Eq. (3) presents the regression, in which the significance level of the F test is less than 0.05, indicating that the regression model was appropriate and the SPI values have been able to significantly predict changes in the VCI and to affect VCI.

$$\text{VCI (June)} = 1.4\ \text{SPI (April)} + 0.46\ \text{SPI (May)} - 0.63\ \text{SPI (June)} + 0.09\ \text{SPI (October)} - 0.27\ \text{SPI (November)} - 1.15\ \text{SPI (December)} + 0.87. \quad (3)$$

The results of the confusion matrix for the 9-month SPI in November and the VCI in June are presented in *Table 6*. According to this table, the highest compatibility between these two indices occured in moderate drought conditions.

Table 6. Confusion matrix for 9-months SPI in November and VCI in June

VCI \ SPI	1	2	3	4	5
1	0.2613	0.2445	0.2422	0.2717	0.065
2	0.4282	**0.571**	0.3422	0.339	0.1203
3	0.439	0.3564	0.3761	0.2878	0.1088
4	0.2767	0.2726	0.3935	0.2454	0.1417
5	0.0802	0.1886	0.3418	0.1475	0.2017

5. Conclusions

In the present study, meteorological data and remote sensing data were used to investigate the effect of meteorological drought on agricultural drought and their relationship. First, the SPI index for 28 rain gauge stations of Lorestan province was calculated for the years from 1987 to 2017. Then, by using NDVI images that extracted from Terra MODIS, the VCI was calculated and finally the relationship between SPI and VCI was examined.

According to the results of SPI, for Lorestan province, dry, normal, and wet years were selected in 2008, 2013, and 2016, respectively.

The results obtained from the investigation of the relationship between SPI and VCI showed that the highest correlation coefficient of VCI was for the 9-month SPI in November. Based on the previous studies, there was a good correlation between SPI and VCI (*Dutta et al.*, 2015), which confirms the results of this study.

It should be noted that in the growing season of vegetation cover, VCI calculation is faced with less error and the correlation between SPI and VCI is higher.

Due to the different environmental and climatic conditions and vegetation, similar results cannot be expected in different regions and the relationship between each of the agricultural drought indicators that extracted from satellite images should be studied separately in each region. Depending on the specific climatic conditions and vegetation, it is necessary to select the appropriate index for monitoring agricultural drought for each region.

According to the results of multivariate regression between SPI and VCI, the correlation coefficient between the 9 and 12-months is higher than other time series, which indicates that non-irrigated products in November are dependent on the rainfall of 9 or 12 months ago.

According to the results, due to the fact that the growth of the crop is faster in the two months of May and June, if the crop faced with a lack of rainfall, the study of VCI in these two months is more important than in other months.

In the equation which resulted from the regression of VCI with SPI, the significance level of F test was less than 0.05, which indicates that the regression model is appropriate and SPI variables in different months have been able to predict the changes of VCI variables and affect them. The results of the confusion matrix showed that the VCI was most compatible with SPI in the average moderate drought class.

References

Agana, N.A. and *Homaifar, A.*, 2018: EMD-based predictive deep belief network for time series prediction: an application to drought forecasting. *Hydrology, 5*, 18. https://doi.org/10.3390/hydrology5010018

Bates, B.C., Kundzewicz, Z.W., Wu, S., and *Palutikof, J.P.*, 2008: Climate Change and Water. Paper of the Intergovernmental Panel on Climate Change. IPCC Secretariat: Geneva.

Bhandari, A.K., Kumar, A., and *Singh, G.K.*, 2012: Feature extraction using Normalized Difference Vegetation Index (NDVI): A case study of Jabalpur city. *Procedia Technology 6*, 612–621. https://doi.org/10.1016/j.protcy.2012.10.074

Caccamo, G., Chisholm, L.A., Bradstock, R.A., and *Puotinen, M.L.*, 2011: Assessing the sensitivity of MODIS to monitor drought in high biomass ecosystems. *Remote Sens. Environ. 115*, 2626–2639. https://doi.org/10.1016/j.rse.2011.05.018

Choubin, B., Soleimani, F., Pirnia, A., Sajedi-Hosseini, F., Alilou, H., Rahmati, O., Melesse, A.M., Singh, V.P., and *Shahabi, H.*, 2019: Effects of drought on vegetative cover changes: Investigating spatiotemporal patterns, In: Extreme Hydrology and Climate Variability. Elsevier, 213–222. https://doi.org/10.1016/B978-0-12-815998-9.00017-8

Dai, A., Trenberth, K.E., and *Qian, T.*, 2004: A global dataset of Palmer Drought Severity Index for 1870–2002: Relationship with soil moisture and effects of surface warming. *J. Hydrometeorol. 5*, 1117–1130. https://doi.org/10.1175/JHM-386.1

Dutta, D., Kundu, A., Patel, N.R., Saha, S.K., and *Siddiqui, A.R.*, 2015: Assessment of agricultural drought in Rajasthan (India) using remote sensing derived Vegetation Condition Index (VCI) and Standardized Precipitation Index (SPI). *Egyptian J. Remote Sens.Space Sci. 18*, 53–63. https://doi.org/10.1016/j.ejrs.2015.03.006

Guhathakurta, P., Menon, P., Inkane, P.M., Krishnan, U., and *Sable, S.T.*, 2017: Trends and variability of meteorological drought over the districts of India using standardized precipitation index. *J. Earth Syst. Sci. 126*. https://doi.org/10.1007/s12040-017-0896-x

Hagman, G., Beer, H., Bendz, M., and *Wijkman, A.*, 1984: Prevention better than cure. Report on human and environmental disasters in the Third World. 2.

Heim Jr, R.R., 2002: A review of twentieth-century drought indices used in the United States. *Bull. Amer. Meteorol. Soc. 83*, 1149–1166. https://doi.org/10.1175/1520-0477-83.8.1149

Hosseini, T.S.M., Hosseini, S.A., Ghermezcheshmeh, B., and *Sharafati, A.*, 2020: Drought hazard depending on elevation and precipitation in Lorestan, Iran. *Theor. Appl. Climatol. 142*, 1369–1377. https://doi.org/10.1007/s00704-020-03386-y

Ji, L. and *Peters, A.J.*, 2003: Assessing vegetation response to drought in the northern Great Plains using vegetation and drought indices. *Remote Sens. Environ. 87*, 85–98. https://doi.org/10.1016/S0034-4257(03)00174-3

Kogan, F.N., 1995: Application of vegetation index and brightness temperature for drought detection. *Adv. Space Res. 15*, 91–100. https://doi.org/10.1016/0273-1177(95)00079-T

Kogan, F.N., 2001: Operational space technology for global vegetation assessment. *Bull. Amer. Meteorol. Soc. 82*, 1949–1964. https://doi.org/10.1175/1520-0477(2001)082<1949:OSTFGV>2.3.CO;2

Liu, Q., Zhang, S., Zhang, H., Bai, Y., and *Zhang, J.*, 2020: Monitoring drought using composite drought indices based on remote sensing. *Sci. Total Environ. 711*, 134585.

Mckee, T.B., Doesken, N.J., and Kleist, J., 1993: The relationship of drought frequency and duration to time scales. AMS 8th Conference on Applied Climatology, 179–184. doi:citeulike-article-id:10490403

Mishra, A.K., Singh, V.P., and *Desai, V.R.*, 2009: Drought characterization: a probabilistic approach. *Stoch. Environ. Res. Risk Assess. 23*, 41–55. https://doi.org/10.1007/s00477-007-0194-2

Moreira, E.E., Coelho, C.A., Paulo, A.A., Pereira, L.S., and Mexia, J.T., 2008: SPI-based drought category prediction using loglinear models. *J. Hydrol. 354*, 116–130. https://doi.org/10.1016/j.jhydrol.2008.03.002

Rhee, J., Im, J., and *Carbone, G.J.*, 2010: Monitoring agricultural drought for arid and humid regions using multi-sensor remote sensing data. *Remote Sens. Environ. 114*, 2875–2887. https://doi.org/10.1016/j.rse.2010.07.005

Shad, M.S., Ildoromi, A., and *Akhzari, D.*, 2017: Drought Monitoring Using Vegetation Indices and MODIS Data (Case Study: Isfahan Province, Iran). *J. Rangeland Sci. 7*, 148–159.

Shahabfar, A., Ghulam, A., and *Eitzinger, J.*, 2012: Drought monitoring in Iran using the perpendicular drought indices. *Int. J. of Appl. Earth Observ.Geoinf.18*, 119–127. https://doi.org/10.1016/j.jag.2012.01.011

Singh, R.P., Roy, S., and *Kogan, F.*, 2003: Vegetation and temperature condition indices from NOAA AVHRR data for drought monitoring over India. *Int. J. Remote Sens. 24*, 4393–4402. https://doi.org/10.1080/0143116031000084323

Viana, C.M., Oliveira, S., Oliveira, S.C., and *Rocha, J.*, 2019: Land use/land cover change detection and urban sprawl analysis, In: Spatial Modeling in GIS and R for Earth and Environmental Sciences. Elsevier, 621–651. https://doi.org/10.1016/B978-0-12-815226-3.00029-6

Vrieling, A., De Leeuw, J., and *Said, M.Y.*, 2013: Length of growing period over Africa: Variability and trends from 30 years of NDVI time series. *Remote Sens. 5*, 982–1000. https://doi.org/10.3390/rs5020982

Wilhite, D.A. and *Vanyarkho, O. V*, 2000: Drought: Pervasive impacts of a creeping phenomenon.

Yagci, A.L., Di, L., and *Deng, M.*, 2015: The effect of corn-soybean rotation on the NDVI-based drought indicators: A case study in Iowa, USA, using vegetation condition index. *GISci. Remote Sens. 52*, 290–314. https://doi.org/10.1080/15481603.2015.1038427

Zargar, A., Sadiq, R., Naser, B., and Khan, F.I., 2011: A review of drought indices. *Environmental Reviews, 19*, 333–349. https://doi.org/10.1139/a11-013

Zhang, A. and *Jia, G.*, 2013: Monitoring meteorological drought in semiarid regions using multi-sensor microwave remote sensing data. *Remote Sens. Environ. 134*, 12–23. https://doi.org/10.1016/j.rse.2013.02.023

Zhang, L., Jiao, W., Zhang, H., Huang, C., and *Tong, Q.*, 2017: Studying drought phenomena in the Continental United States in 2011 and 2012 using various drought indices. *Remote Sens. Environ. 190*, 96–106. https://doi.org/10.1016/j.rse.2016.12.010

Zhu, Z., Bi, J., Pan, Y., Ganguly, S., Anav, A., Xu, L., Samanta, A., Piao, S., Nemani, R.R., and *Myneni, R.B.*, 2013: Global data sets of vegetation leaf area index (LAI) 3g and fraction of photosynthetically active radiation (FPAR) 3g derived from global inventory modeling and mapping studies (GIMMS) normalized difference vegetation index (NDVI3g) for the period 1981 to. *Remote Sens. 5*, 927–948. https://doi.org/10.3390/rs5020927

DOI:10.28974/idojaras.2021.3.7

IDŐJÁRÁS

Quarterly Journal of the Hungarian Meteorological Service
Vol. 125, No. 3, July – September, 2021, pp. 477–490

Spatiotemporal distribution of heavy and extreme snowfalls in the Transcarpathian region

Ruslan Ozymko[1,3*], **Alina Semerhei-Chumachenko**[2], and **Vasyl Manivchuk**[3]

[1]*Uzhhorod National University*
Narodna Square 3, Uzhhorod, Ukraine

[2]*Odesa State Environmental University*
Lvivska Street, 15, Odesa, Ukraine

[3]*Transcarpathian Regional Center of Hydrometeorology*
Slovianska Embankment, 5, Uzhhorod, Ukraine

**Corresponding author E-mail: ruslanozymko@gmail.com*

(Manuscript received in final form August 31, 2020)

Abstract— This paper presents a spatiotemporal analysis of the dynamics of heavy and extreme snowfalls in the Transcarpathian region during 1990-2019. Data on snowfalls are obtained from the observation points of the state hydrometeorological network of the Transcarpathian Regional Center of Hydrometeorology. Also there are data included from the Pozhezhevska snow avalanche station (Ivano-Frankivsk region) as a representative observation point for the highland zone of the eastern part of the Transcarpathian region. The analysis took into account the date of snowfall, the amount of precipitation that fell during the snowfall,l and its duration. The recurrence of different indicators of snowfall distribution was calculated for each observation point separately for the specified thirty-year period. Some results were mapped by the isolines using kriging interpolation. Spatio-temporal heterogeneities and regularities in the distribution of heavy and extreme snowfalls have been revealed.
Key-words: heavy snowfall, extreme snowfall, Transcarpathian region, recurrence, trend, distribution, kriging interpolation

1. Introduction

Precipitation is one of the main indicators of climate. In most cases, rainfall is uneven, especially over mountainous areas (*Barry,* 1984). Natural meteorological phenomena associated with precipitation are characterized by significant variability and discreteness in space and time, which complicates their study (*Babychenko,* 1991; *Lipinskyi et al.,* 2006; *Lohvynov et al.,* 1972,1973; *Sakaly,* 1985).

The distribution of precipitation can be extremely uneven both during the year and during one season. This also applies to heavy and extreme snowfalls, of which there may be several cases in one year and dozens in another. At the same time, their intensity, duration, and area of precipitation vary greatly, which complicates weather forecasting and leads to disruptions of various sectors of the national economy and infrastructure (*Acar* and *Gönençgil,* 2019; *Lukić et al.,* 2018; *Balabukh,* 2013; *Osadchyy* and *Babychenko,* 2012). All over the world and in Ukraine in particular, the frequency of extreme weather events is increasing, among which heavy and extreme precipitation takes the first place (*Balabukh,* 2008; *Lohvynov et al.,* 1972; *Osadchyy* and *Babychenko,* 2012; *Pachaury* and *Mayer,* 2014). That is why scientists raise the issue of long-term dynamics of precipitation, especially in conditions of climate change and increasing frequency of weather anomalies. The policy of governments on climate change has been ratified by many documents at national and international levels (*Tykhomyrova,* 2018).

Insufficient attention has always been paid to the study of heavy and extreme snowfalls, especially in the Ukrainian Carpathians. The main interest of scientists was limited to heavy and extreme rains, heavy and extreme prolonged rains, as well as heavy and extraordinary showers (*Balabukh,* 2008; *Voloshyna* and *Knysh,* 2010; *Pyasetska,* 2001; *Lukić et al.,* 2018). The risks and dangers of heavy and extreme snowfalls are significantly underestimated. First of all, such snowfalls are the causes of avalanches and traffic jams. During intensive falling sleet, it often sticks to various surrounding objects, breaking tree branches, breaking power and communication wires, disrupting constructions and utilities. Late snowfalls make it impossible to carry out spring agricultural work *(Lipinskyy et al.,* 2006; *Lohvynov et al.,* 1973; *Sakaly,* 1985).

The purpose of this work was to analyze the long-term changes in the number, intensity and spatial distribution of heavy and extreme snowfalls in the Transcarpathian region.

2. Materials and methods

2.1. Research area

The Transcarpathian region is located in the extreme west of Ukraine. It borders on Lviv and Ivano-Frankivsk regions, as well as four European Union countries: Poland, Slovakia, Hungary, and Romania. The area of the region is 12.8 thousand km^2 (2.1% of the territory of Ukraine). Thus, the Transcarpathian region is located in Central Europe, which has important cross-border significance (*Rishko,* 2017).

The Transcarpathian region is a unique ecological system of western Ukraine with a variety of relief and climatic conditions due to the vertical clarity and diversity of landscapes. Its territory is protected from the north and east by the Ukrainian Carpathians, from the northwest by the Tatra Mountains, from the south by the western Romanian mountains and the Maramureş massif *(Rishko,* 2017; *Sakaly,* 1985; *Lohvynov et al.,* 1973).

About two thirds of the territory of Transcarpathia is occupied by mountains with the highest peak of Ukraine (Hoverla, 2061 meters above sea level). The region is located on the southwestern slopes of the Ukrainian Carpathians (Eastern Carpathians) and on the adjacent Transcarpathian lowlands, which are part of the Middle Danube lowlands (*Herenchuk,* 1981).

The climate of Transcarpathia is temperate-continental with sufficient and excessive humidity, unstable spring, not very hot summer, warm autumn, and mild winter. The average annual wind speed in different places is 1.2–2.4 m/s. The maximum speed, registered in the area of the cities of Khust and Mizhhirya and in the mountain meadows, reaches about 40 m/s. In January, the average monthly long-term temperature is -7.8 °C in the mountains, while in the lowlands (Uzhhorod) it is only -3.1 °C, and in summer it is 11–14 °C in the highlands and 20–21 °C in the lowlands. The amount of precipitation changes depending on the height of the territory. The average annual rainfall is 600–800 mm in the lowlands, and 1000–1500 mm in the mountains (in a year of high water content it is up to 2500 mm) *(Babychenko* and *Dyachuk,* 2003; *Sakaly,* 1985).

Fig. 1 shows a map of the research area with the geographical location of the observation points of the Ukrainian Hydrometeorological Center, from which data were collected on heavy and extreme snowfall for this work.

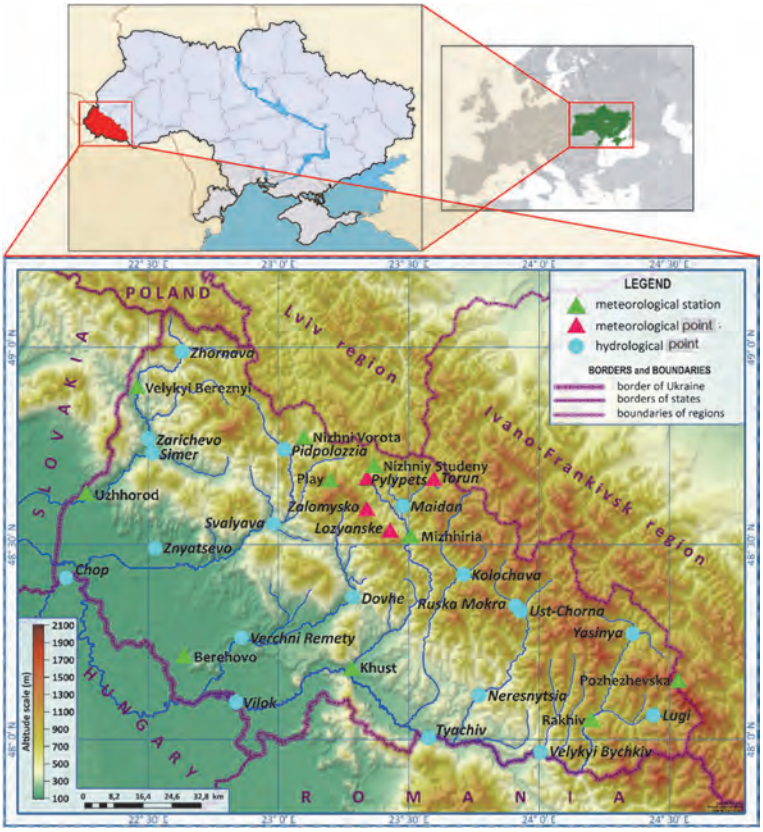

Fig. 1. Geographical location of hydrometeorological observation point involved in the research.

2.2. Data and methods

We used data only from those points that conducted continuous meteorological observations of precipitation during 1990–2019 to ensure temporal representativeness. In total, data from 10 meteorological stations, 4 meteorological points and 19 hydrological observation points are included in the work (*Table 1*).

According to the methodological guidelines of the Central Geophysical Observatory named after Borys Sreznevskyi (CGO) and the Ukrainian Hydrometeorological Center (UkrHMC) a clear criteria is defined for heavy and extreme snowfall (*Table 2*) (*Humonenko et al.*, 2019).

Table 1. Lists of points of hydrometeorological observations

Name	Latitude (north)	Longitude (east)	Altitude (m)
1. MS Berehovo	48°13′02′′	22°38′12′′	112
2. MS Uzhhorod	48°37′58′′	22°15′39′′	115
3. MS Khust	48°11′07′′	23°16′49′′	166
4. MS Velykyi Bereznyi	48°54′05′′	22°27′19′′	209
5. MS Rachiv	48°03′08′′	24°12′00′′	438
6. MS Mizhhiria	48°31′26′′	23°30′23′′	456
7. MS Nizhni Vorota	48°46′30′′	23°05′49′′	500
8. MS Nizhniy Studeny	48°42′10′′	23°22′01′′	615
9. MS Play	48°39′59′′	23°11′49′′	1330
10. MS Pozhezhevska	48°09′14′′	24°32′03′′	1439
11. MP Zalomysko	48°37′01′′	23°20′10′′	785
12. MP Lozyanske	48°32′49′′	23°25′34′′	572
13. MP Pylypets	48°39′45′′	23°19′20′′	618
14. MP Torun	48°40′23′′	23°35′07′′	827
15. GP Velykyi Bychkiv	47°58′03′′	24°00′22′′	295
16. GP Verchni Remety	48°15′44′′	22°51′30′′	118
17. GP Vilok	48°05′47′′	22°50′13′′	114
18. GP Dovhe	48°22′00′′	23°17′08′′	172
19. GP Zhornava	48°59′22′′	22°37′45′′	334
20. GP Zarichevo	48°46′13′′	22°29′57′′	154
21. GP Znyatsevo	48°29′28′′	22°31′03′′	108
22. GP Kolochava	48°25′26′′	23°42′34′′	567
23. GP Lugi	48°03′47′′	24°26′15′′	632
24. GP Maidan	48°36′50′′	23°27′50′′	503
25. GP Neresnytsia	48°06′51′′	23°46′09′′	299
26. GP Pidpolozzia	48°44′35′′	23°01′15′′	362
27. GP Ruska Mokra	48°20′39′′	23°54′33′′	563
28. GP Svalyava	48°33′11′′	22°58′49′′	193
29. GP Simer	48°44′03′′	22°30′53′′	152
30. GP Tyachiv	48°00′17′′	23°34′33′′	211
31. GP Ust-Chorna	48°19′49′′	23°55′39′′	529
32. GP Chop	48°24′56′′	22°11′04′′	101
33. GP Yasinya	48°16′21′′	24°21′31′′	650

Note: MS – meteorological station, MP – meteorological point, GP – hydrological point

Natural meteorological phenomena of the II level of danger (NMP II) are natural phenomena that in terms of quantitative indicators, duration, and territory of threat, pose a threat to the population and disrupt the functioning of the economic complex of the country (*Humonenko et al.*, 2019).

Natural meteorological phenomena of the III level of danger (NMP III) are natural phenomena that, according to quantitative indicators, duration, and area of distribution, pose a threat to human life in large areas, lead to large-scale damage to the country's economic complex (*Humonenko et al.*, 2019).

Only those cases of snowfalls were taken into account, which in quantitative and temporal characteristics reached the corresponding values specified in *Table 2.*

Table 2. Criteria for heavy and extreme snowfalls approved by CGO and UkrHMC from January 1, 2019

Phenomenon	**Criterion of the natural phenomenon of the II level of danger (NMP)**		**Phenomenon**	**Criterion of the natural phenomenon of the III level of danger (NMP)**	
	quantitative indicator	**duration**		**quantitative indicator**	**duration**
heavy snowfall	20-29 mm	≤12 hours	extreme snowfall	≥30 mm	≤12 hours

Data on heavy and extreme snowfalls were obtained by sampling from various sources of information, thus multiple verifications were performed. The basis of the database was the monthly «Tables of meteorological and agrometeorological observations», which are compiled by all meteorological stations. For meteorological and hydrological points, the information was obtained from the monthly «Tables of meteorological observations», and if they were not available, then from the «Books for recording hydrological observations». The information was also supplemented from the annual «Weather review and natural hydrometeorological phenomena on the territory of Ukraine», from the database METEOBASE developed by UkrHMC, and from «Reports on natural hydrometeorological phenomena» obtained directly from meteorological stations. The single program of meteorological observations of precipitation at stations and observation points made it possible to unify and combine data for research.

Statistical data processing, reliability assessment of the used series of observations, and accuracy testing of the obtained quantity were performed using

the methods of mathematical statistics *(Battalov*, 1968; *Dubrovskaya* and *Knyazev*, 2011; *Kobysheva* and *Narovlyanskyy*, 1978; *Shkolnyy et al.*, 1999).

The calculation of arithmetic mean (perennial) values ($\overline{x}$) was performed by the formula:

$$\overline{x} = \frac{\sum x_i}{n}, \quad (1)$$

where x_i are the individual values of the researched feature, n is the the number of years, cases or observations.

To characterize the variability of heavy and extreme snowfalls, the standard deviations of individual values (σ) from the long-term average, as well as the coefficients of variability (variation) (C_v) were calculated by the formulas:

$$\sigma = \sqrt{\frac{\sum(x_i - \overline{x})^2}{n}}, \quad (2)$$

$$C_v = \frac{\sigma}{\overline{x}}. \quad (3)$$

All mathematical calculations of indicators were performed in Microsoft Excel 2016.

Mapping of data on heavy and extreme snowfalls was carried out using the software package for cartographic modeling Surfer 15, and the isoline method was used. Interpolation was performed by the kriging method, as the one that most accurately uses statistical parameters to find the optimal estimate in terms of minimum mean deviation when constructing surfaces, cubes, and maps (*Abdullin* and *Shikhov*, 2017; *Katsalova* and *Shpyh*, 2013; *Mkrtchyan* and *Schuber*, 2013). All cartographic materials are created in an equilateral cylindrical projection of the Mercator using a three-dimensional coordinate system WGS-84.

3. Results

During 1990–2019, 453 isolated cases of heavy and 125 cases of extreme snowfall were recorded in the research area. The long-term distribution of the number of heavy and extreme snowfalls is shown in *Fig. 2*.

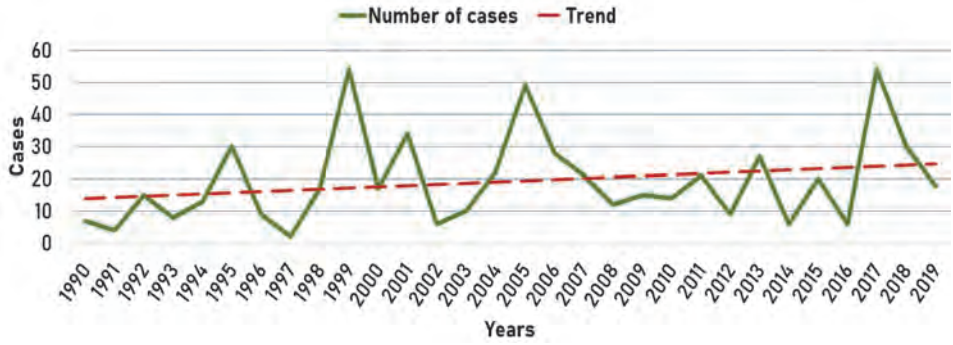

Fig. 2. Total number of cases of heavy and extreme snowfalls

As it can be seen from the graph (*Fig. 2*), the number of cases varies significantly from year to year. The most heavy and extreme snowfalls were recorded in 1999 and 2017 – 54 cases, and the least number was recorded in 1991 (4 cases) and 1997 (2 cases). In the first decade (1990–1999), 159 cases of heavy and extreme snowfalls were recorded, in the second (2000–2009) – 214 cases, and in the third (2010–2019) – 205 cases. The linear trend shows a tendency to increase the number of heavy and extreme snowfalls during the researched period, and therefore their recurrence and frequency increase. The same trends in climate change are observed globally (*Pachaury* and *Mayer*, 2014) and regionally (*Balabukh*, 2013). The average annual recurrence of heavy and extreme snowfalls happened in 19.3 cases, separately heavy snowfalls happened in 15.1 cases, emergency happened in 4.3 cases.

The average amount of precipitation that falls during one snowfall is of great practical importance. Calculations showed that for all cases of the studied snowfalls, an average of 26.6 mm of snow fell. The standard deviation was 7.7 mm, which indicates a fairly wide range of variation in precipitation during snowfalls. The coefficient of variation was 29%, which conditionally indicates the homogeneity of the sample and the rare recording of extraordinary snowfalls during which ≥50 mm of precipitation falls in ≤12 hours.

To calculate the climatic characteristics, the annual course of heavy and extreme snowfalls is important (*Fig. 3*).

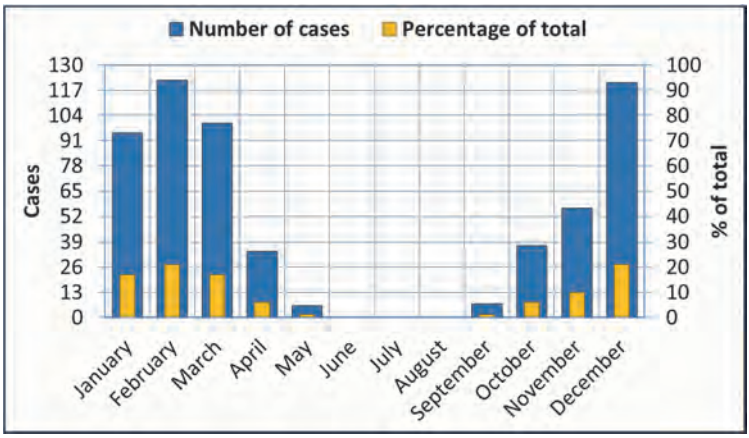

Fig. 3. Annual number of cases and their percentage of the total number of heavy and extreme snowfalls.

Analysis of the diagram (*Fig. 3*) shows that heavy and extreme snowfall fell during all seasons, except summer. Most of them were in winter: December – 121 (20.9%), January – 95 (16.5%), and February – 122 (21.1%) cases. A large number of snowfalls was recorded in March – 100 (17.3%) cases, which is due to the predominance of winter circulation this month. An interesting fact was that heavy snowfalls were observed even in May – 6 cases (1.0%) and September – 7 cases (1.2%), and during the warm period of the year (April-October), they were 14.5% of the total number of cases. The calculated average monthly distribution of cases is given in *Table 3*. Such distributions indicate the highest probability of heavy and extreme snowfalls in December and February, slightly lower in January and March, low in April, October, and November, and the lowest in May and September.

Table 3. The average monthly number of cases of heavy and extreme snowfalls

	Months											
	I	II	III	IV	V	VI	VII	VII	IX	X	XI	XII
Cases	3.2	4.1	3.3	1.1	0.2	-	-	-	0.2	1.2	1.9	4.0

The duration of snowfall is one of the most important characteristics. The process of snow accumulation and formation of snow cover height depends on it. During heavy snowfalls in the mountains of the Transcarpathian region, an increase in snow cover up to 50 cm can occur per day, which sharply increases the risk of avalanches (*Hryshchenko et al.*, 2013). The temporal dynamics of the duration of heavy and extreme snowfalls is given in *Table. 4*.

Table 4. Distribution of cases of heavy and extreme snowfalls of different duration

Duration											
to 1 hour	**1-2 hours**	**2-3 hours**	**3-4 hours**	**4-5 hours**	**5-6 hours**	**6-7 hours**	**7-8 hours**	**8-9 hours**	**9-10 hours**	**10-11 hours**	**11-12 hours**
Number of cases											
2	1	2	-	2	2	4	4	8	9	12	532

The uneven distribution of the duration of heavy and extreme snowfalls proves that in the territory of Transcarpathia, this natural meteorological phenomena are practically impossible to form, in a relatively short time interval (1–5 hours). However, the transience and discretion of snowfalls make it impossible to accurately record their duration, especially at night. Therefore, this conclusion is, to some extent, relative.

The spatial distribution of the researched snowfalls is of practical importance for the engineering design of buildings and structures, and other needs of various sectors of the national economy. For this purpose, the territory of Transcarpathia was mapped according to various indicators of distribution of heavy and extreme snowfalls. *Fig. 4* shows the general picture of the distribution of recurrence of heavy and extreme snowfalls during the researched period.

Fig. 4. Recurrence of heavy and constant snowfalls in Transcarpathia in the period of 1990–2019.

The map clearly distinguishes two zones of maximum recurrence: the territory of the mountain range Chornohora (snow avalanche station Pozhezhevska – 121 cases in 30 years) and the mountain range Borzhava (snow avalanche station Play – 62 cases in 30 years). Two more, less pronounced zones of significant recurrence are the upper left bank of the Teresva River basin (hydrological points Ust-Chorna – 34 cases and Ruska Mokra – 25 cases) and the catchment area of the Tysa and Rika rivers (meteorological station Khust – 31 cases).

The lowest recurrence is observed in the Transcarpathian lowland, which is part of the Middle Danube lowland (Uzhhorod aviation meteorological station – 3 cases, Beregovo meteorological station – 2 cases, and Chop hydrological point – 4 cases). Other zones of recurrence minima are the upper reaches of the Uzh River (Zhornava hydrological point – 1 case) and the estuaries of the Kosivska and Shopurka rivers (Velykyi Bychkiv hydrological point – 2 cases). In the rest of the territory, the recurrence rates, on average, vary from 10 to 20 cases over 30 years.

The next step was to map the quantitative indicators, i.e., the average and maximum values of precipitation during snowfall, recorded for each observation point (*Fig. 5*).

From *Fig. 5*(b) it is clear, that during one snowfall twice as much precipitation may fall as it is usually the case on average. In *Fig. 5* (a) the following zones of maximum precipitation values are distinguished: the upper parts of the Teresva, Terebli, and Rika river basins (Ruska Mokra hydrological point – 30.8 mm and meteorological points: Lozianske – 30.2 mm, Pylypets – 30.9 mm and Torun – 32.0 mm). It can be concluded that in these areas there are often extraordinary snowfalls, which are classified as natural meteorological phenomena of the highest III level of danger (*Table 2*). Areas of least risk of emergency snowfall are the right part of the Uzh River basin, the Verkhnyotysianska basin and the southern part of the Transcarpathian lowland.

Regarding the maximum amount of precipitation during snowfall (*Fig. 5* (b)), the distribution is slightly different. There are two distinct zones of maximum precipitation: the Borzhava mountain range and the upper reaches of the Teresva River. During the researched period, a record amount of precipitation during an extreme snowfall was recorded at the avalanche station Play (Borzhava ridge) on the night of January 18–19, 2007 – 71.3 mm/7 hours 10 min. Another zone of maximum precipitation is the ridge of Chornohora in the eastern part of Transcarpathia (avalanche station Pozhezhevska – March 4–5, 2001 54.3 mm/12 hours). Areas where extreme snowfalls have never been recorded are the upper right part of the Uzh River basin, the southwestern part of the Transcarpathian lowland, and the eastern half of the Verkhnotysianska basin.

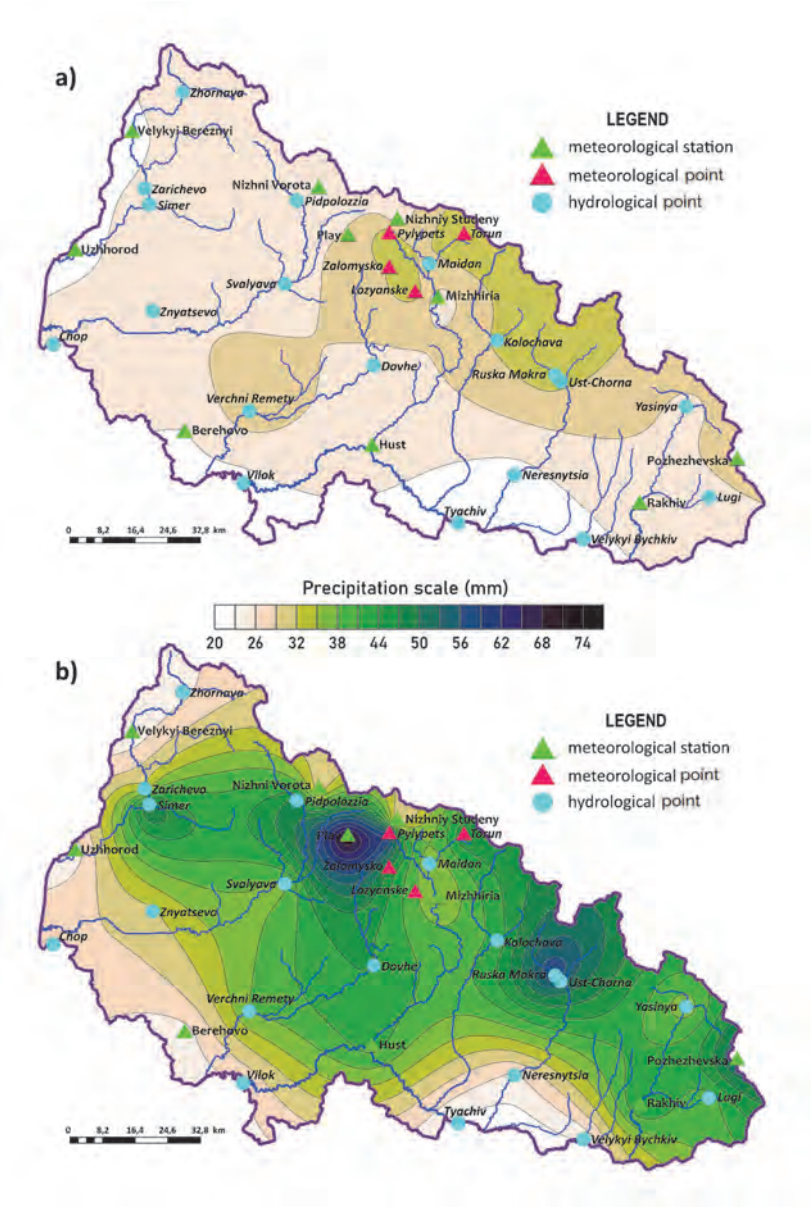

Fig. 5. Average annual (a) and maximum (b) precipitation of heavy and extreme snowfalls in Transcarpathia in the period of 1990–2019.

4. Conclusions

1. A positive trend in the number of heavy and extreme snowfalls in the Transcarpathian region for the period 1990–2019 has been identified. It is possible that in the future we should expect an increase in the number of cases of heavy and extreme snowfalls.
2. The average annual recurrence of heavy and extreme snowfalls during 1990-2019 was determined — 19.3 cases, i.e., on average, about 19 local cases of heavy and extreme snowfalls were observed in the Transcarpatian region a year.
3. When compiling the review of weather-forming processes, it is recommended to take into account the features of the annual course of the formation of heavy and extreme snowfalls, which has a maximum in February and December.
4. Over Transcarpathia, heavy and extreme snowfalls most often (92%) last 11-12 hours, falling 50 mm of snow in a shorter time interval is less likely.
5. The areas of the greatest natural load by heavy and extreme snowfalls due to mapping of the territory of the Transcarpathian region are selected – these are the territory of the Borzhava mountain range, the upper reaches of the Teresva River, and the Chornohora mountain range.
6. It is established, that the greatest recurrence of heavy and extreme snowfalls was observed in the mountainous part of the Transcarpathian region (on average 15–25 cases per year). The maximum amount of precipitation in the mountains during snowfalls varies between 25–35 mm. Extreme snowfalls, during which ≥50 mm of precipitation falls in ≤12 h, are a rare natural meteorological phenomenon.

For a more detailed study of heavy and extreme snowfalls as natural meteorological phenomena in the Transcarpathian region, it is advisable to conduct cluster analysis, and regression and correlation analyzes of their relationship with orography.

References

Abdullin, R.K. and *Shikhov, A.N.*, 2017: Sinteticheskoye kartografirovaniye opasnykh meteorologicheskikh yavleniy na regionalnom urovne. *Geodeziya i Kartografiya 78*, 31–40. (In Russian)

Acar, Z. and *Gönençgil, B.*, 2019: Extreme precipitation events in Turkey. *Meteorologický časopis 22*, 87–94.

Babychenko, V.M. and *Dyachuk, V.A.*, 2003: Klimat Ukrayiny. UkrNDHMI, Kyyiv. (In Ukrainian)

Babychenko, V.N., 1991: Stykhyynye meteorolohycheskye yavlenyya na Ukraine i v Moldavyi. Hydrometeoyzdat, Lenynhrad. (In Russian)

Balabukh, V.O., 2008: Minlyvist duzhe sylnykh doshchiv i sylnykh zlyv v Ukrayini. *Naukovi pratsi UkrNDHMI 257*, 61–72. (In Ukrainian)

Balabukh, V.O., 2013: Rehionalni proyavy hlobalnoyi zminy klimatu v Zakarpatskiy oblasti. *Ukrayinskyy hidrometeorolohichnyy zhurnal 13*, 55–62. (In Ukrainian)
Barry, R.H., 1984: Pohoda y klymat v horakh. Hydrometeoyzdat, Lenynhrad. (In Russian)
Battalov, F.Z., 1968: Mnoholetnye kolebanyya atmosfernykh osadkov y vychyslenye norm osadkov. Hydrometeoyzdat, Lenynhrad. (In Russian)
Dubrovskaya, L.Y. and *Knyazev, H.B.*, 2011: Kompyuternaya obrabotka estestvenno-nauchnykh dannykh metodamy mnohomernoy prykladnoy statystyky. TML-Press, Tomsk. (In Russian)
Herenchuk K.I., 1981: Pryroda Zakarpatskoyi oblasti. Vyshcha shkola, Lviv. (In Ukrainian)
Hryshchenko V.F., Aksyuk O.M., and *Honcharenko H.A.*, 2013: Dovidnyk zi snihovoho pokryvu v horakh Ukrayiny (Karpaty, Krym). UkrNDHMI, Kyyiv. (In Ukrainian)
Humonenko, L.V., Zhuk, N.H., Savchenko, L.I., Tkach, L.V., and *Filonenko, V.O.*, 2019: Nastanova z meteorolohichnoho prohnozuvannya. UkrHMTS, Kyyiv. (In Ukrainian)
Katsalova, L.M. and *Shpyh, V.M.*, 2013: Krihinh-interpolyatsiya v zadachakh prohnozu pohody. *Naukovi pratsi UkrNDHMI 264*, 3–9. (In Ukrainian)
Kobysheva, N.V., Narovlyanskyy, H.YA., 1978: Klymatolohycheskaya obrabotka meteorolohycheskoy ynformatsyy. Hydrometeoyzdat, Lenynhrad. (In Russian)
Lipinskyy, V.M., Osadchyy, V.I., and *Babychenko, V.M.*, 2006: Stykhiyni meteorolohichni yavyshcha na terytoriyi Ukrayiny za ostannye dvadtsyatyrichchya (1986-2005 rr.*)*. Nika-Tsentr, Kyyiv. (In Ukrainian)
Lohvynov, K.T., Babychenko, V.N., and *Kulakovskaya, M.YU.*, 1972: Opasnye yavlenyya pohody na Ukrayne. Hydrometeoyzdat, Lenynhrad. (In Russian)
Lohvynov, K.T., Raevskyy, A.N., and *Ayzenberh, M.M.*, 1973: Opasnye hydrometeorolohycheskye yavlenyya v Ukraynskykh Karpatakh. Hydrometeoyzdat, Lenynhrad. (In Russian)
Lukić, T., Basarin, B., Micić, T., Bjelajac, D., Maris, T., Marković, S.B., Pavić, D., Gavrilov, M.B., and *Mesaroš, M.*, 2018: Rainfall erosivity and extreme precipitation in the Netherlands. *Időjárás 122*, 409–432. https://doi.org/10.28974/idojaras.2018.4.4
Mkrtchyan, O.S. and *Shuber, P.M.*, 2013: Interpolyatsiya danykh meteosposterezhen′ kil′kostey opadiv ta inshykh klimatychnykh zminnykh metodom rehresiynoho krygingu. *Visnyk Lvivskoho universytetu. Seriya heohrafichna 42*, 258–264. (In Ukrainian)
Osadchyy, V.I. and *Babychenko, V.M.*, 2012: Dynamika stykhiynykh meteorolohichnykh yavyshch v Ukrayini. *Ukrayinskyy heohrafichnyy zhurnal 4*, 8-14. (In Ukrainian)
Pachaury, R.K. and *Mayer, L.A.*, 2014: Yzmenenye klymata: Obobshchayushchyy doklad. Vklad Rabochykh hrupp I, II y III v Pyatyy otsenochnyy doklad Mezhpravytelstvennoy hruppy ekspertov po yzmenenyyu klymata. MHEYK, Zheneva. (In Russian)
Popov, T., Gnjato, S., and *Trbić, G.*, 2018: Analysis of extreme precipitation over the Peripannonian region of Bosnia Hercegovina. *Időjárás 122*, 433–452. https://doi.org/10.28974/idojaras.2018.4.5
Pyasetska, S.I., 2001: Chyslo dniv iz sylnymy opadamy v pivdenno-zakhidniy chastyni Krymskykh hir. *Naukovi pratsi UkrNDHMI 249*, 73–81. (In Ukrainian)
Radzka. E. and *Rymuza. K.*, 2020: Statistical and geostatistical analysis of spatial variation of precipitation periodicity in the growing season. *Időjárás 124*, 129–141. https://doi.org/10.28974/idojaras.2020.1.7
Rishko, S.V., 2017: Dopovid pro stan navkolyshnoho pryrodnoho seredovyshcha Zakarpatskoyi oblasti za 2016 rik. Departament ekolohiyi ta pryrodnykh resursiv Zakarpatskoyi ODA, Uzhhorod. (In Ukrainian)
Sakaly, L.Y., 1985: Teplovoy y vodnyy rezhym Ukraynskykh Karpat. Hydrometeoyzdat, Lenynhrad. (In Russian)
Shkolnyy, YE.P., Loyeva, I.D., and *Honcharova, L.D.*, 1999: Obrobka ta analiz hidrometeorolohichnoyi informatsiyi. Odeskyy hidrometeorolohichnyy instytut, Odesa. (In Ukrainian)
Tykhomyrova, YE.B., 2018: Zmina klimatu yak skladova mizhnarodnykh prohram bezpeky. *Visnyk Lvivskoho universytetu. Seriya mizhnarodni vidnosyny 44*, 22–31. (In Ukrainian)
Voloshyna, O.V. and *Knysh, I.F.*, 2010: Statystychne doslidzhennya vypadkiv duzhe sylnykh doshchiv na terytoriyi Zakhidnoyi Ukrayiny. *Ukrayinskyy hidrometeorolohichnyy zhurnal 6*, 102–108. (In Ukrainian)

DOI:10.28974/idojaras.2021.3.8

IDŐJÁRÁS

Quarterly Journal of the Hungarian Meteorological Service
Vol. 125, No. 3, July – September, 2021, pp. 491–511

Downscaling diurnal temperature over west and southwest Iran: A comparison of statistical downscaling approaches

Mohammad Reza Poodineh

Department of Physical Geography
University of Sistan and Baluchestan, Zahedan, Iran
mrpoodineh@yahoo.com

(Manuscript received in final form September 10, 2020)

Abstract— This study aimed to forecast temperature variations in the western and southwestern part of Iran using a general circulation model and artificial neural networks (ANN). The data included mean diurnal temperatures from synoptic stations, National Centers for Environmental Prediction/ National Center for Atmospheric Research (NCEP/NCAR) reanalysis data, and outputs of a third-generation global climate model, the Hadley Centre Coupled Model version 3 (HadCM3), under A2 and B2 scenarios for the baseline period (1961–1990). The data of the first (1961–1975) and second 15 years (1976–1990) of the baseline period were used for model calibration and validation, respectively. Both models, however, produced reliable estimates at the plain stations with neither outperforming the other due to their negligible errors. However, the neural network results of mountain synoptic stations showed a lower error rate than the statistical downscaling model (SDSM) outputs. All in all, we can say that there was a larger amount of error in the outputs of the atmospheric general circulation models (AGCMs) in the mountainous regions. According to the outputs of the neural network and the AGCMs, temperatures at the studied stations were on the rise. In fact, this increase was more noticeable at the plain stations. This can be attributed to their proximity to the sea, to their latitude, and to the more intensive industrial activities (especially, extraction of petroleum and production of petroleum products) taking place near the plain stations.

Key-words: diurnal temperature, AGCMs, SDSM, HadCM3

1. Introduction

A general circulation model (GCM) indicates whether increasing concentrations of greenhouse gases will have considerable climate outcomes on global and regional scales. It is still debatable how much increasing greenhouse gases will

affect meteorological processes; however, it is evident that increased concentrations of greenhouse gases have directly and indirectly affected climatic elements both spatially and temporally (*Smith et al.*, 2010). Sea level rise and changes in temperature threshold and rainfall are among the outcomes of climate change. Changes in precipitation distribution patterns and the 1 °C change in the temperature of the water resources of a region are some of the other events resulting from climate change. Long-term forecasts of climate variables to be aware of the extent of variations, and hence, to take necessary actions to alleviate the adverse effects of climate change have attracted the specialists in climatology and agriculture, and even in social sciences and economics (*Maraun et al*, 2015). More frequent heat waves can be pointed out as the direct effects, while the increased heat island intensity and the decrease in boundary layer height as indirect outcomes of the climate change. Evaluation of climate change with the help of AGCMs has attracted in Iran and abroad in the past 10 years. Only a few of such evaluations are mentioned here to save space. For instance, Harpham and Wilby conducted a study in England by using different models such as the outputs of the HadCM3 model, a radial basis function network, and a multi-layer perceptron artificial neutral network (MLP) ANN to predict precipitation for different regions. The results showed that each of those methods was able to forecast precipitation, although they had different capabilities in different regions. In fact, the (MLP) ANN yielded better results (*Harpham* and *Wilby*, 2005). In another study, *Meshkati et al.* (2010) analyzed and evaluated the least-angle regression (LARS) model in simulating the meteorological data in Golestan Province. Their results indicated that the performance of LARS in modeling the meteorological variables of the surveyed stations was generally acceptable and could be employed to reconstruct the data of the stations for past periods. In the same relation, *Ababaei et al.* (2011) used downscaling the data of the AGCM to evaluate climate change in Iran for 2010–2039.

GCMs can never be used directly for regional or local predictions. They require downscaling to improve their predictions on local scales by applying local behaviors. All of these operations are known as downscaling, which is a term used to describe the process related to data for evaluating the effects of climate change at temporal or spatial scales (*Ashraf*, 2011a, 2011b). Nevertheless, the results of a study conducted on GCMs show increased concentrations of greenhouse gases that have considerable outcomes for climate on global and regional scales at different temporal and spatial scales (*Sahai et al*, 2003). Prediction of future weather conditions and their outcomes for regional hydrology are very important in identifying appropriate strategies for reducing the effects of climate change and adapting to weather conditions (*Kug et al.*, 2008). GCMs are troublesome in studies on the effects of climate change due to lack of accurate regional data. Therefore, to determine climate change in the western and southwestern parts of Iran, the SDSM and a neural network were employed to predict temperature changes.

Samadi et al. (2013) reviewed the statistical downscaling of river runoff in a semi-arid catchment. According to the SDSM and ANN projections, daily temperature will increase up to +0.58 °C (+3.90%) and +0.48 °C (+3.48%), and daily precipitation will decrease up to −0.1 mm (−2.56%) and −0.4 mm (−2.82%), respectively. The results suggest a significant reduction of stream flow in both downscaling projections, particularly in winter. The discussion considers the performance of each statistical method for downscaling future flow at catchment scale as well as the relationship between atmospheric processes and flow variability and changes.

Dorji et al. (2017) reviewed the statistical downscaling of river runoff in a semi-arid catchment using a statistical downscaling model (SDSM) and a time delay neutral network (TDNN). The results from this study will augment other investigation and research for improving the prediction of rainfall. IPCC AR5 reports gaps in understanding the climate impacts on precipitation at the catchment scales. Further work to downscale variability and extreme indices are important for impact studies. Within the stated limitations, the results of the reviewed study provide daily values of temperature and rainfall for applications, like driving a hydrology model for the Colombo area. It also provides a scientific guideline for impact assessment studies, framing policies and long-term adaptation planning. The projected annual increase for the representative concentration pathway (RCP) is 8.5; the average temperature is 2.83 °C (SDSM) and 3.03 °C (TDNN), and the rainfall is 33% (SDSM) and 63% (TDNN) for the 2080s.

2. Data and methodology

This study aimed to compare and simulate temperatures of the western and southwestern parts of Iran by using a neural network and downscaling of AGCMs. The research data included mean diurnal temperatures from synoptic stations in plain (Ahwaz, Abadan, and Dezful) and mountainous regions (Shahr-e Kord, Khorramabad, and Hamadan), NCEP analysis data, and outputs of HadCM3 third-generation global climate model under A2 and B2 scenarios for the baseline period (1961–1990). The temperatures for three periods (2010–2039, 2040–2069, and 2070–2099) were predicted and compared with those of the baseline period. The data of the first 15 years (1961–1975) and those of the second 15 years (1976–1990) of the baseline period were used for model calibration and validation, respectively. *Fig. 1* shows the distribution of the studied stations.

GCMs can never be used directly for regional or local predictions, because they need downscaling to improve their predictions on local scales by applying local behaviors. Therefore, the data should be downscaled before they are used. The Hadley Coupled Atmosphere-Ocean General Circulation Model (HadCM3) is a coupled atmospheric-ocean general circulation model (AOGCM) designed

and developed at the Met Office Hadley Center for Climate Change in England. This model, which was described by *Pope et al.* (2000), consists of an atmospheric component named HadAM3 and an ocean component named HadOM3, which has a sea ice component. HadAM3 has a horizontal resolution of 2.5° × 3.75° latitude × longitude), 96 × 73 grid points on the scalar grid on the entire planet Earth. Its spectral resolution is T42, which corresponds to a horizontal grid spacing with the dimensions of 417 km × 78 km (at the equator).

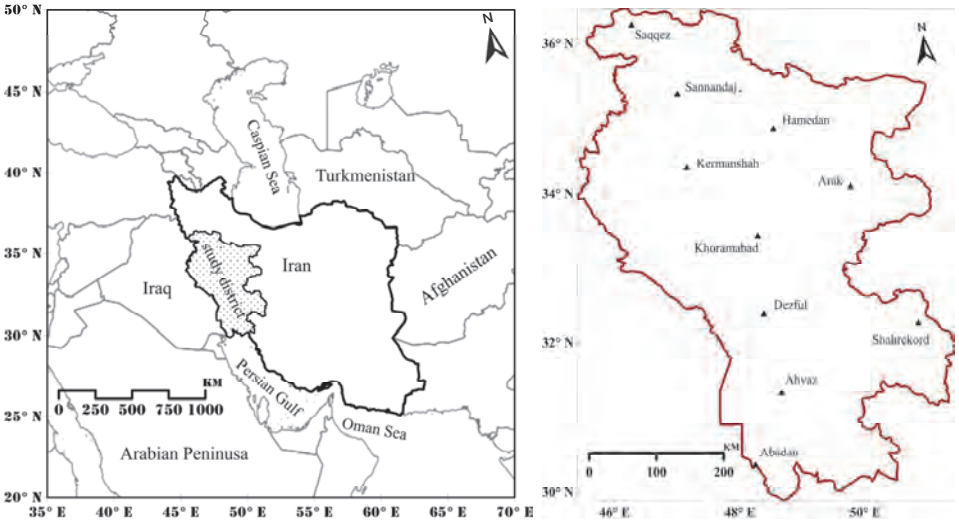

Fig. 1. Key map of study area (left) and spatial distribution of the weather stations (right).

The ocean model (HadOM3) has 20 levels with a resolution of 1.5˚×1.5˚. The high resolution power of the ocean component is the most important advantage of this model (*Pope et al.*, 2000). HadOM3 has a resolution of 1.25 × 1.25 degrees and 20 levels. The high resolution of HadOM3 is the most important advantage of this model (*Pope et al.*, 2000). Climate scenarios use the data from emission scenarios for future predictions. In simpler terms, climate scenarios are the outputs of dynamical models for climate change in future decades. Downscaling refers actually to the process of moving from large-scale predictors towards observed local scale predictions. After verification, these equations can be used in downscaling future predictions through employing emission scenarios (here, A2a and B2a scenarios). Climate scenarios use the data from emission scenarios to predict the future. Put more simply, climate scenarios are the outputs of statistical climate models for future decades. In this study, data

quality had to be controlled first for downscaling. The results indicated that the best way of using the simulation data was to use the raw data (without data transformation). The independent variables that were able to make a good estimate of the actual data were selected to estimate the temperature. Some of the independent variables had an average correlation but did not make an accurate estimate of the actual data when they were entered into the model, and hence they were omitted. However, as the model was an AGCM, and this kind of model is based on the assumption that climate change is influenced both by local and macro factors on the scale of the atmosphere, it was attempted to include more independent variables as long as the computational error was smaller than 0.05. Some variables, such as special humidity, zonal component, and meridian component sometimes had fairly good correlation, but greatly increased the estimation error when they were entered into the model. Therefore, such variables were not included in the model to evaluate temperature variations at the studied stations. In this stage, in addition to the mentioned items, special attention was paid to the degree of overlap (collinearity or variance inflation factor (VIF)) between the independent variables and the dependent variable (the temperature of interest). After the independent variables were selected at each station to estimate the temperature, the degree of overlap between the independent variables and the dependent variable was calculated for each station and taken into account to estimate the changes in temperature. The following method was used to calculate the degree of overlap between temperature and each of the predictor variables (*Pan* and *Jackson*, 2008):

$$VIF = \frac{1}{1-r^2}, \tag{1}$$

where *VIF* is the variance inflation factor and r^2 is the coefficient of determination.

Moreover, the entire process of controlling data and evaluating variables in each step was performed outside the SDSM to better control the prediction process. Therefore, all of these steps were performed in MATLAB using programming possibilities before the prediction process was carried out to have full control over the trend in data. The entire process of controlling the data and evaluating the variables is an other item that must be paid attention to in statistical downscaling. For this purpose, the number of ensemble effects was selected by considering descriptive characteristics, probability distributions, and differentiation test and fluctuation analysis. Hence, these steps were trained by increasing and decreasing the ensemble effects through considering the independent variables, the *VIF*, and the bias rate under evaluation to obtain the best results.

An artificial neural network (ANN) was used to study and compare the variations in estimates through SDSM. An ANN is a computational method that tries to present a mapping from the input space (the input layer) to the desired

space (the output layer) by identifying the intrinsic relationships between the data with the help of the learning process and through utilization of processors called neurons. The hidden layer(s) process the information received from the input layer and send it to the output layer. Each network is trained by receiving examples. Training is a process that eventually results in learning. Network learning takes place when communication weights between the layers change so much that there is an acceptable difference between the predicted and calculated values. When this happens, the learning process is completed. These weights express the network memory and knowledge. The larger the number of hidden layers is the more complicated the probability of network convergence will become. After selecting and analyzing the variables based on the A2a and B2a scenarios, temperatures of the southern and southwestern regions in Iran were predicted for up to 2099. However, most researchers believe that prediction results are reliable for up to one fourth of the statistical period. Therefore, this principle was taken into account in making predictions by using the neural network. Finally, the model was implemented for each of the studied stations, and a database with the dimension of 32040×10 was studied and analyzed for the future climate change for the statistical period 2011–2099. In the next stage, regression methods were utilized to study variations in the trend. Spectral analysis was used to study and analyze the fluctuations and cycles of temperature at the studied stations.

3. Results and discussion

The SDSM and a neural network were employed to study changes in temperature and to predict the future temperatures for the southern and southwestern parts of Iran. One of the most important steps in SDSM is the selection of dominant variables, because the independent variables directly influence the characteristics of the model and the results obtained from it (*Santer*, 1996). The SDSM evaluates the statistical relationships between the observed (or predicted) variables and the large-scale (or predictor) variables based on correlation and partial correlation. Five variables having the highest correlation (p-value = 0) with the observed data on temperature were selected from the 26 tested variables based on the coefficients of correlation between the observed data and the diurnal predictor variables using the SDSM software. *Table 1* shows the correlation coefficients of the variables. According to this table, compared to the other predictor variables, the average temperature at the stations in southwest Iran (Ahwaz, Dezful, Abadan, Shahrekord, Khorramabad, and Hamadan) had very significant correlations with the sea level pressure, the 500 hPa geopotential level, the relative humidity (%) at the 850-hPa level and close to ground surface and the average temperature at the 2 m height. Among the mentioned variables, the sea level pressure and the average 2 m height temperature had the most common diffraction surface with the mean temperatures at the southwestern stations. Pressure has an undeniable role in the

governing atmospheric situation and conditions in a region by affecting most of the climate variables (*Mohammadi*, 2014). Some researchers believe that pressure abnormalities have greater effects at higher latitudes than at lower latitudes (*Blasing*, 1981). This element is so effective that it is always analyzed as the first element in the identification and studies of climatic conditions of a region (*Broccoli* and *Harnack*, 1981). Nonetheless, the sea level pressure and its relationships with temperature differ both temporally and spatially. For instance, more temperature abnormalities in distribution are observed in tropical regions than in extratropical ones (*Whetton*, 1990).

Table 1. Results of evaluating the HadCM3 and neural network outcomes

			General Circulation Models				Neural Network	
		Parameter	orrelation	Partitional correlation	Mean square error	Ensemble effects	VIF	Weight MSE
Plain stations	Ahwaz	Seal level pressure	-0.837	-0.710	0.86	25	9	0.58 0.93
		Altitude of 500 hPa	0.837	0.661				
		Altitude of 850 hPa	-0.573	-0.456				
		Ground level relative humidity	-0.845	-0.419				
		Ground level average temperature	0.951	0.909				
	Abadan	Seal level pressure	-0.825	-0.611	0.91	30	8	0.61 0.58
		Altitude of 500 hPa	0.784	0.511				
		Altitude of 850 hPa	-0696	-0.523				
		Ground level relative humidity	-0.743	-0.341				
		Ground level average temperature	0.896	0.832				
	Dezful	Seal level pressure	-0.850	-0.260	1.1	20	10	0.36 0.65
		Altitude of 500 hPa	0.875	0.632				
		Altitude of 850 hPa	-0.814	-0.231				
		Ground level relative humidity	-0.852	-0.341				
		Ground level average temperature	0.961	0.360				

Continue *Table 1*. Results of evaluating the HadCM3 and neural network outcomes

			General Circulation Models				Neural Network	
Mountain stations	Shahrekord	Sea level pressure	-0.888	-0.410	0.96	30	7	0.654	1.73
		Altitude of 500 hPa	0.875	0.456					
		Altitude of 850 hPa	-0.812	-0.330					
		Ground level average temperature	0.960	0.354					
	Khorramabad	Seal level pressure	-0.858	-0.413	1.42	20	8	0.741	1.72
		Altitude of 500 hPa	0.872	0.411					
		Altitude of 850 hPa	-0.807	-0.312					
		Ground level relative humidity	-0.841	-0.461					
		Ground level average temperature	0.948	0.623					
	Hamadan	Seal level pressure	-0.789	-0.352	2.14	35	7	0.80	0.65
		Altitude of 500 hPa	0.874	0.412					
		Altitude of 850 hPa	-0.707	-0.248					
		Ground level relative humidity	-0.659	-0.514					
		Ground level average temperature	0.955	0.647					

Although results of the SDSM in estimating and predicting temperatures in some areas of the regions were acceptable, its accuracy was lower than that of the neural network in some other stations including those in Hamadan and Khorramabad. However, *Sahai et al.* (2010) obtained similar results in the analysis of weather variations in India. Despite these differences in SDSM results, in some stations such as Ahwaz, Dezful, and Abadan, both the neural network and HadCM3 yielded suitable results in predicting temperature. Therefore, as mentioned earlier, we can say that the error rates of both methods at some stations are not so considerable as to conclude definitely that the neural network produced better results. On the scale of global research, although most SDSM predictions exhibited lower accuracy than other methods (*Ojha*, 2010), it produces acceptable results compared to the neural network in some cases at different times and locations (*Chen et al.*, 2012; *Hassan et al.*, 2012).

Results of the analysis showed that the VIF values for the southern stations were 6–9%, indicating that these stations exhibited the lowest error rate. In downscaling, VIF is added to or deducted from the regression model to regulate the variance of diurnal weather variables (*Khan et al.*, 2006). Nevertheless, *Fiseha et al.* (2012) studied changes in extreme temperature profiles in the US using five predictor variables and reported VIF values ranging from 8 to 10%). However, some researchers believe that VIF values should take into account the trend and fluctuations in variables in addition to the extent of overlap with the predictor

variables in estimating the data for future (*McGuffie et al.*, 1999). For most stations, 20–35 ensemble effects produced more acceptable results so that the means, variances, and minimum and maximum values exhibited the least differences (*Figs. 2* and *3*). Many of the researchers obtained similar results in the downscaling of temperature prediction. According to some researchers, increasing ensemble effects have no significant impacts on the model results for some climate elements having very low coefficients of changes. In addition, identifying the spatial and temporal distribution of data has a key role in selecting the number of ensemble effects.

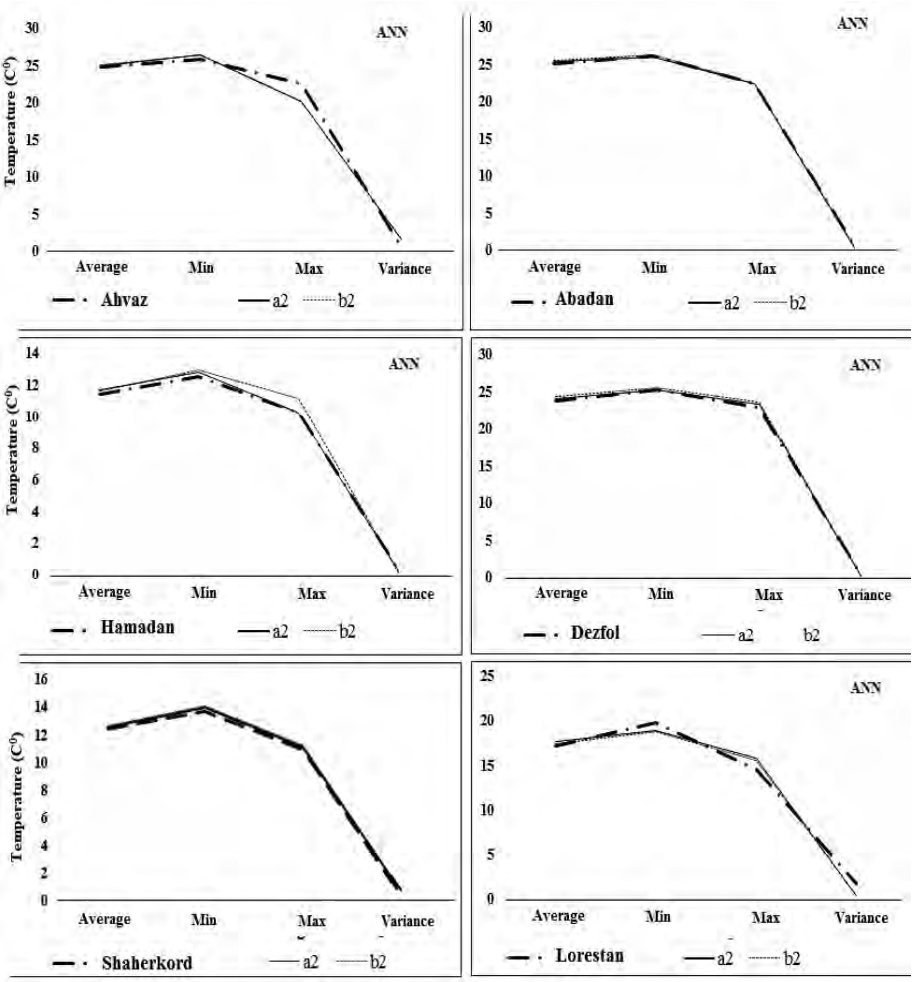

Fig. 2. Evaluation of the predicted changes in temperature based of the neural network for 1961–1990.

Regarding the evaluation of climate change, estimation of increases and decreases has a basic role in predicting future climate change. In fact, researchers pay close attention to the values of the minimums and maximums in selecting the superior models of climate change in addition to the general trend in climatic norms (*Chen et al.*, 2012). In this approach, the model is considered optimal if it can estimate the climatic trend well and produce acceptable results in predicting the fluctuations.

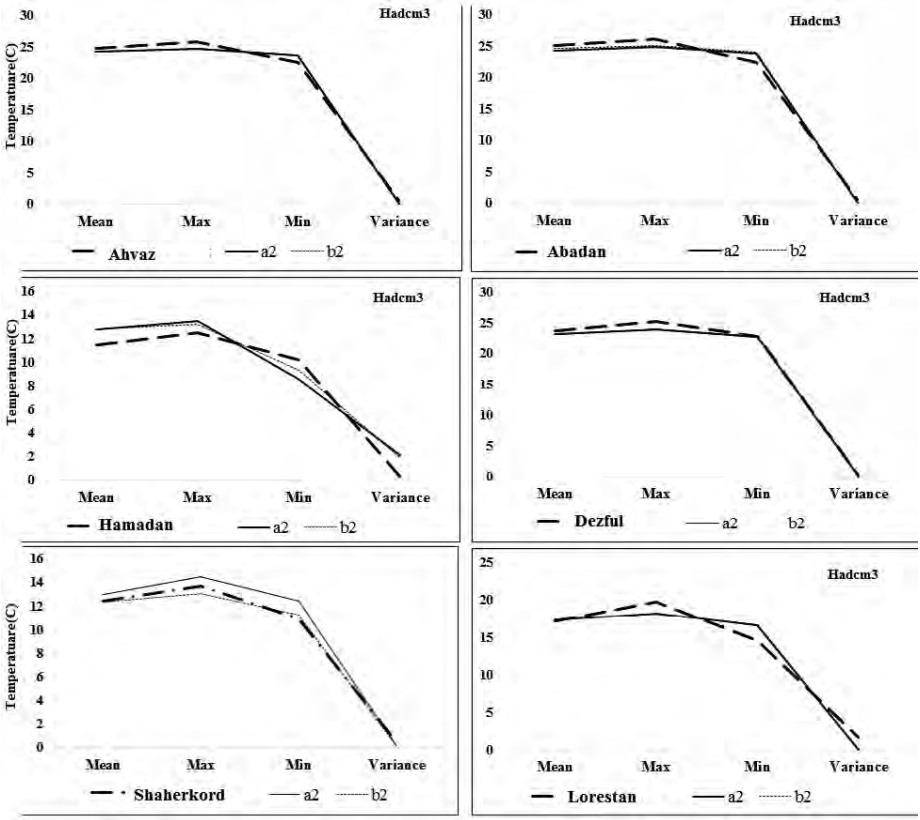

Fig. 3. Predicted mean variations based on the output of HadCM3 during 1961–1990 evaluating future temperature variations in the southwestern part of Iran.

Since the values of the minimums and maximums are very important in predicting climate elements (in other words, the time series), these values as well as the frequency distributions were determined in this research. According to the results, although the stations at Ahwaz, Abadan, and Dezful measured the target values well, the resultant amount of error in the output of the GCM for the mentioned stations does not allow us to say definitely that the neural network yielded acceptable

results. Therefore, the amounts of error at these stations were not statistically significant at a 95% confidence level in evaluating climate change. The conditions were slightly different at the other stations. For instance, the outputs of the HadCM3 model showed a better evaluation than the neural network in estimating temperature variations at the Shahrekord station. However, neural network outputs were more acceptable at the Shahrekord and Khorramabad stations. The reason for this superiority, as discussed earlier, is based on the principle that a model is more appropriate for predicting future change if it can express the observed temperature variations well.

Table 2 shows the spatial characteristics of temperature at the stations in southwest Iran based on the outputs of the downscaling of HadCM3 and the neural network for the A2a and B2a scenarios. In the first column of each index, spatial characteristics of the measured data are listed for comparison with the simulated data for the scenarios. According to this table, there were considerable increases in the average temperatures at the studied stations based on the HadCM3 and neural network outputs for the A2a and B2a scenarios. The outputs of the HadCM3 model for the A2a scenario show that the average temperature increased by 2.5 degrees at the plain stations (Abadan, Ahwaz, and Dezful) but, based on the B2a scenario, the temperatures at these stations increased by 2 degrees. Therefore, the increases and decreases in temperature for the A2a and B2a scenarios were much higher than the observed increases and decreases in temperature. Differences in the central indices indicate the diurnal increases and decreases in temperature. This can be backed by the closeness of the values for the mean and the median (50th percentile) and the low value of the mode in all of the research periods. However, the Khorramabad station showed higher diurnal decreases and increases than other stations so that temperature prediction at this station based on the neural network exhibits a similar situation. This can indicate that there will be more heat and cold waves in the future based on the outputs of the GCMs for the A2 and B2 scenarios. Accordingly, the descriptive characteristics of temperature for future years based on the neural network for the A2a and B2a scenarios exhibited increases of 1 and 1.5 °C, respectively. Nevertheless, unlike the AGCMs, the neural network outputs for the central indices (mean, median, and mode) are more consistent with the actual data. Therefore, we can infer that the mean temperature in the future will exhibit increases and decreases and display high spatial diversity. The high coefficients of change based on both methods show the high changeability of temperature in the studied stations. This may be due to the higher concentration of highlands in west Iran because of the effects of temperature modifiability at high altitudes. The skewness was positive for spatial characteristics but negative for the different scenarios. This indicates that the number of areas with averages higher than total mean of the region is larger than the number of areas with averages lower than the total mean of the region. The value of the diffraction (variance) shows how the observations are dispersed around the mean. It had its highest value, which was another confirmation of the increases and decreases in diurnal temperature in the future. The values obtained from analyzing the 25th, 50th, and 75th percentiles show that the temperature will experience larger values based on the A2a scenario.

Table 2. Spatial characteristics of temperature at the studied stations based on the A2a and B2a scenarios during 2015–2025

	Scenario		Abadan	Ahwaz	Dezful	Hamadan	Khorramabad	ShahreKord
Mean	Station		25.5	25.3	23.6	11.6	11.08	12.1
	Neural network	A2	26.4	26.1	24.4	12.5	17.9	13.0
		B2	26.1	25.8	24.1	12.2	17.6	12.7
	HADCM3	A2	27.8	28.6	27.6	13.7	19.7	14.9
		B2	27.1	27.8	26.8	13.6	19.1	14.9
Median	Station		25.4	25.3	24.0	11.7	17.2	11.9
	Neural network	A2	26.2	62.2	24.8	12.5	18.1	12.8
		B2	25.9	25.9	24.5	12.2	17.8	12.5
	HADCM3	A2	27.7	28.6	27.5	13.1	19.8	15.0
		B2	26.9	27.7	26.7	13.0	19.1	15.0
Coefficient of changes	Station		3.7	3.7	15.2	5.3	6.9	5.8
	Neural network	A2	3.6	3.6	7.1	4.9	6.6	5.5
		B2	3.6	3.6	14.9	5.0	6.7	5.6
	HADCM3	A2	2.5	2.4	2.5	9.3	2.6	2.8
		B2	2.5	5.5	2.6	9.4	1.7	2.8
Skewness	Station		-0.3	-0.5	-6.3	-0.3	-0.2	-0.1
	Neural network	A2	-0.3	-0.5	-6.3	-0.3	-0.2	-0.1
		B2	-0.3	-0.5	-6.3	-0.3	-0.2	-0.1
	HADCM3	A2	0.0	0.0	0.0	0.5	-0.3	0.4
		B2	0.0	0.0	0.0	0.5	-0.4	0.4
Max.	Station		28.2	27.1	26.2	13.1	19.8	13.7
	Neural network	A2	29.0	27.9	27.0	13.8	20.6	14.5
		B2	28.7	27.6	26.7	13.5	20.3	14.2
	HADCM3	A2	29.0	29.8	28.8	16.0	20.7	16.1
		B2	28.2	29.0	28.0	15.9	19.7	16.1
Min.	Station		22.5	22.5	0	10.2	14.4	10.2
	Neural network	A2	23.3	23.3	0.8	11.0	15.2	11.0
		B2	23.0	23.0	0.5	10.7	14.9	10.7
	HADCM3	A2	26.5	27.3	26.3	11.6	18.6	14.2
		B2	25.7	26.5	25.4	11.5	18.4	14.2
Quarter1	Station		25.0	24.8	23.6	11.2	16.3	11.7
	Neural network	A2	25.8	25.6	24.4	12.0	17.1	12.5
		B2	25.5	25.3	24.1	11.7	16.8	12.2
	HADCM3	A2	26.5	27.3	26.3	11.6	18.6	14.2
		B2	26.6	27.4	26.4	12.6	18.9	14.5
Quarter2	Station		25.4	25.4	24.0	11.7	17.3	12.0
	Neural network	A2	26.2	26.2	24.8	12.5	18.1	12.8
		B2	25.9	25.9	24.5	12.2	17.8	12.5
	HADCM3	A2	27.4	28.2	27.2	12.8	19.4	14.5
		B2	26.9	27.7	26.7	13.0	19.1	15.0
Quarter3	Station		26.7	26.8	25.2	12.5	18.8	13.4
	Neural network	A2	27.5	27.6	26.0	13.3	19.6	14.2
		B2	27.2	27.3	25.7	13.0	19.3	13.9
	HADCM3	A2	28.9	29.7	28.7	16.0	30.4	15.6
			28.1	28.9	27.9	15.0	19.5	15.6

Table 2 shows only the general characteristics of temperature variations at the studied stations. Therefore, *Tables 3* and *4* indicate monthly temperature variations based on HadCM3 and neural network outputs for the A2 and B2 scenarios.

Table 3. Prediction of temperature variations at the studied stations based on the neural network for the period 2015–2025.

A2	Jan	Feb	Mar	Apr	May	Jun	Jul	Aug	Sep	Oct	Nov	Dec
Abadan	0.7	0.8	0.9	1.2	1.0	1.1	1.0	1.7	0.8	1.0	0.6	0.7
Ahwaz	0.8	1.1	0.8	1.1	1.0	1.0	0.9	1.2	0.8	1.0	1.1	0.9
Dezful	0.5	0.4	0.2	0.3	0.3	0.3	0.01	0.3	0.1	0.3	0.6	0.8
Hamadan	0.5	0.8	0.7	0.7	0.6	0.8	0.8	0.8	0.7	0.9	0.4	0.6
Khorramabad	0.3	0.4	0.2	0.6	0.3	0.5	0.4	0.5	0.3	0.4	0.1	0.4
Shahrekord	0.5	0.6	0.3	0.3	0.1	0.0	0.2	0.1	0.1	0.2	0.2	0.5
B2	**Jan**	**Feb**	**Mar**	**Apr**	**May**	**Jun**	**Jul**	**Aug**	**Sep**	**Oct**	**Nov**	**Dec**
Abadan	0.9	1.1	1.1	1.4	1.3	1.4	1.2	1.9	1.1	1.3	0.9	1.1
Ahwaz	1.1	1.3	1.1	1.3	1.3	1.2	1.1	1.5	1.14	1.3	1.3	1.1
Dezful	0.9	0.6	0.5	0.6	0.5	0.5	0.3	0.6	0.35	0.61	0.91	1.2
Hamadan	0.8	1.1	1.0	0.9	0.8	0.83	1.2	1.1	1.03	1.1	0.7	0.9
Khorramabad	0.6	0.6	0.5	0.8	0.6	0.7	0.7	0.8	0.62	0.7	0.7	0.6
Shahrekord	0.8	0.8	0.6	0.6	0.3	0.2	0.5	0.4	0.37	0.5	0.53	0.6

Table 4. Prediction of temperature variations at the studied stations based on HadCM3 outputs for the period 2015–2025.

A2	Jan	Feb	Mar	Apr	May	Jun	Jul	Aug	Sep	Oct	Nov	Dec
Abadan	1.7	1.5	1.6	2.3	1.2	2.0	2.6	3.9	0.2	2.4	1.4	1.9
Ahwaz	3.2	3.3	3.0	1.2	1.2	2.7	2.9	3.3	1.1	3.5	3.5	3.5
Dezful	3.1	2.9	3.5	1.6	1.9	2.7	2.6	3.0	1.3	3.8	2.7	2.8
Hamadan	2.2	3.1	2.4	2.9	3.2	3.2	0.7	-0.5	0.0	-0.4	0.4	3.8
Khorramabad	3.0	4.5	3.4	2.6	3.6	1.5	-0.5	2.2	-2.2	-1.9	0.1	2.7
Shahrekord	2.2	5.0	2.8	2.9	2.7	-0.4	0.7	-0.3	-0.2	-1.2	-0.6	2.1
B2	**Jan**	**Feb**	**Mar**	**Apr**	**May**	**Jun**	**Jul**	**Aug**	**Sep**	**Oct**	**Nov**	**Dec**
Abadan	1.7	1.3	1.4	1.7	0.7	1.8	2.8	7.3	0.0	2.2	1.2	1.7
Ahwaz	2.8	3.1	2.8	0.6	1.1	2.5	2.7	3.1	0.9	3.3	3.3	3.3
Dezful	2.9	2.7	2.3	1.4	1.7	2.5	2.4	2.5	1.1	2.7	2.5	2.6
Hamadan	1.6	2.8	2.9	2.7	1.8	3.0	0.5	-0.7	-0.6	-0.7	-0.6	3.6
Khorramabad	2.8	2.3	2.2	3.4	3.4	1.3	-0.7	-2.2	-1.4	-1.2	-0.1	2.5
Shahrekord	3.0	2.8	2.6	2.7	2.5	-0.6	-1.5	-0.5	-0.4	-0.4	-0.8	1.9

Evaluation of temperature variations based on neural network outputs up to 2025 showed temperature increases in every month. As mentioned earlier, the neural network made better predictions than the HadCM3 model at most of the stations. Moreover, neural network outputs were acceptable at mountain stations, especially at Shahrekord, where the temperature increased by 0.1–0.3 C in all months based on the A2 scenario. In February, the increase was 0.6˚ C, which was the highest among the months. However, the temperature increased by nearly 0.89˚ C for the B2 scenario. In April, Khorramabad station showed the same increase, and the temperature was the highest among the months. In plain stations, mostly located in Khuzestan Province, the highest increases were observed among all the studied stations. The hot months of the year showed much more significant increases than the other months of the year.

Nevertheless, the B2 scenario outputs showed much more considerable increases in the hot months at plain stations. For instance, the temperature increased on average by up to 1.23 °C from April to October for the B2 scenario. The mountain stations showed smaller increases than the plain stations. The reason for this could be the role played by the highlands in temperature moderation at the mountain stations. Among the mountain stations the Hamadan showed a higher than 1 °C increase in temperature from June to October for the B2 scenario. However, the increase was lower than 1 °C at the other stations. According to Table 3, temperatures at the studied stations increased for both the A2 and the B2 scenarios based on the neural network outputs. The estimates of temperature variations are a little different based on the outputs of the HadCM3, so that these outputs showed an increasing trend in temperature in some months at the mountain stations (Khorramabad, Hamadan, and Shahrekord) but a decreasing trend in some months. Nevertheless, neural network outputs showed better results at these (mountain) stations. Temperature showed an increasing trend based on HadCM3 outputs for both the A2 and the B2 scenarios at plain stations (Abadan, Ahwaz, and Dezful). For instance, the temperature will approximately increase by 3 °C at the Abadan station during the next 90 years in April, whereas the neural network showed an approximately 1.2 °C increase until 2025 (*Table 5*). Based on the A2 scenario outputs, the increase will be 0.3 °C in September at Dezful station, although the B2 scenario predicted a 0.8 °C increase for the same month. Conditions are more diverse at the mountain stations. Increased and decreased temperatures at mountain stations, as mentioned before, can indicate large increases and decreases in diurnal temperatures in these areas in the future. Nevertheless, the uncontrolled increase in temperature can affect cultural factors, which will have economic implications in the countries. For instance, some studies in the the Sahara Desert indicate that, on average, 50% of crops will be changed by 2100 due to the sharp decrease of the uncontrolled increase in temperature (*Blanc et al.*, 2010). However, HadCM3 outputs showed substantial decreases in temperature from January to September at mountain stations for both the A2 and the B2 scenarios.

Table 5. Prediction of temperature variations at the studied stations based on the neural network and HadCM3 outputs for the period 2010–2099.

	Neural Network		HadCM3 outputs	
	A2	**B2**	**A2**	**B2**
Abadan	0.95	1.25	1.70	1.95
Ahwaz	0.95	1.20	1.40	2.70
Dezful	0.30	0.59	2.30	2.60
Hamadan	0.71	0.98	1.40	1.67
Khorramabad	0.42	0.66	1.00	1.57
Shahrekord	0.25	0.55	0.90	1.20

Table 6. Temperature variations at the studied stations based on HadCM3 outputs for the A2 scenario for the period 2010–2099.

	Jan	**Feb**	**Mar**	**Apr**	**May**	**Jun**	**Jul**	**Aug**	**Sep**	**Oct**	**Nov**	**Dec**
							2010–2039					
Abadan	0.7	0.5	0.6	1.3	0.7	1.0	1.6	2.9	-0.8	1.4	0.4	0.9
Ahwaz	0.2	2.3	2.0	0.2	0.3	1.7	1.9	2.3	1.0	2.5	2.5	2.5
Dezful	2.1	1.9	2.5	0.6	0.9	1.7	1.6	2.0	0.3	2.8	1.7	1.8
Hamadan	1.2	2.1	1.4	1.9	2.0	2.2	-0.3	-1.5	-1.0	-1.5	-1.4	2.8
Khorramabad	2.0	3.5	2.4	1.6	2.6	0.5	-1.5	1.0	-3.2	-3.0	-0.9	1.7
Shahrekord	1.2	4.0	1.8	1.9	1.7	-1.4	-0.3	-1.3	-1.2	-3.2	-1.6	1.1
							2040–2069					
Abadan	1.6	1.2	1.3	2.0	1.4	1.7	2.3	3.6	-0.1	2.1	1.1	1.6
Ahwaz	2.7	3.0	2.7	0.9	1.0	2.4	3.6	3.0	0.8	3.2	3.2	3.2
Dezful	2.8	2.6	3.2	1.3	1.6	2.4	2.3	2.7	1.0	3.5	2.4	2.5
Hamadan	1.9	2.8	2.1	2.6	2.7	2.9	0.4	-0.8	-0.3	-0.8	-0.7	3.5
Khorramabad	2.7	4.2	3.1	2.3	3.3	1.2	-0.8	1.7	-2.5	-2.3	-0.0	2.4
Shahrekord	1.9	4.7	2.5	2.6	2.4	-0.7	0.4	-0.6	-0.5	-2.5	0.9	1.8
							2070–2099					
Abadan	1.7	1.5	1.6	2.3	1.7	0.2	2.6	3.9	0.2	2.4	1.4	1.9
Ahwaz	3.0	3.3	3.0	1.2	1.3	2.7	2.9	3.3	1.1	3.5	3.5	3.5
Dezful	3.1	2.9	3.5	1.6	1.9	2.7	2.6	3.0	1.3	3.8	2.7	2.8
Hamadan	2.2	3.1	2.4	2.9	3.0	3.2	0.7	-0.5	0.0	-0.5	-0.4	2.8
Khorramabad	3.0	4.5	3.4	2.6	3.6	1.5	-0.5	2.0	-2.2	-0.2	0.1	2.7
Shahrekord	2.2	5.0	2.8	2.9	2.7	-0.4	0.7	-0.3	-0.2	-2.2	-0.6	2.1

Table 7. Temperature variations at the studied stations based on HadCM3 outputs for the B2 scenario for the period 2010–2099.

	Jan	Feb	Mar	Apr	May	Jun	Jul	Aug	Sep	Oct	Nov	Dec
2010–2039												
Abadan	1.1	0.7	0.8	1.1	0.1	1.2	2.2	3.1	-0.6	1.6	0.6	1.1
Ahwaz	2.2	2.5	2.2	0.0	0.5	1.9	2.1	2.5	0.3	2.7	2.7	2.7
Dezful	2.3	2.1	2.7	0.8	1.1	1.9	1.8	1.9	0.5	2.1	1.9	2.0
Hamadan	1.3	2.2	2.3	2.1	1.2	2.4	-0.1	-1.3	-1.2	-1.3	-1.2	3.0
Khorramabad	2.2	1.7	1.6	2.8	2.8	0.7	-1.3	-2.8	-2.0	-1.8	-0.7	1.9
Shahrekord	2.4	2.2	2.0	2.1	1.9	-1.2	-2.1	-1.1	-1.0	-1.0	-1.4	1.3
2040–2069												
Abadan	1.9	1.5	1.6	1.9	0.9	2.0	3.0	3.9	02	2.4	1.4	1.9
Ahwaz	0.3	3.3	3.0	0.8	1.3	2.7	7.9	3.3	1.1	3.5	3.5	3.5
Dezful	3.1	2.9	3.5	1.6	1.9	2.7	2.6	2.7	1.3	2.9	2.7	2.8
Hamadan	2.1	3.0	3.1	2.9	2.0	3.2	0.7	-0.5	-0.4	-0.5	-0.4	3.8
Khorramabad	3.0	2.5	2.4	3.6	3.6	1.5	-0.5	-2.0	-1.2	-1.0	0.1	2.7
Shahrekord	3.2	3.0	2.8	2.9	2.7	-0.4	-1.3	-0.3	-0.2	-0.2	-0.6	2.1
2069–2099												
Abadan	2.1	1.7	1.8	2.1	1/1	2.2	3.2	4.1	0.4	2.6	1.6	2.1
Ahwaz	3.2	3.5	3.2	1.0	1.5	2.9	3.1	3.5	1.3	3.7	3.7	3.7
Dezful	3.3	3.1	3.7	1.8	2.1	2.9	2.8	2.9	1.5	3.1	-2.9	3.0
Hamadan	2.3	3.2	3.3	3.1	2.2	3.4	0.9	-0.3	-0.2	-0.3	-0.2	0.4
Khorramabad	3.2	2.7	2.6	3.8	3.8	1.7	-0.3	-1.8	-1.0	-0.8	0.3	2.9
Shahrekord	3.4	3.2	3.0	3.1	2.9	-0.2	-1.1	-0.1	0.0	0.0	-0.4	2.3

For a more accurate analysis of temperature variations at the studied stations, changes in temperature for the different months were presented for three baseline periods. *Tables 6* and *7* show the results for the A2 and B2 scenarios. As shown in the tables, these variations follow an annual pattern with the difference that temperature variations are more considerable for both the A2 and the B2 scenarios. Other characteristics are totally observed in the tables, although the B2 scenario shows a higher increase (*Table 7*). According to *Tables 6* and *7*, the temperature decreased at the mountain stations in the first period (2010–2039) much more than in the other periods (2040–2069 and 2070–2099). For instance, in the downscaling SDSM based on the outputs for the A2 and B2 scenarios at the mountain stations (Khorramabad, Shahrekord, and Hamadan) in October, there were decreases of 2.5 and 1.24 °C on average, respectively. However, the intensity of decrease declined towards the recent periods so that the predicted decreases were 1.5 and 0.36 °C, respectively, during 2070–2099. Regarding the studies on climate fluctuations, the temporal index is very important, because climate, as a system, results from a series of meteorological conditions that have been tangible through the data of several previous decades, and their occurrence

and recurrence are probable in the future decades. Therefore, the current climate, to which we have well been adjusted, is described by the data of several previous decades. Nonetheless, the neural network, which predicted up to a fourth of the studied period (i.e., up to 2025), predicted more tangible changes in some plain stations, especially Abadan and Ahwaz. This region in Iran is affected more by fluctuations of the Persian Gulf due to its proximity, so that studies indicate an increase up to 2 °C in the temperature of surface water in the Persian Gulf (*Rigel*, 2002). However, mountain stations showed slight increases. AGCMs, regarded as some of the most reliable tools for the analysis of climate change impacts on different systems, and are capable of simulating climate parameters for a long period of time by using the scenarios confirmed by IPCC (*Kilsby* et al., 2007), predicted an increase of 1–2 °C in temperatures at these stations.

Nevertheless, both scenarios produced similar predictions in downscaling considering the nature of the definitions of these scenarios. This may be due to the fact that greenhouse gases, which are considered by scientists to be the main factor causing climate change (*Jahanbakhsh et al.*, 2010), are not measured at the studied stations, especially at the mountain stations. Consequently, the NCEP data were measured mainly based on estimates and interpolation. Therefore, most researchers have predicted greater increases in temperature. The results showed that the Hamadan Station would encounter an almost 1.2 °C of increase by 2099. At the same time, the outputs of two AGCMs (HadCM2, ECHAM4) and of the MAGICC-ECHAM4 model predicted that the temperatures of all Iranian provinces would experience a 2–3.6 °C increase on average by 2100 (*Abbasi* and *Asmari*, 2012). If the behaviors and data series predicted based on both methods are taken into account, we will notice that they exhibit similar behaviors and fluctuations in general, but the fluctuation range of the HadCM3 is wider than that of the neural network. As stated earlier, the temperatures at the studied stations increased by 0.5–1.5 °C on average. However, the IPCC estimated the average temperature will increase from 0.5 to 1 °C based on the HadGEM and by 3 °C based on the HadCM3 for the studied region, assuming that CO_2 concentration will increase by 1% in the atmosphere. These results are almost consistent with those of the present research (*Fig. 2*). Some researchers have predicted that Iran's temperature will increase by 1–3 °C (*Abbasi et al.*, 2010). For instance, the temperature increased by up to 2.5 °C on average at some parts of the mountain stations. In addition, the temperature rise was nearly 1.5 °C at the mountain stations based on HadCM3 outputs for the A2a and the B2a scenarios. Nonetheless, most researchers have predicted a temperature raise (*Ashraf et al.* 2011*a*; *Parvin*, 2010). As mentioned earlier, the estimates of temperature increase for the A2a and B2a scenarios, despite the different natures of these two scenarios, were almost similar, because greenhouse gases were not measured. At some stations, such as Ahwaz and Abadan, the temperature will exhibit a 1.0–2.5 °C increase on average by 2099. However, the neural network showed that changes would be negligible up to 2025.

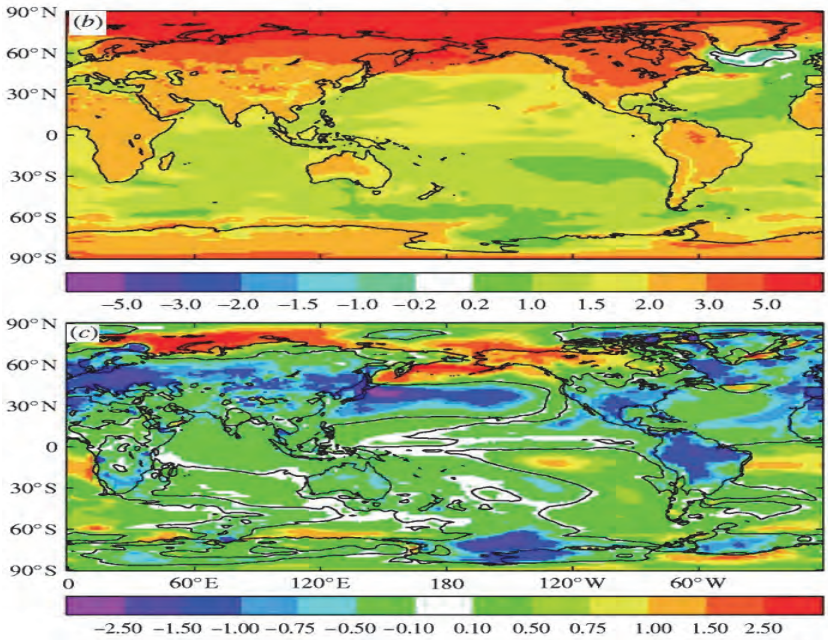

Fig. 2. Mean temperature variations of the world based on (a) Had GEM and (b) HadCM3 (source: IPCC)

4. Summary and conclusions

Climate is considered one of the fundamental pillars of human life, and its protection assumes a daily increase in importance considering the global progress and development. Climate change is one of the most complicated problems that we are facing now and will confront in future. Humans are the main cause of climate change by neglecting the rules governing nature and lacking enough knowledge of environmental problems related to climate. The uncontrolled interventions have caused climate parameters to continuously change on temporal and spatial scales. These changes represent one of the natural characteristics of the atmospheric cycle resulting from abnormalities or fluctuations in the trends of meteorological parameters such as precipitation and temperature. Subjects related to climate change have been raised, and human activities in relation to emission of greenhouse gases such as CO_2 and methane as well as other topics pertaining to climate change have been discussed at universities and research centers indicating that great losses will result from climate change. Nowadays, climate change prediction is very important in macro planning activities. In this regard,

GCMs are among the most powerful existing tools that are evolving for simulation of climate change. These models are highly reliable on global and planetary scales. For this purpose, temperature changes were estimated using the HadCM3 model and a neural network in southwest Iran at plain stations (Abadan, Ahwaz, and Dezful) and mountain stations (Hamadan, Khorramabad, and Shahrekord). The research data included the diurnal average temperature of synoptic stations in southwest Iran, NCEP reanalysis data, and the outputs of a third-generation global climate model HadCM3 under the A2 and B2 scenarios for the baseline period (1961–1990). The following results were obtained:

1) HadCM3 outputs at plain stations (Abadan, Ahwaz, and Dezful) yielded more appropriate results than at mountain stations (Hamadan, Khorramabad, and Shahrekord). However, the neural network showed better estimates at mountain stations and at plain stations. The amounts of error of the neural network and HadCM3 outputs were not so significantly different at plain stations that one of them could be preferred to the other in evaluating temperature variations. Nevertheless, conditions were more diverse at mountain stations.
2) Evaluation of temperature variations based on the neural network and HadCM3 outputs suggested that, in general, plain and mountain stations would encounter an increasing trend in temperature. However, temperature rise would be more remarkable at plain stations. Regarding the monthly scales based on HadCM3 outputs, plain stations will show increasing trends in temperature mainly from January to April.
3) Comparison of the evaluations on climate change based on the A2 and B2 scenarios revealed that both of them predicted a rise in temperature, but the latter showed a greater increase in the trend of temperature rise at the studied stations. However, both scenarios showed nearly similar results for the neural network. All in all, it can be concluded that HadCM3 outputs would be reliable only in yielding an overall estimate for the entire region, and care should be exercised in using it to study fluctuations, increases, and decreases in temperature. On average, based on the outputs of HadCM3, temperatures will rise by 1.4 and 1.9 °C in the southwestern part of Iran by 2099 for the A2 and B2 scenarios, respectively. As mentioned earlier, temperatures at most stations showed increasing trends, resulting in many problems. Surface evaporation caused by global warming will dry out rivers and lower the quality of water. This problem will be much more evident in drier areas such as desert and semi-desert regions. In addition, increased salts in drinking water can decline its quality through water evaporation. At the same time, the available water for agricultural purposes will decrease, and drought will endanger food security. Drought can also make villagers migrate to cities, resort to marginalization, and decide to work false jobs. It can also worsen social abnormalities.

References

Ababaei, B., *Mirzaei, F.*, and *Sohrabi, T.*, 2011: LARS-WG Performance Evaluation at 12 Coastal Meteorological Stations of Iran. *Res. J. Iran's Water 5*, 217–222.

Abbasi, F. and *Asmari, M.*, 2012: Forecasting and Evaluating Temperature and Precipitation Variations of Iran in Future Decades through MAGICC-SCENGEN Model. *Water Soil, 25*, 70–83.

Abbasi, F.; Babaiyan, I.; Malbousi, S.; Imari, Morteza; Mokhtari, Lili Goli, 2010: Assessing Iran's Climate Change in the Next Decades (2025 to 2100 AD) Using the Exponential Downscaling of AGCMs. *Geograph. Res. 104*, 17979–18005.

Ashraf, B., M. Mousavi Baygi, M. Kamali and *Davari, K.*, 2011a: Prediction of seasonal variations of climatological parameters over next 20 years by using statistical downscaling method of HadCM3 data. *J. Water Soil 25*, 945–957.

Ashraf, B., Mousavi Bygi, Muhammad; Kamali, Gholamali; and *Davari, K.*, 2011b: Predicting Seasonal Changes in Climatic Parameters in 20 Years Using Downscaling of HadCM3 Data (Case Study: Razavi Khorasan Province), *Water Soil 4*, 940–952.

Blanc, P., Bourbon, X., Lassin, A., and *Gaucher, E.C.*, 2010: Chemical model for cement-based materials: Temperature dependence of thermodynamic functions for nanocrystalline and crystalline C–S–H phases. *Cement Concrete Res. 40*, 851–866. https://doi.org/10.1016/j.cemconres.2009.12.004

Blasing, T.J., 1981: Characteristic anomaly patterns of summer sea-level pressure for the Northern Hemisphere. *Tellus 33*, 428–437. https://doi.org/10.3402/tellusa.v33i5.10732

Broccoli, A.J., and *Harnack, R.P.*, 1981: Predictability of monthly North Pacific sea level pressure from monthly sea surface temperature for the period 1933–1976. *Month. Weather Rev. 109*, 2107–2117. https://doi.org/10.1175/1520-0493(1981)109<2107:POMNPS>2.0.CO;2

Chen, H., Xu, C.Y., and *Guo, S.*, 2012: Comparison and evaluation of multiple GCMs, statistical downscaling and hydrological models in the study of climate change impacts on runoff. *J. hydrol. 434*, 36–45. https://doi.org/10.1016/j.jhydrol.2012.02.040

Dorji, S., Herath, S., and *Mishra, B.K.* 2017: Future climate of Colombo downscaled with SDSM-neural network. *Climate 5*, 24. https://doi.org/10.3390/cli5010024

Fiseha, B.M., Melesse, A.M., Romano, E., Volpi, E., and *Fiori A.*, 2012: Statistical Downscaling of Precipitation and Temperature for the Upper Tiber Basin in Central Italy. *Int. J. Water Sci.1*, 3. https://doi: 10.5772/52890

Harpham, C. and *Wilby, R.L.*, 2005: Multi-site downscaling of heavy daily precipitation occurrence and amounts. *J. Hydrology, 312*, 235–255. https://doi.org/10.1016/j.jhydrol.2005.02.020

Hassan, Z., Harun, S., and *Malek, M.A.*, 2012: Application of ANNs model with the SDSM for the hydrological trend prediction in the sub-catchment of Kurau River, Malaysia. *J. Environ. Sci. Engin. B, 1*(5B). https://doi.org/10.1007/s002270100676

Jahanbakhsh, S.; Hadiani, Mir Omid; Rezaei Banafsheh, Majid; and *Dinpazhouh, Yaghoub*, 2010: Modeling Parameters of Climate Change in Mazandaran. The Fourth International Congress of Geographers in the Islamic World: Zahedan, Iran, April 14–16, 2010.

Khan, M.S., Coulibaly, P., and *Dibike, Y.*, 2006: Uncertainty analysis of statistical downscaling methods. *J. Hydrolo. 319*, 357–382. https://doi.org/10.1016/j.jhydrol.2005.06.035

Kilsby, C.G., Jones, P.D., Burton, A., Ford, A.C., Fowler, H.J., Harpham, C., ... and *Wilby, R.L.*, 2007: A daily weather generator for use in climate change studies. *Environ. Model. Software 22*, 1705–1719. https://doi.org/10.1016/j.envsoft.2007.02.005

Kug, J.S., Lee, J.Y., Kang, I.S., Wang, B., and *Park, C.K.*, 2008: Optimal multi-model ensemble method in seasonal climate prediction. *Asia-Pacific J. Atmosph. Sci. 44*, 259–267.

Maraun, D., Widmann, M., Gutiérrez, J.M., Kotlarski, S., Chandler, R.E., Hertig, E., ... and *Wilcke, R.A.*, 2015: VALUE: A framework to validate downscaling approaches for climate change studies. *Earth's Future 3*, 1–14. https://doi.org/10.1002/2014EF000259

McGuffie, K., Henderson-Sellers, A., Holbrook, N., Kothavala, Z., Balachova, O., and *Hoekstra, J.*, 1999: Assessing simulations of daily temperature and precipitation variability with global climate models for present and enhanced greenhouse climates. *Int. J. Climatol.: A, 19*, 1–26. https://doi.org/10.1002/(SICI)1097-0088(199901)19:1<1::AID-JOC348>3.0.CO;2-T

Meshkati, A.H., Kordjazi, M., and *Babaiyan, I.,* 2010: Analysis and Evaluation of LARS in Simulating Meteorological Data of Golestan Province during 1993–2007, *Appl. Studies Geograph. Sci. 16*, 81–96.

Mohammadi, B., 2014: Identifying Spatial and Temporal Abnormalities of Seal Level Pressure in Iran. *Geograph. Res.* 1, 43–58.

Ojha, S.P., Kumar C., Goyal, M., and *J Adeloye, A.*, 2010: Downscaling of precipitation for lake catchment in arid region in India using linear multiple regression and neural networks. *The open Hydrology J. 4*, 122–136. https://doi.org/10.2174/1874378101004010122

Pan, Y. and *Jackson, R.T.*, 2008: Ethnic difference in the relationship between acute inflammation and serum ferritin in US adult males. *Epidemiol. Infect. 136*, 421–431.

Parvin, N., 2010: Study of Climate Change in the Past Fifty Years with an Emphasis on the Southwest of Iran. The Fourth International Congress of Geographers in the Islamic World: Zahedan, Iran, April 14–16, 2010.

Pope, V.D., Gallani, M.L., Rowntree, P.R., and *Stratton, R.A.,* 2000: The impact of new physical parametrizations in the Hadley Centre climate model: HadAM3. *Climate Dynam. 16*, 123–146. https://doi.org/10.1007/s003820050009

Riegl, B., 2002: Effects of the 1996 and 1998 positive sea-surface temperature anomalies on corals, coral diseases and fish in the Arabian Gulf (Dubai, UAE). *Marine Biol. 140*, 29–40. https://doi.org/10.1007/s002270100676

Sahai, A.K., Grimm, A.M., Satyan, V., and *Pant, G.B.*, 2003: Long-lead prediction of Indian summer monsoon rainfall from global SST evolution. *Climate Dynam. 20*, 855–863. https://doi.org/10.1007/s00382-003-0306-8

Sahai, S., Sharma, C., Singh, S. K., and *Gupta, P. K.*, 2010: Ambient CO levels during winter and summer agricultural burning seasons of Northern India. *Asian J.Water, Environ.Pollut. 7*(4), 99-104.

Samadi, S., Carbone, G.J., Mahdavi, M., Sharifi, F., and *Bihamta, M.R.,* 2013: Statistical downscaling of river runoff in a semi arid catchment. *Water Res. Manage. 27*, 117–136. https://doi.org/10.1007/s11269-012-0170-6

Santer, B.D., Taylor, K.E., Wigley, T.M.L., Johns, T.C., Jones, P.D., Karoly, D.J., ... and *Schwarzkopf, M.D.*, 1996: A search for human influences on the thermal structure of the atmosphere. *Nature, 382*(6586), 39–46. https://doi.org/10.1038/382039a0

Smith, D.J., Christen, E.W., Cutting, M., and *Hornbuckle, J.W.*, 2010: An analysis of climate change impacts on irrigated crop water requirement in the SA MDB region. Darling Downs: Cooperative Research Centre for Irrigation Futures.

Whetton, P.H., 1990: Relationships between monthly anomalies of sea-surface temperature and mean sea level pressure in the Australian region. Australian meteorological magazine. 1990; 38(1):17-30. http://hdl.handle.net/102.100.100/258514

William, W. and *Wei, S.*, 1998: time series analysis, univariate and multivariation method. Second edition, Publisher: Pearson Addison Wesley, ISBN: 0-321-32216-9.

DOI:10.28974/idojaras.2021.3.9

IDŐJÁRÁS

Quarterly Journal of the Hungarian Meteorological Service
Vol. 125, No. 3, July – September, 2021, pp. 513–519

Short Contribution

On the correction of processed historical rainfall data of siphoned rainfall recorders

Tibor Rácz

Doctoral School of Environmental Sciences at the Szent István University
Páter Károly utca 1, Gödöllő, 2100, Hungary
raczt167@gmail.com

(Manuscript received in final form September 28, 2020)

Abstract— Historical rainfall data registered by siphoned rainfall recorder (SRW) devices have been widely used for a long time in rainfall intensity investigations. A relatively known counting error of the SRW devices is the siphoning error, when the registration of rainfall is blocked temporarily, during the drainage of measure tank. This issue causes a systematic underestimation in the rainfall and rainfall intensity measurement results. To reduce its consequences, a data correction is crucial when SRW data are used, for example as a reference for climate comparison studies, or for proceeding of intensity-duration-frequency curves, etc. In this paper, a formula is presented to fix the siphonage error of SRW devices for historical rainfall data. The early measures were processed in a significant percentage of cases, and sometimes the original measurement results (registration ribbon) have been lost. An essential advantage of the presented formula is that it can be applied for these processed data, which show only the intensity of a known length time interval. For this correction, the average rainfall intensity and the length of the time window are needed, over the physical parameters of the SRW device. The data correction can provide a fixed value of the rainfall intensity, which is undoubtedly closer to the real average rainfall intensity. The importance of this formula is in the reprocessing and validation of the historical rainfall intensity data, measured by siphoned rainfall recorders.

Key-words: historical rainfall data, siphoned rainfall recorder, rainfall intensity, data correction, siphoning issue

1. Introduction

The rainfall intensity measurement has particular importance in several fields of sciences. The measurement of the rainfall intensity has a 300-year-long history

(*Kurytka*, 1953). There are several arrangements and devices which were used to measure and register this parameter for scientific, and mainly for engineering applications. One of the most widely used instruments for this aim is the siphoned rainfall recorder (SRW), which has been used mostly in the first two-thirds of the 20th century, and there are several devices in use even nowadays. Some old shops produce these instruments, and there are new producers, as well (e.g., Dr. Alfred Müller MI KG, Theodor Friedrichs Atelier). Some of these kinds of devices were electrified, using sensors and data loggers to ensure the further use of these instruments in the future in a simpler way. There was a widely spread opinion about the excellent accuracy and reliability of these instruments; however, the accuracy issues during the most intensive part of showers, induced by a break during the siphonage were well known. Kallós investigated these errors in the Hungarian practice in the 1950s (*Kallós*, 1955), who had a proposal to fix this kind of error on the base of the registration ribbon. A similar proposal was given by Luyckx and Berlamont, on the base of a theoretical approach and laboratory measurements (*Luyckx* and *Berlamont*, 2002). The suggestion of Luyckx and Berlamont, similarly to the result of Kallós, is related to the correction of the registration ribbons of the SRWs. They have presented the relative error of the SRW devices, which has the same magnitude as the tipping bucket rainfall recorders. However, the method of Luyckx and Berlamont is a simple and handful tool for the data correction of continuously registered data, and its use is limited to the repair of the complete registration ribbon.

However, rather often the registration ribbons cannot be available anymore; there are only the processed data of characteristic rainfall intensity values of unique showers. This kind of processing has resulted in the highest intensities of some time window, for example, the maximum intensities of the 5-10-20-30-60 minutes long time intervals. In these cases, the previously mentioned correction methods cannot be used, since the instantaneous rainfall intensity is unknown, but it still would be necessary to correct the effect of siphonage error, at least approximately. The correction of this issue is important, since the relation of the rainfall intensities in the past in a given geographical site can be determined only on the base of these historical data. In this paper, a method is presented to approach this issue and to fix the early, processed rainfall intensity data for the use of the hydrologists of our age.

2. Methods

The method of *Luyckx* and *Berlamont* (2002) is based on the determination of the time of siphoning during the rainfall, and the realistic volume of rainwater can be calculated using the added siphoning time. As the real volume is available, the real rainfall intensity can be recalculated and determined. As the error is a systematic undercatch, the fixed intensity is always higher than those, which were

determined on the base of the registration ribbon. For this method, the instantaneous intensity is needed at the siphoning period, over the technical parameters of the SRW, as the siphonage rate and the catching surface of the funnel.

This method can be extended to longer time windows only with the average rainfall intensity, without knowing the internal raw data of the time interval. In this paper, a correction method for time windows of any lengths is presented. The proposed method is an approach, which helps to get the data closer to the realistic rainfall intensity values. The correctness of the proposed formula will be shown.

3. Results and discussion

3.1. The correction method for rainfall intensities of a t time interval

A rainfall event can be divided into various time intervals, and these intervals can be characterized by rainfall intensity. In a *t* time interval, the value of the rainfall intensity is i_t. The V_t volume of the fallen rain measured by the instrument during this period is

$$V_t = t \times i_t. \tag{1}$$

During these time windows, one or more siphonage can occur if the fallen rainfall depth reaches the width of the registration ribbon at least once. The number of siphonage during the *t* time window is the integer part of the quotient of the volume of the fallen rainfall expressed in depth over a unique surface. The recording limit of the device is expressed in rainfall depth, as well. The recording limit is practically the maximum depth of the rainfall which can be drawn on the ribbon, after which the siphonage must happen, and the drawing of the rainfall depths can be continued from the base edge of the paper. The recording limit value in practice is 10–15 mm rain depth, depending on the type of device. So, *n* can be calculated with the following formula:

$$n = int\left(\frac{V_t}{h_s}\right) = int\left(\frac{t \times i_t}{h_s}\right), \tag{2}$$

where *n* is the average repetition number of the siphonage during the *t* interval, h_s is the recording limit of the SRW device.

The duration of siphoning is an essential parameter of the instruments since, during its drainage, the measurement is suspended. The length of the siphonage period depends on the technical parameters of the device and the actual rainfall supply. The duration of the siphonage is a constant technical parameter of the device, in the magnitude of 10-30 seconds. Another key parameter is the siphonage rate of the device; it is in relation to the siphonage time and the volume

of the receiving tank of the SRW instrument. The drainage rate is a known technical parameter, as well. If there is no rainfall supply, a base value of the siphonage rate can be gained. If there is a rain replenishment, the siphonage period must be longer. If the rainfall intensity would be equal to the base value of the siphonage rate, the rainwater could flow through the gauge without being measured. Still, of course, the siphonage rate chosen by the producers is high enough to avoid this situation. During the rainfall supply, the time of siphonage can be calculated by the following formula, according to *Luyckx* and *Berlamont* (2002):

$$t_s = \frac{t_{s,0}}{1-\frac{q}{q_s}}, \tag{3}$$

where t_s – the length of a unique siphonage period, $t_{s,0}$ is the length of the emptying of the device, if there is no water collected during the siphoning, q is the rate of the rainfall, and $q_s$is the rate of the siphonage.

In a time window, more siphoning periods can occur. For the time window, only the i_t average rainfall intensity is known. The $t_{s,tot}$ total siphonage time during the *t* time window, supposing that the rainfall intensity, so the rate of the rainfall is constant and equal to its average value is

$$t_{s,tot} = n \times t_s . \tag{4}$$

The V_s rainfall volume, which falls during the siphonage and has not been measured can be calculated as

$$V_s = t_{s,tot} \times i_t . \tag{5}$$

The V_{corr} corrected volume of the rainfall is the sum of V_t measured volume and V_s calculated unmeasured volume, which seems to be collected during a more extended period than *t*; but this means only that over the incompletely collected rainfall, there is an amount of rainwater to be added to the registered volume. So, the corrected volume is

$$V_{corr} = V_t + V_s = \left(t + t_{s,tot}\right) i_t . \tag{6}$$

In reality, the volume V_{corr} of rainfall falls in *t* time, so the $i_{t,corr}$ corrected rainfall intensity in the *t* interval is

$$i_{t,corr} = \frac{V_{corr}}{t} . \tag{7}$$

The rainfall rate is the discharge of rainwater which flows down from the funnel of the gauge during the measurement. The rainfall rate can be written as

$$q = A_f \times i_t, \tag{8}$$

where A_f is the area of the catching surface of the gauge.

The unified formula of the correction can be the following:

$$i_{corr} = \frac{\left(t + int\left(\frac{t \times i_t}{h_s}\right)\left(\frac{t_{s,0}}{1 - \frac{A_f \times i_t}{q_s}}\right)\right)}{t} \times i_t \,. \tag{9}$$

3.2. Verification of accuracy

The confirmation of the proposed method is presented with a comparison to the result of the series of unique corrections of the siphoning issue. This process is practically the core of the data fixing procedure of Luyckx and Berlamont, using it for a series of siphoning in a given *t* time interval. In the followings, this comparison is going to be presented.

The core of the correction part is the time of siphonage, t_{corr}, when the measurement is suspended. In Eq. (9) is the second part of the expression between the brackets:

$$t_{corr} = int\left(\frac{t \times i_t}{h_s}\right)\left(\frac{t_{s,0}}{1 - \frac{A_f \times i_t}{q_s}}\right). \tag{11}$$

For the verification, the series of unique corrections must be inspected. The correction part of the siphonage error of a unique siphonage can be expressed as

$$t_{u,corr} = \left(\frac{t_{s,0}}{1 - \frac{A_f \times i_u}{q_s}}\right), \tag{12}$$

where i_u is the instantaneous rainfall intensity at the period of a unique siphonage.

The total siphonage error in a particular *t* time interval when *n* siphonages occur is

$$t_{\sum u,corr} = \sum_{j=1}^{n} \left(\frac{t_{s,0}}{1 - \frac{A_f \times i_{u,j}}{q_s}} \right) . \quad (13)$$

The question is whether or not Eq. (11) converges to Eq. (13). The simplification of the Eq. (11) for the proposed method results in the following:

$$t_{corr} = t_{s,0} \times q_s \times int\left(\frac{t \times i_t}{h_s}\right)\left(\frac{1}{q_s - A_f \times i_t}\right) \sim int\left(\frac{t \times i_t}{h_s}\right)\left(\frac{1}{q_s - A_f \times i_t}\right). \quad (14)$$

After making a similar transformation on Eq. (13), the result is

$$t_{\sum u,corr} = t_{s,0} \times q_s \sum_{j=1}^{n} \left(\frac{1}{q_s - A_f \times i_{u,j}}\right) \sim \sum_{j=1}^{n} \left(\frac{1}{q_s - A_f \times i_{u,j}}\right). \quad (15)$$

The value of rainfall intensity i_t is the time average of the increment of caught rainfall volume in t time, meanwhile $i_{u,j}$ are instantly measured intensities at the siphoning processes in the same t time window. However, the $i_{u,j}$ intensities are unique intensities of the same rainfall; their averages are not similar to the i_t, these averages can differ a lot theoretically. The occurrence of $i_{u,j}$ values has a sampling character; after the first siphoning in the interval, the emptying – and so the sampling – happens regularly, catching a certain volume of rainwater. This sampling character ensures that for a long period and/or shorter siphoning periods, the average of unique intensities must approach the calculated average intensities. Of course, a unique intensity value during the siphoning process always differs from the average intensity of the correction, notwithstanding, the correction provides a good approximation for its value. In a hypothetical case, if there would be infinite numbers of siphoning during the time window, the average of the unique intensities must be equal to the calculated average intensity.

In reality, as the time windows showing the highest intensities always occur at the supremum or local suprema of the rainfall, the peak of the intensity is somewhere in the middle of the interval. A significant difference between the two averages could occur, if there would be an incredibly high and narrow peak of rainfall depth in the time window between two siphoning, but, despite the high variability of the temporal rainfall intensities, this situation is not likely at all. On the basis of this consideration, the i_t and the average of $i_{u,j}$ intensities might be close enough to each other, and this means that the proposed approach is a reasonable estimation of the reality.

4. Conclusion

The presented method is a simple tool for the correction of the earlier measured rainfall intensity data of siphoning rainfall recorders, where the original data are not available, and only some intensities can be found for known time intervals. The method can fix the main systematic error of these devices. For the procedure of the correction, the hydraulic characteristics of the device are needed, as the catching surface of the funnel and the siphoning rate of the instrument's discharging system. The accuracy of the correction was presented over some extreme theoretical cases, and the corrected intensity data approach the results efficiently based on a correction executed uniquely by the siphoning occurrences. This method helps to clear the historical databases to make them a better reference for the investigation of the climate change, relating to the rainfall intensities.

The proposed correction does not solve the other significant source of error of rainfall measurements the windfield deformation, which demands a solution to ensure a real accuracy of the collected data. This kind of error would have particular importance in the future.

References

Kallós, I., 1955: Ombrogrammok értékelése. *Hidrológiai Közlöny, 1955,* 293–296. (in Hungarian)

Kurytka, J.C., 1953: Precipitation measurements study. Urbana, Illinois, USA: the State of Illinois, State Water Survey Division, Dpt of Education and Registration. Available at: https://citeseerx.ist.psu.edu/viewdoc/download?doi=10.1.1.461.3364&rep=rep1&type=pdf (accessed 2 September 2020)

Luyckx, G. and *Berlamont, J.*, 2002: Accuracy of siphoning rain gauges. Global Solutions for Urban Drainage – Proceedings. Portland USA, American Society of Civil Engineers. Available at: https://www.researchgate.net/publication/268176925_Accuracy_of_Siphoning_Rain_Gauges (accessed 2 September 2020)

INSTRUCTIONS TO AUTHORS OF *IDŐJÁRÁS*

The purpose of the journal is to publish papers in any field of meteorology and atmosphere related scientific areas. These may be

- research papers on new results of scientific investigations,
- critical review articles summarizing the current state of art of a certain topic,
- short contributions dealing with a particular question.

Some issues contain "News" and "Book review", therefore, such contributions are also welcome. The papers must be in American English and should be checked by a native speaker if necessary.

Authors are requested to send their manuscripts to

Editor-in Chief of IDŐJÁRÁS
P.O. Box 38, H-1525 Budapest, Hungary
E-mail: journal.idojaras@met.hu

including all illustrations. MS Word format is preferred in electronic submission. Papers will then be reviewed normally by two independent referees, who remain unidentified for the author(s). The Editor-in-Chief will inform the author(s) whether or not the paper is acceptable for publication, and what modifications, if any, are necessary.

Please, follow the order given below when typing manuscripts.

Title page should consist of the title, the name(s) of the author(s), their affiliation(s) including full postal and e-mail address(es). In case of more than one author, the corresponding author must be identified.

Abstract: should contain the purpose, the applied data and methods as well as the basic conclusion(s) of the paper.

Key-words: must be included (from 5 to 10) to help to classify the topic.

Text: has to be typed in single spacing on an A4 size paper using 14 pt Times New Roman font if possible. Use of S.I. units are expected, and the use of negative exponent is preferred to fractional sign. Mathematical formulae are expected to be as simple as possible and numbered in parentheses at the right margin.

All publications cited in the text should be presented in the *list of references*, arranged in alphabetical order. For an article: name(s) of author(s) in Italics, year, title of article, name of journal, volume, number (the latter two in Italics) and pages. E.g., *Nathan, K.K.,* 1986: A note on the relationship between photo-synthetically active radiation and cloud amount. *Időjárás 90,* 10–13. For a book: name(s) of author(s), year, title of the book (all in Italics except the year), publisher and place of publication. E.g., *Junge, C.E.,* 1963: *Air Chemistry and Radioactivity.* Academic Press, New York and London. Reference in the text should contain the name(s) of the author(s) in Italics and year of publication. E.g., in the case of one author: *Miller* (1989); in the case of two authors: *Gamov* and *Cleveland* (1973); and if there are more than two authors: *Smith et al.* (1990). If the name of the author cannot be fitted into the text: *(Miller,* 1989); etc. When referring papers published in the same year by the same author, letters a, b, c, etc. should follow the year of publication. DOI numbers of references should be provided if applicable.

Tables should be marked by Arabic numbers and printed in separate sheets with their numbers and legends given below them. Avoid too lengthy or complicated tables, or tables duplicating results given in other form in the manuscript (e.g., graphs). *Figures* should also be marked with Arabic numbers and printed in black and white or color (under special arrangement) in separate sheets with their numbers and captions given below them. JPG, TIF, GIF, BMP or PNG formats should be used for electronic artwork submission.

More information for authors is available: journal.idojaras@met.hu

Published by the Hungarian Meteorological Service

Budapest, Hungary

ISSN 0324-6329 (Print)

ISSN 2677-187X (Online)